NEW DESIGN AND SYNTHETIC STRATEGIES OF METAL-ORGANIC FRAMEWORKS

A Dissertation

by

ZHANGWEN WEI

Submitted to the Office of Graduate and Professional Studies of
Texas A&M University
in partial fulfillment of the requirements for the degree of

DOCTOR OF PHILOSOPHY

Chair of Committee,	Hong-Cai Zhou
Committee Members,	Abraham Clearfield
	Michael B. Hall
	Perla Balbuena
Head of Department,	David H. Russell

May 2014

Major Subject: Chemistry

ABSTRACT

Metal-organic frameworks (MOFs) are newly emerged porous materials. These inorganic-organic hybrid materials have diverse crystalline structures, high surface areas, and large porosities. This dissertation is focusing on developing new design and synthetic strategies to construct novel MOFs for applications of gas separation, gas storage, and chemical sensing.

In the second section, a linker-extension strategy through hard-soft selective metal-coordination was developed for obtaining nano-sized linkers which would require complicated organic synthesis with traditional methods. A non-rigid MOF named as PCN-91 containing nano-sized metallo-linkers has been synthesized easily using a linear bipolar organic linker with carboxylate and pyrazolato groups on each end.

In the third section, a solid porous copper MOF, PCN-922, was synthesized using a presynthesized zinc MOF, PCN-921, as a template and exchanging the zinc cations to copper cations. It showed good gas adsorption potential for H_2, CO_2 and CH_4. The framework-templating method is useful for growing single crystals which are difficult to produce by direct synthesis methods. Also, the stability of MOFs could be strengthened through the metal cation exchange process.

In the fourth section, rigidifying fluorescent linkers by MOF formation has been proposed and demonstrated as an effective method for building special fluorescent solid materials. A yellow fluorescent linker extended from tetraphenylethylene has been

combined with Zr_6 clusters to form a MOF, PCN-94, showing rarely reported 91% high quantum yield and blue fluorescence with 75-nm blue-shift compared to the linker precursor solids. The extraordinary fluorescent properties are attributed to the structural distortion, and intra-/inter-molecular interaction limitation of the linkers by calculation results.

In the fifth section, tailoring pore size strategy has been proposed for boosting MOFs' volumetric methane storage capacities. PCN-62, which possesses rht-topology, was crystallized and showed 243 v_{STP}/v methane capacity under 65 bar and 189 v_{STP}/v working capacity between 5 and 65 bar.

In summary, three design strategies and one synthetic strategy have been demonstrated successfully for building novel MOFs with excellent properties towards their specific applications. These strategies and findings shed light on fundamental chemical mechanisms and realized practical applications for metal-organic frameworks.

DEDICATION

To my parents and brother, and to all my friends who helped me during my five years of PhD study.

ACKNOWLEDGEMENTS

I would like to thank my committee chair, Dr. Hong-Cai Joe Zhou, and my committee members, Dr. Abraham Clearfield, Dr. Michael B. Hall, and Dr. Perla Balbuena, for their guidance and support throughout the course of this research.

I will always appreciate my advisor, Dr. Zhou, for offering me the great opportunity to work in his lab. He gave me much insightful guidance and pushed me toward success in finishing my degree.

I will also thank all the group members with who I have been working. They are so friendly and patient in helping me. I would especially like to thank Dr. Daqiang Yuan, Dr. Weigang Lu, Dr. Zhi-Yuan Gu and Mr. Dawei Feng. They worked with me closely and provided the best help I can ever have.

Thanks also go to the collaboration from Dr. Daofeng Sun's group in Shandong University, Dr. Gregory J. Halder and Dr. Yu-Sheng Chen in Argonne National Lab BM-17 and ID-15, Dr. Mohammad A. Omary's group in University of North Texas, Dr. Hall's group in Texas A&M University, Dr. Jingbo Louise Liu's group in Texas A&M University-Kingsville, and Dr. Taner Yildirim's group in National Institute of Standards and Technology. Their great work strongly supported and improved the quality of our research.

Thanks also go to my colleagues and the department faculty and staff for making my time at Texas A&M University a great experience.

My friends certainly deserve an acknowledgement. Your help in the five years in research and life have always been important to me.

Then I want to thank my father Jiangchuan Wei, mother Jianhua Zhang, and my twin brother Zhangwu Wei, for their encouragement and love.

Finally, I would like to extend my gratitude to the funding agencies. U.S. Department of Energy (DOE Grants DE-FC36-07GO17033, DOE DE-SC0001015 and DE-AR0000073), part of the Methane Opportunities for Vehicular Energy (MOVE) Program, an ARPA-E Project under Award Number DE-AR0000249. Welch Foundation (A-1725), the National Science Foundation (NSF CBET-0930079), the National Science Foundation/Department of Energy under grant number NSF/CHE-0822838. Use of the Advanced Photon Source was supported by the U. S. Department of Energy, Office of Science, Office of Basic Energy Sciences, under Contract No. DE-AC02-06CH11357. China Scholarship Council.

NOMENCLATURE

BET	Brunauer-Emmett-Teller
DFT	Density Functional Theory
FW	Formular Weight
MOF	Metal-Organic Framework
MOP	Metal-Organic Polyhedron
PCN	Porous Coordination Network
PSM	Post-Synthetic Modification
PXRD	Powder X-Ray Diffraction
Q_{st}	Isosteric Heat of Adsorption
SA	Surface Area
SBU	Secondary Building Unit
TGA	Thermal Gravimetric Analysis
UMCs	Uncoordinated Metal Centers
XPS	X-ray Photoelectron Spectroscopy

TABLE OF CONTENTS

Page

LIST OF FIGURES

Page

LIST OF TABLES

Page

1. INTRODUCTION

After Alfred Werner's explanation of transition metal salt structures in 1893, coordination chemistry started rapid development.[1] In this day and age, one of the newest coordination chemistry areas is metal-organic frameworks (MOFs), which emerged in the middle of the 1990s and is undergoing fast growth.[2-10] MOFs are highly crystalline coordination networks constructed from inorganic metal-based nodes and organic bridging linkers (Figure 1).[5, 11, 12] As a new type of organic-inorganic hybrid porous solids, MOFs exhibit high internal surface area, large porosity, tunable structure, and diverse functionality, compared to other porous materials including activated carbons, mesoporous silica, zeolites, nanotubes, covalent-organic frameworks, metal-organic polyhedra and porous organic molecules.[13-15] MOFs have been extensively studied not only for fundamental interests such as luminescence[16], magnetic[17] and ferroelectric[18] properties, but also for potential practical applications including gas storage,[19-21] chemical separation,[14, 22] heterogeneous catalysis,[23, 24] chemical sensing,[25] biomedicine[26], proton conduction[27], drug delivery[26, 28] and others[29]. Design and synthesis of MOFs with high surface area, low cost, and high stabilities is a sought-after goal.

The basic components of MOFs are inorganic metal ions or metal nodes (secondary building units, SBUs) and organic bridging linkers.[30-32] Their connection numbers, geometries and binding modes determine framework structures.[30] Moreover, different components have their own chemical properties, stabilities, and functions,

capable of being built into resulting MOFs. Hence designing and synthesizing MOFs needs thorough consideration of these elements.

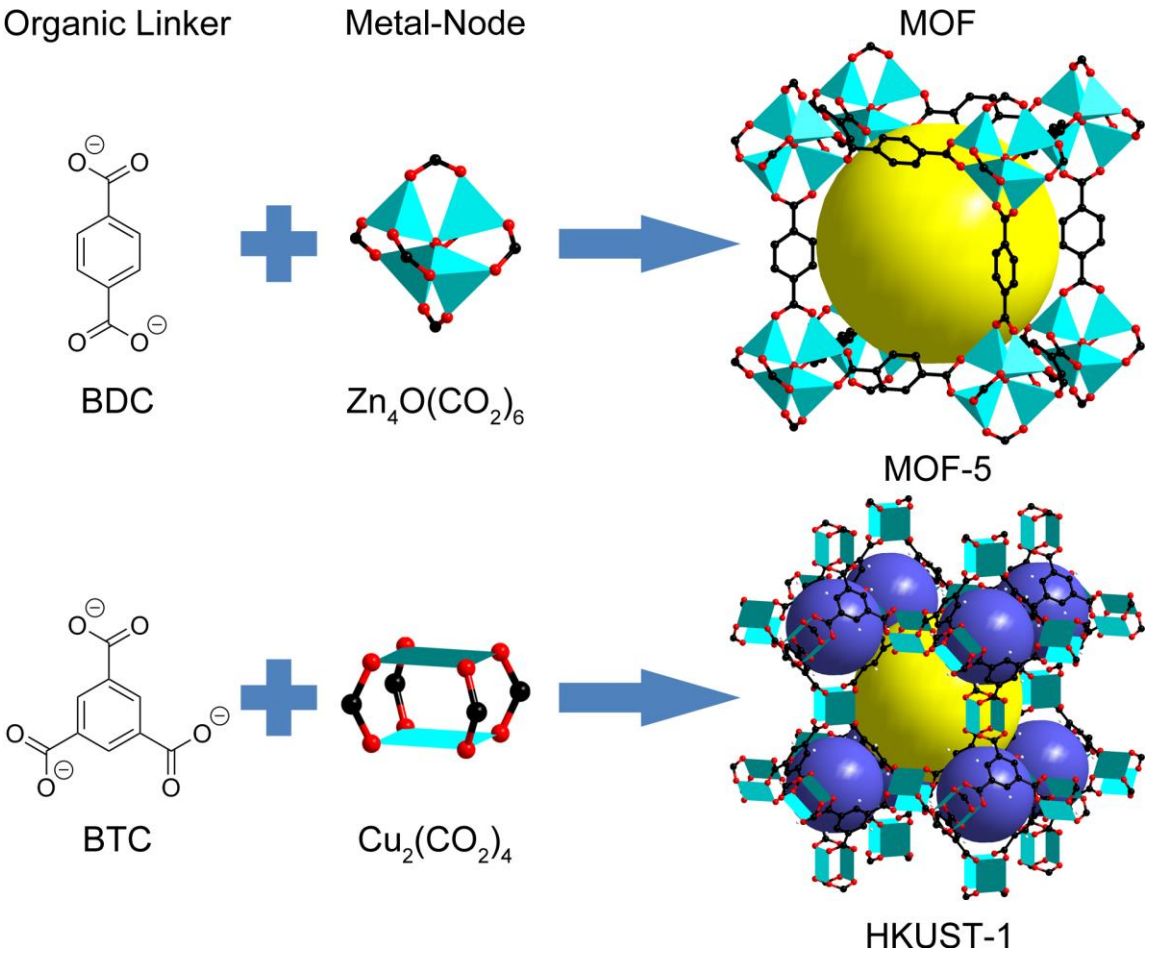

Figure 1. Schematic representation of synthesis of MOF-5 and HKUST-1.

A common SBU is a single or multi-center metal nodes connected by carboxylate groups of linkers (Figure 2).[31, 32] Dozens of metal elements including both main group and transition metals can be used to construct SBUs. Additionally, one metal element could form a discrete metal node with a different quantity of metal centers or an infinite chain with the same linker. For example, Zn, having labile coordination bonds with carboxylate groups, possesses flexible coordination modes and could form Zn_4O SBUs, square paddlewheel SBUs, triangular paddlewheel SBUs,[33] and infinite 1D-chain SBUs.[34] On the other hand, Zr, which strongly coordinates to carboxylate groups, also forms Zr_6 SBUs,[35] Zr_8 SBUs,[36] and 1D-chain SBUs.[37] Moreover, one SBU could provide different connection modes, such as Zr_6 nodes possessing 12-connected, 8-connected and 6-connected modes.[38-41] Besides contributing to the topology, some SBUs also have special properties, such as the unsaturated metal centers (UMCs) of dicopper paddlewheels in HKUST-1 creating their high affinity towards small molecules, such as Hydrogen (H_2).[11] In addition, mixed-metal and nitrogen-coordination (Figure 2f) SBUs have also been produced.[42]

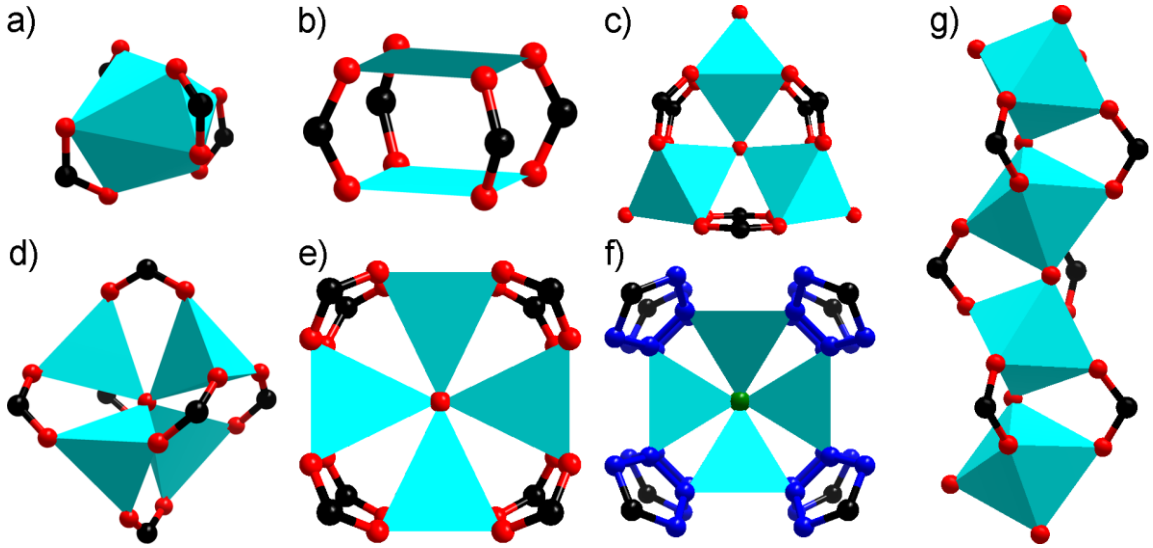

Figure 2. Selected common secondary building units (SBUs) (turquoise, metal; red, oxygen; blue, nitrogen; black, carbon; green, chloride; yellow, others.): a) single metal;[43] b) dinuclear paddlewheel;[44] c) trinuclear prism;[45] d) tetranuclear octahedron;[5] e) tetranuclear prism;[46] f) tetranuclear prism coordinated with a nitrogen donor;[47] g) infinite chain.[48]

Based on powerful organic synthesis techniques, infinitely variable organic linkers designed with different sizes, shapes, binding sites, and functional groups can be synthesized. The size of the linker may be as short as one oxalate[49], or as long as dot-XI with 50 Å length (Figure 3a)[50]. The common carboxylate organic linkers are linear,[5, 50], bending,[51] trigonal,[52, 53] tetragonal,[39, 44] tetrahedral[54, 55] or other geometries containing multiple carboxylate groups (Figure 3).[56] Also, asymmetric linkers are also studied and provide interesting results.[57, 58] Moreover, both rigid and flexible linkers have been synthesized and studied.[54, 59] Recently, linkers using phosphonate groups[60], sulfonate group[61] and heterocyclic compounds[62, 63] as binding sites have also been studied.[62] In addition, different binding sites can be built in one linker and connected to different

SBUs.[64] On the other hand, organic linkers can also be generated *in situ* during the MOF formation.[65]

The combination of inorganic and organic components allow for MOFs with numerous structures to be constructed.[56, 66] To take full advantage of the empty pores, functional groups may be introduced with predesigned organic linkers.[67] Post-synthetic modification (PSM) may also introduce functional groups into the linkers and SBUs of pre-formed frameworks,[68-70] or even exchange the linkers/metal ions[44, 71]. By systematically enlarging the linkers and introducing functional groups while retaining the shape of the linkers and the same SBUs, a series of isoreticular MOFs with identical topologies but various pore sizes and functionalities can be built under closely related reaction conditions, such as IRMOF series, PCN-6X series (Figure 4), and UIO-6X series.[53, 67] Based on synthesis and handling, the same metal ion and linker may yield the same framework with different crystallinity[72], SBUs[55], linker configurations[51] and topologies[73, 74]. Additionally, mixed-linker and mixed-metal strategies can also be used for extending the structure diversity,[75] employing functional groups,[76] and improving performance over MOFs building from single component linkers[77].

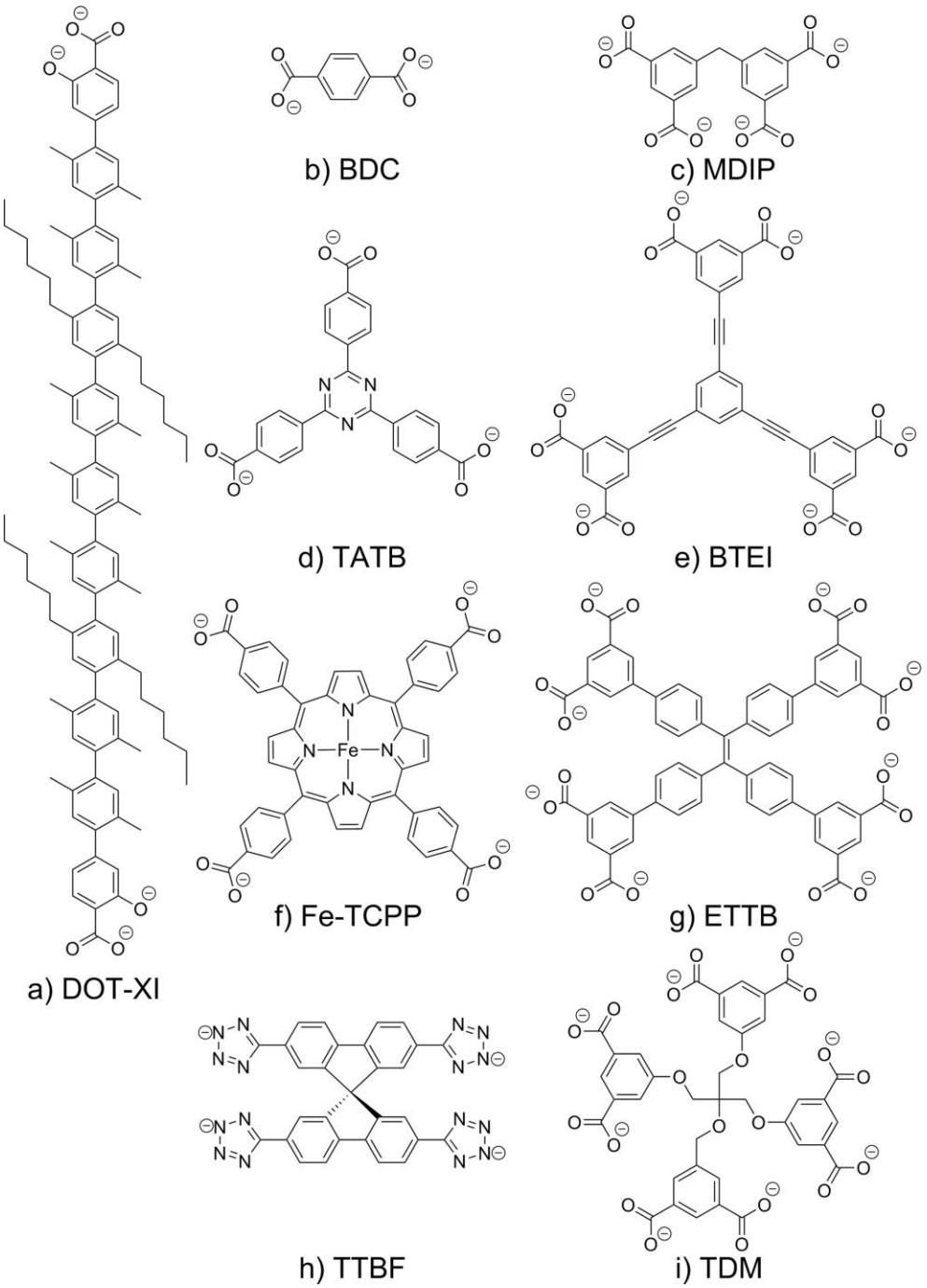

Figure 3. Selected organic linkers with different size, shape and binding sites. a) 50 Å linear ditopic linker;[50] b) short linear ditopic linker;[5] c) bending tetratopic linker;[51] d) trigonal tritopic linker;[52] e) trigonal hexatopic linker;[53] f) tetragonal tetratopic linker;[39] g) tetragonal octatopic linker;[44] h) tetrahedral tetratopic linker with N-binding sites;[55] i) tetrahedral octatopic linker.[54]

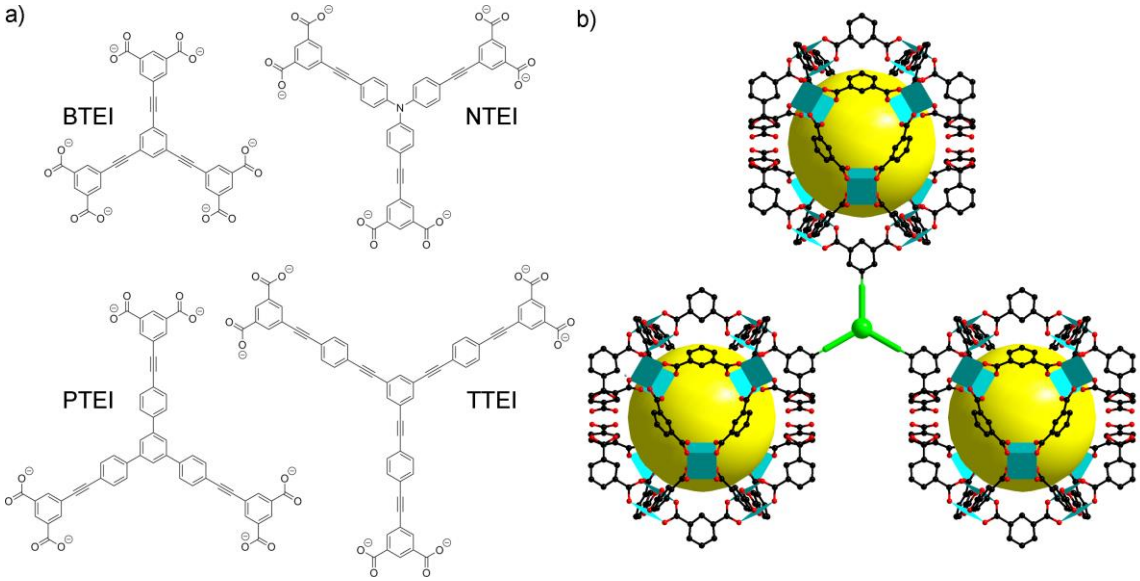

Figure 4. a) Hextatopic linkers for PCN-6X series, btei (PCN-61), ntei (PCN-66), ptei (PCN-68), and ttei (PCN-610); b) (3,24)-network constructed from cuboctahedral in PCN-61.

MOF synthesis has two main purposes: to get high-quality single crystals for structure determination and to get pure phase MOFs which could be crystalline powders. The traditional MOF synthesis, which is based on hydrothermal and solvothermal reactions between organic linker precursors and metal salts in water or high boiling point organic solvents, is commonly used for obtaining single crystals.[78] Other methods including reflux,[79] sonochemical,[80] microwave,[77] electrochemical,[79] mechanochemical,[81] and high-throughput synthesis[82] have also been employed to control the product structure, reaction time, purity, crystallinity, crystal size and shape, scale-up, as well as to grow thin films and membranes.[78, 83] *In situ*[82] and *ex situ*[84] studies of MOF crystallization are performed to extract the reaction status information and optimize the

reaction conditions. Additionally, the effect of solvent, counter anion, structure-directing agent, mineralizer, precursor, blocking agent, modulator, and other additives are widely studied.[78]

Many applications of MOFs are based on their high internal surface and large porosity. MOFs' internal surface and porosity are usually evaluated with N_2 or Ar adsorption at 77 or 87K, respectively.[5, 19, 38] Besides Langmuir theory assuming single layer adsorption, Brunauer-Emmett-Teller (BET) theory concerning multilayer adsorption are commonly used methods for calculating internal surface areas for MOFs with large pores from the sorption isotherm.[19, 85] Free pore volume is also important parameters for assessing adsorption capacity. Pore size and shape also significantly affects diffusion rate and selectivity.[14] X-ray diffraction is commonly used to analyze MOFs' structures and pores.[44] Interestingly, some MOFs can change their pore size and shape through changing the framework or the flexible functional groups upon stimulation.[48, 86, 87] Neutron powder diffraction,[88-90] inelastic neutron scattering,[52] variable-temperature infrared spectroscopy,[91] roman spectroscopy[92] are the main techniques used for locating the guest molecule binding sites, counting their amount, and tracking their status after adsorption. On the other hand, computational modeling not only provides detailed information about the interactions happening on the internal surface which may not be detect by instruments, but also can scan the performance of proposed materials to save time and cost in experiments.[21, 91, 93] The interaction strength between guest molecules and sorbent materials, which is related to storage and separation performance, is evaluated with the isosteric heat of adsorption (Q_{st}).[19] Q_{st} is

obtained by applying the Clausisus-Clapeyron equation to multiple sets of gas adsorption data measured under different and close temperatures.[88, 94]

To achieve the porosity of MOFs, the guest solvent molecules contained in the as-synthesized samples must be removed by a procedure called "activation". The routine activation includes exchanging the strong coordination and high boiling point solvent to weak coordination and low boiling point molecules, followed by a heat-evacuation process.[19] But this crude operation may result in the framework collapse, particularly for MOFs with large pores.[53] Supercritical carbon dioxide (CO_2) activation[95] and freeze-drying activation[96] are employed as efficient methods in these cases.

The diversity and tailorability of MOFs' structure and function can produce countless interesting properties and fulfill a lot of requirements for potential applications. Among them, gas storage and separation, especially H_2 storage,[19] methane (CH_4) storage[20] and CO_2 capture[22] are the most actively studied. Additionally, MOF applications in luminescence will be introduced here.[16]

Fossil fuels are non-renewable energy sources and their usage has produced large amounts of CO_2 which is thought to bring about global climate change. For this reason, many scientists are seeking new clean energy sources, like H_2 and CH_4, as well as capturing the released CO_2. Porous materials could effectively separate, capture and reversibly store these energy related gases. MOFs' large internal surface and pore volume make them promising candidates.[19, 20, 22]

Due to favorable energy density and a pollution-free nature, H_2 is an acceptable alternative to traditional fossil fuels. However, one key factor in preventing the

commercialization of H_2 as fuel is that there are no efficient and cheap methods for storage. Compression and liquefaction methods require big and heavy containers as well as large amounts of energy. Chemisorptions of hydride compounds with high Q_{st} suffer from strong binding of H_2 that results in limited release /recharge rate, thus requiring additional energy. Alternatively, porous materials including MOFs could store H_2 by physisorption with lower Q_{st}.[19, 97, 98]

MOFs' BET surface area is shown to be qualitatively linear with their H_2 storage capacity under 77 K and high pressure, according to experiments and computational simulations.[19] Enlarging the size of organic linkers of known MOFs may be the simplest way to obtain new MOFs with high surface area under a given topology. By adopting this strategy, our group reported the isoreticular PCN-6X series with large BET surface area and high H_2 uptake capacities (Figure 4).[53] Recently Hupp *et al* has reported two MOFs, NU-109E and NU-110E, which are both constructed from the hexatopic linkers with 17 Å radiuses.[99] The BET surface areas for NU-109E and NU-110E have reached 7010 and 7140 $m^2 g^{-1}$, respectively, which break the record held by NU-100 and MOF-210.[75, 100] However, linker extension requires multistep organic synthesis which is time-consuming, high cost and low yield. Mixed-linker systems composed of simple and short linkers could yield MOFs with rare topologies and higher surface areas that cannot be generated from a single linker. With two relatively simple linkers, MOF-210 is constructed possessing BET surface area 6240 $m^2 g^{-1}$.[75] However, this method needs a large number of scanning reactions and relies on high-throughput synthesis.

At the same time, increasing the interactions between the H_2 molecules and frameworks is also important for improving the adsorption capacities.[19] Comparison between interpenetrated PCN-6 and non-interpenetrated PCN-6' demonstrates that catenation or interpenetration could increase the low pressure H_2 storage because of the enhanced interactions between H_2 and multi-walls of the small pores.[52] On the other hand, choosing SBUs which could generate uncoordinated metal centers (UMCs), or incorporating UMCs on the organic linkers can considerably increase the Q_{st}.[88, 94] PCN-12, reported by our group, has significantly increased Q_{st} by close-packing unsaturated Cu centers, and holds the record for low pressure H_2 uptake (Figure 5).[51] UMCs may also be incorporated through the introduction of metal cations into MOFs by either constructing anionic frameworks,[101] or transforming neutral groups into ionic groups.[102] In addition to normal UMCs, spillover mainly based on platinum and palladium has been studied, which will break the H-H bonding to form single atoms attached to the framework.[103] In addition, introducing different neutral functional groups has a minor effect on the H_2 storage; however, calculations have shown that electron-donating groups can enhance the gas uptake.[94, 104]

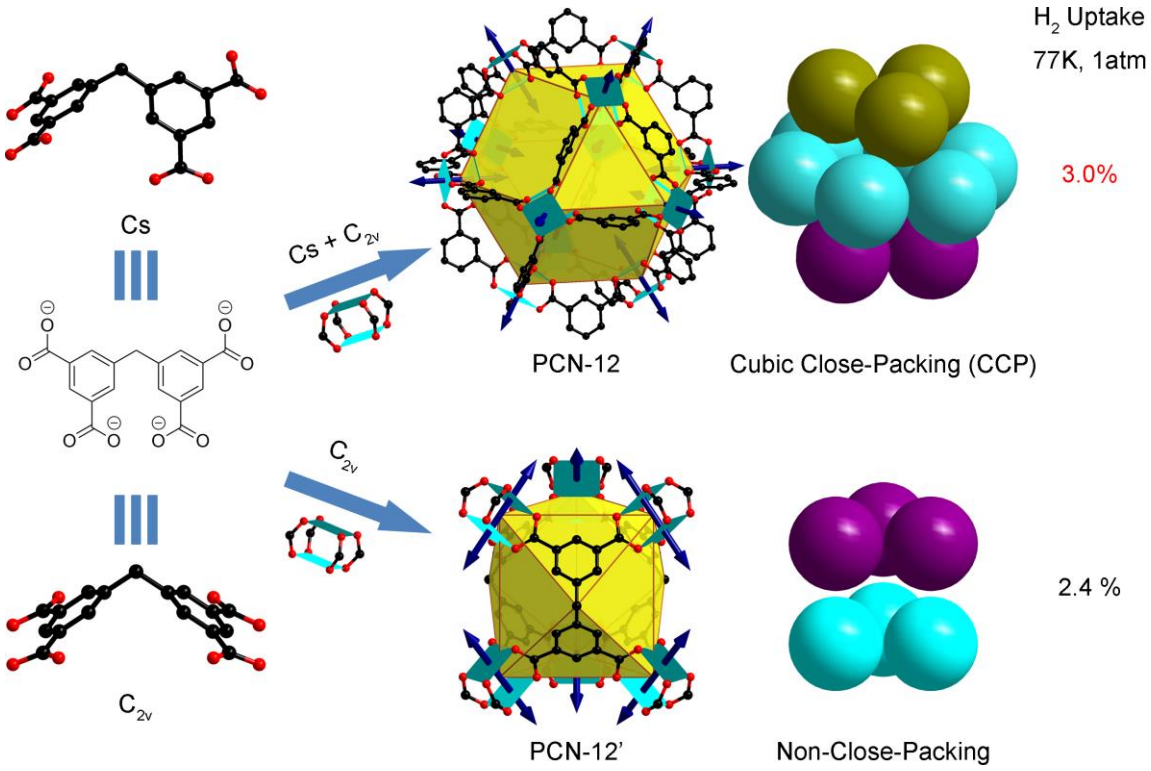

Figure 5. The linker, linker conformation, synthesis, open metal site alignment, and hydrogen uptake of the two MOFs: PCN-12 and PCN-12'. Color scheme: C, black; Cu, turquoise square; O, red; cavities, yellow; open metal site, blue arrow.

Natural gas, which is mainly composed of CH_4, has an energy density comparable to gasoline while releasing less CO_2 in burning. Considering that natural gas is relatively abundant, readily available and much cheaper than gasoline, natural gas can replace gasoline before the H_2 system becomes commercialized. To overcome the high expense, safety issues, and energy consumption of liquefied natural gas (LNG) and compressed natural gas (CNG) systems, adsorbed natural gas (ANG) systems has been proposed to work under ambient temperature and between pressures of 5~35 bar.[20]

Similar to H_2 storage, CH_4 storage requires that adsorbents have proper internal surface area and Q_{st}. However, CH_4 has a highly symmetric and constrained shape showing no permanent dipole or quadrupole moment. Therefore, CH_4 is less sensitive toward polar metal cations and functional groups.[20] Consequently, adding polar ions or functional groups have diminished ability to increase Q_{st}. In addition, increasing strong binding sites may decrease the working capacity since more CH_4 molecules are retained under low pressure (~5 bar), despite the total uptake inflation. According to calculations, organic linkers are the major adsorption site in common MOFs which have low SBU density.[20, 89, 90, 92] Building micropores for packing multiple CH_4 molecules has been proven to be the most effective way to increase uptake.[20] Experimental and computational studies have shown that BET surface areas in the range of 2500~3000 $m^2 g^{-1}$ are optimal for CH_4 storage.[93] Larger BET surface area usually means larger pores which reduce the interaction between the molecules and frameworks. CH_4 uptake capacities can be enhanced by building ~4 Å or ~7.75 Å micropores or mesopores separated with pendant lipophilic alkyl chains on the aromatic linkers.[93] Our group reported PCN-14 which possesses both small pores and high density of UMCs having a total uptake 230 (v/v) at 290K and 35 bar which continues to be the record holder for CH_4 high pressure volumetric uptake (Figure 6).[20, 105] In order to utilize MOFs as adsorbent for CH_4 storage, their properties such as pore size, pore shape, density and surface area must be carefully balanced to achieve optimal potential.[20]

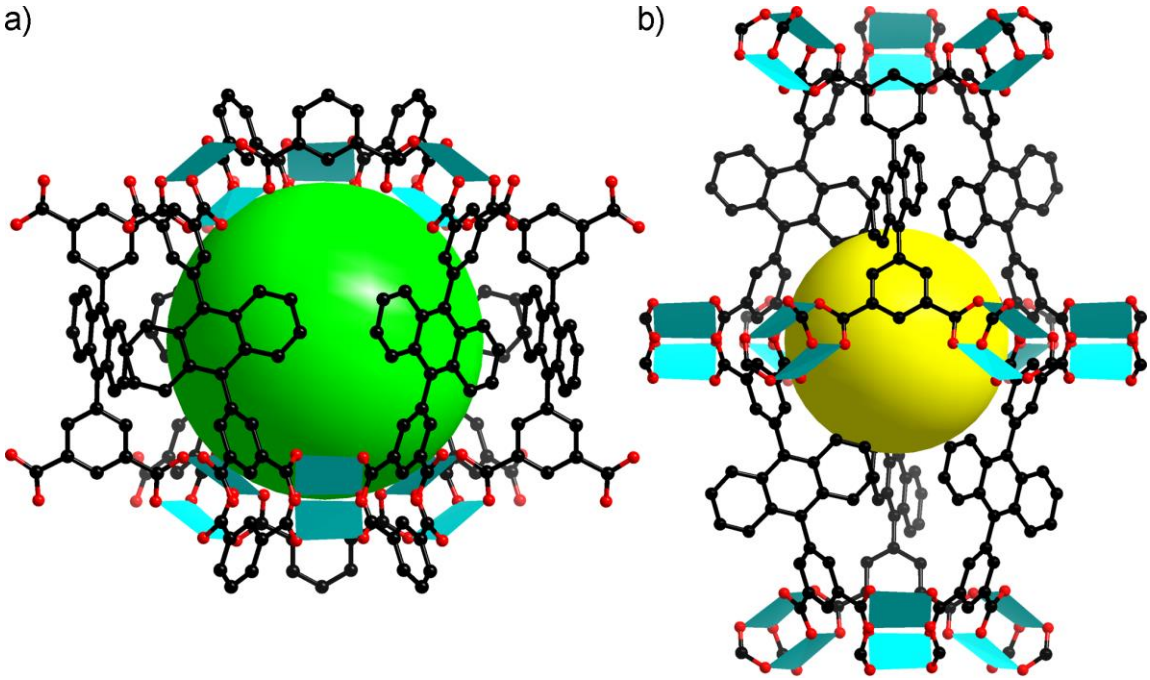

Figure 6. a) Large cage in PCN-14; b) small cage in PCN-14. Color scheme: C, gray; Cu, turquoise square; and O, red.

Although clean energy is the ultimate solution for solving the energy and environmental issues faced by human beings, the relevant research still needs further improvement. Capturing the large amount of CO_2 from fossil fuel power plants is considered equally important for preventing climate change disaster. Carbon capture options include pre-combustion combustion capture, oxy-fuel, and post-combustion capture. Among them, capturing the CO_2 from the flue gas after combustion has been intensively studied due to the easy collaboration with current systems. Flue gas is composed of primarily N_2, with the remaining components being a mixture of ~15% CO_2, as well as a small amount of other gases including H_2O, CO, SO_x, NO_x. Thus the post-combustion CO_2 capture requires the adsorbent selectively adsorb CO_2 from the gas

mixture, regenerate with small energy penalty, stay intact under heat and impurities, and be cost-effective. The amine-scrubbing technique used for current systems could consume more than 30% of the energy produced by the power plant while suffering corrosion and solvent boil-off issues.[106] Solid sorbent materials based on physisorption need much less energy for regeneration and attract attention. MOFs are promising candidates based on their hydrophobic internal surface, functionality, high porosity, and high uptake compared with traditional porous materials including zeolites and activated carbons.[22]

As mentioned above, because CO_2 only composes 15% of the flue gas, it is important for the sorbent to selectively capture CO_2 under 0.15 bar partial pressure. Selectivity usually comes from size-based selectivity and adsorptive selectivity. Besides rigid MOFs with small pores,[107] some flexible MOFs only open the pores for CO_2,[87] and some other MOFs have flexible functional groups acting as gates to control the gas entrance[86].

CO_2 has strong quadrupole moment and polarizability compared to N_2. Through increasing the polarity of the internal surface of the adsorbent, MOFs' adsorption selectivity toward CO_2 can be effectively increased. In this context, the BET surface area is not as important as in hydrogen storage since it mainly affects gas uptake at high pressure range.[22] First, alkylamines are expected to capture the CO_2 based on acid-base interaction and polarization. Strong coordination of amine groups results in no examples of directly building MOFs with linkers appending alkylamine. However, introducing alkylamines on SBUs or organic linkers by post-synthetic modification (PSM)

successfully increased the Q_{st} and CO_2 selectivity under low pressure.[69, 70] Second, various MOFs based on N-containing heterocyclic linkers[63] and aromatic amine groups[108] have been synthesized and examined for CO_2 adsorption. However, their moderate effect on CO_2 capture ability are mainly attributed to the surface polarization caused by heteroatoms.[22] Functional groups with strong polarity except amines have also been incorporated into MOFs including halide, thio, cyano, hydroxyl, and nitro groups. Systematically introducing these groups into a series of isoreticular MOFs has been performed in experimental and computational studies to evaluate functionalization modification effects on CO_2 adsorption behavior. It was found that functional groups with stronger polarity will result in a higher CO_2 affinity.[76, 109] The appended groups reduce the pore size and enhance the CO_2 interactions, further improving the selectivity.[110] Finally, the UMCs provide charge-dense binding sites for CO_2. PCN-88 reported by our group can effectually capture CO_2 molecules between two precisely designed UMCs (named as single molecular traps).[111] In fact, Mg_2(dobdc), with a huge amount of unsaturated magnesium ions in its pores, shows the highest volumetric and gravimetric CO_2 adsorption capacity in the low-pressure range (Figure 7).[112]

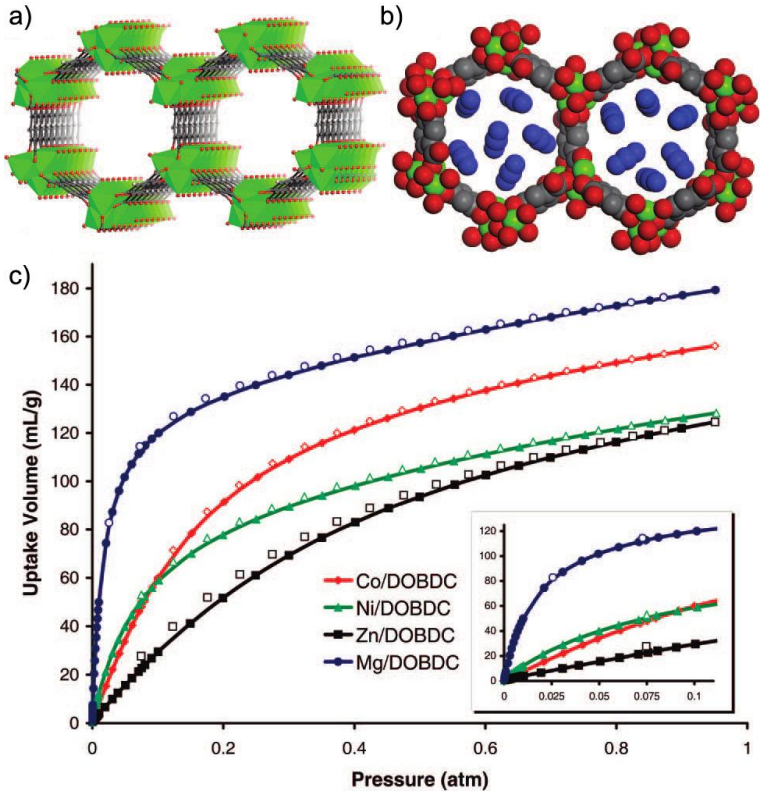

Figure 7. a) View of 1D channels present in the M_2(dobdc) structure (solvent omitted); (b) space-filling model of the pore structure of 1 unit cell of Mg_2(dobdc) (Mg atoms, gree; C atoms, gray; O atoms, red; H atoms and solvent molecules removed for clarity) occupied by 12 molecules of CO_2 (blue) which represents the sorption at 0.1 atm and 296K; c) CO_2 sorption isotherm (296 K, 0 to 1 atm) comparing Mg(dobdc) series, along with an inset of the low pressure region from 0 to 0.1 atm (filled markers represent adsorption points; open markers represent desorption points). Reprinted with permission from ref. 112.[112] Copyright 2008 American Chemical Society.

Luminescence is another important property of MOFs. It may come from not only the inorganic SBUs or organic linkers separately, but also the charge transfer between SBUs and linkers.[16] Rigid, separate SBU/linkers in the framework reduce the intermolecular energy transfer and vibrational quenching, and could increase the luminescence intensity, lifetime and quantum yield, as well as shift the spectra. Porous

MOFs can also capture guest molecules which can either cause luminescence or interfere with the framework luminescence by quenching/enhancing intensities or shifting the spectra. [16]

MOFs combining biocompatibility, tunability, crystallinity, and large porosity, are promising candidates for drug delivery. The direct incorporation strategy allows for a drug to be synthetically incorporated into MOFs and released through controllable decomposition.[28] Coating the microwave produced nanoscale MOFs with silica or organic polymers may further control the release rate. The post-synthetic loading strategy loads the drug into the empty pores and the drug is then released by diffusion.[113] Although MOFs with large pores can directly adsorb drug molecules and bind them with weak Van der Waals interaction, functionalized MOFs could bind the drug strongly and precisely control the release rate.[26, 28, 114]

MOFs possess both characteristics of inorganic and organic materials. The well-developed synthetic methods can be utilized to precisely tune the structure, functionality and performance of these materials. Therefore, these amazing materials can be applied into various areas. In the future, MOFs have to be examined in real world industrial conditions, such as for separations. Further research will be needed to address relatively low physical and chemical stability of MOFs in comparison to traditional porous materials. New MOF families based on high valence metal ions such as zirconium and aluminum[115] should get more attention and development. MOF performance on adsorption, separation, catalysis, and chemical sensing should be tested through scale-up. Current MOF research has greatly benefited from inter-disciplinary study; however,

further collaboration between MOF researchers, organic chemists, inorganic chemists, computational chemists, biochemists, material scientists, and engineers will bring more knowledge about synthesis, characterization, application prospect, as well as helping to commercialize these useful materials.

2. LINKER EXTENSION THROUGH HARD-SOFT SELECTIVE METAL COORDINATION FOR THE CONSTRUCTION OF A NON-RIGID METAL-ORGANIC FRAMEWORK*

2.1 Introduction

Compared to traditional porous materials such as zeolites and activated carbons, MOFs are known for their tuneable pore structures, extraordinarily high surface areas, and adjustable surface properties.[15, 98] These properties give MOFs great application potential in gas storage and separation, most notably, hydrogen and methane storage as well as carbon dioxide capture.[14, 19, 22, 25, 26, 28, 74, 116-124]

Prior work of others and ours has demonstrated that high-pressure gravimetric hydrogen-adsorption capacity of a MOF is proportional to its internal surface area.[97] In fact, a large specific surface area is one of the main prerequisites for MOF applications, especially for gas storage. Strategies to reach higher surface area thus become a sought after goal. Extension of the length of an organic linker through organic synthesis has become the most direct method to reach this target.[53, 56, 75, 125] Another approach is to use metal coordination to combine several short organic linkers into a nano-sized linker.[126, 127] This approach is limited by the competition between framework assembly and

* Springer and Science China-Chemistry, 56, 2013, 418-422, Linker extension through hard-soft selective metal coordination for the construction of a non-rigid metal-organic framework, ZhangWen Wei, DaQiang Yuan, XiaoLiang Zhao, DaoFeng Sun, Hong-Cai Zhou, Copyright 2013 is given to the publication in which the material was originally published, by adding; with kind permission from Springer Science and Business Media.

metallolinker formation. One strategy to overcome such a competition is to differentiate the two procedures by using two distinct sets of donor groups and metal ions. For instance, a bipolar linker containing both a "hard" and a "soft" end can be used to coordinate selectively with a "hard" metal and a "soft" metal, respectively.[128] In this communication, we report a flexible metal-organic framework possessing Pt_3O_4-net topology constructed from a metal-coordination-extended linker using such a strategy.

In order to obtain metal-coordination-extended linkers, the short organic linker should be a bi-polar linker in which each end has its preference to a different type of metal ion. It is known that the soft nitrogen donor atoms of a pyrazolate or its derivatives can preferentially bind the Cu(I) ions to form a Cu(I) triangle node (Figure 8a).[129-131] Hence, we designed and synthesized a new bi-polar linker, namely 4-(4-carboxylatophenyl)-3,5-dimethylpyrazolate (dmpba), which can connect to different metal ions with each end to construct MOFs (Figure 8b).

It has also been documented that Cu(II) ions can be reduced to Cu(I) ion by N-containing compound or solvent.[132] Thus, Cu(II) salts were chosen as the starting materials for MOF synthesis.

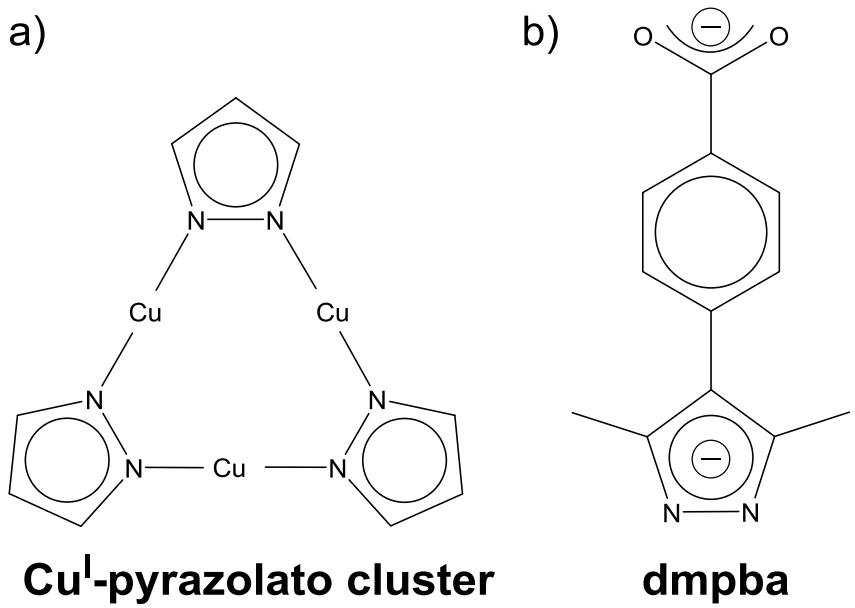

Figure 8. a) The tri-copper unit (simplified); b) 4-(4-carboxylatophenyl)-3,5-dimethylpyrazolate (dmpba).

2.2 Experimental Section

General information. Commercially available reagents were used as received without further purification. Elemental analyses (C, H, N) were obtained on a Perkin-Elmer 240 elemental analyzer. Nuclear magnetic resonance (NMR) data were collected on a Mercury 300 MHz spectrometer. Thermogravimetry analyses (TGA) were performed under N_2 on a SHIMADZU TGA-50 TGA, with a heating rate of 4 ℃ min^{-1}. X-ray photoelectron spectra (XPS) were acquired with Axis Ultra DlD (Kratos) equipped with Al monochromatic X-rays operating at 12 kV and 10 mA. Powder X-ray diffraction (PXRD) patterns were obtained on a BRUKER D8-Focus Bragg-Bretano X-ray Powder Diffractometer equipped with a Cu sealed tube (λ = 1.54178) at a scan rate of 0.2 s deg^{-1}, solid-state detector, and a routine power of 1400 W (40 kV, 35 mA).

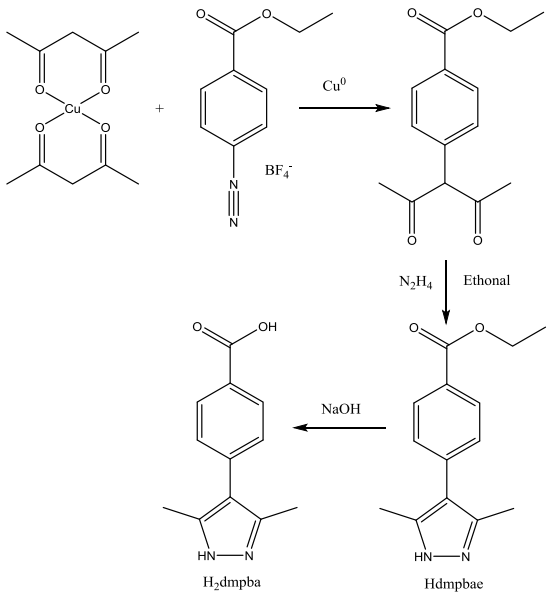

Figure 9. Schematic representation of synthesis route for H_2dmpba and Hdmpbae.

Synthesis of $Cu(acac)_2$ (acac stands for acetylacetone). The synthetic route of H_2dmpba is shown in Figure 9.The preparation of $Cu(acac)_2$ was according to the literature method.[133] Copper(II) acetate (0.2 mol), acetylacetone (25 mL) and sodium acetate (0.2 mol) was reflux in methanol for 2 hours. The thin blue needle-like crystals were filtered out, washed with 50 mL of ether and then dried under vacuum.

Synthesis of diazonium tetrafluoroborate. The preparation of the diazonium tetrafluoroborate was according to the literature method.[134] 0.2 mol of ethyl 4-aminobenzoate was dissolved in 30 mL HBF_4 (48%) and 30 mL water. The solution was cooled to -10 ℃ . 0.2 mol $NaNO_2$ in water solution was added slowly under disturb. After 10 mins, the yellow solid was filtered out, washed with 50 mL cold methanol and 50 mL ether. The yellow product was dried under vacuum at 0 ℃ .

Synthesis of 4-(1-acetyl-2-oxopropyl)-benzoyl ethyl ether. The preparation of 3-subtituted acetone acetate was according to the literature method.[135, 136] The dried $Cu(acac)_2$ and 13 g Cu powder was put into a 1000 mL flask on vacuum line. 300 mL dried dichloromethane (CH_2Cl_2) and 25 mL acetylacetone were added. The diazonium salt was added into the flask under the nitrogen. Formation of nitrogen was observed immediately after the addition of the diazonium salt. The mixture was disturbed under the nitrogen for 12 hours. The organic solution was partitioned with 1N HCl (4 x 100 mL) and dried with Mg_2SO_4. The solvent was evaporated on rotary evaporator. Excess acac was removed at 85 degree on rotary evaporator. The residue was eluded through silica-gel column using 10% ether acetate/hexane. The yellow solution was dried on rotary evaporator. 30 mL hexane was added. The solution was kept in -18 °C to yield

light yellow crystal. ^{1}H NMR: 1.35 (tri, 3H), 1.83 (s, 6H), 4.34 (tetra, 2H), 7.21 8.02 (AA'BB' system, 4H).

Synthesis of ethyl 4-(3,5-dimethyl-1H-pyrazol-4-yl)benzoate, Hdmpbae. 8g yellow crystal of 4-(1-acetyl-2-oxopropyl)-benzoyl ethyl ether was dissolved in 95% ethanol. 1 equivalent of hydrazine hydrate was added to the solution. The solution was refluxed for 2 hours and then dried on rotary evaporator. The solid was dissolved in ether and washed with brine. The organic layer was separated and dried again. The yellow solid was recrystallized in $CHCl_3$/pentane to yield light yellow needle liked crystal of Hdmpbae. ^{1}H NMR: 2.17 (s, 6H), 7.36 7.92 (AA'BB' system, 4H).

Synthesis of 4-(3,5-dimethyl-1H-pyrazol-4-yl)-benzoic acid, H_2dmpba. Hdmpbae (0.55 g, 2.25 mmol) was suspended in 50 mL of THF (tetrahydrofuran) and 50 mL of methanol, to which 30 mL of 5 M KOH aqueous solution was added. The mixture was stirred under reflux for overnight. Organic solvent was removed using a rotary evaporator, and diluted hydrochloric acid was added to the remaining aqueous solution until it became acidic (pH = 2 ~ 3). The precipitate was collected by filtration, washed with water and dried under vacuum to give H_2dmpba as a white solid. Yield: 80%. ^{1}H NMR (300 MHz, DMSO-d_6): δ = 2.22 (s, 6H), 7.41 (d, 2H), 7.95 (d, 2H).

Synthesis of PCN-91. 5 mg H_2dmpba, 15 mg $Cu_2(NO_3)_2$, 1.6 mL *N*,*N*-dimethylacetamide (DMA) and 2 drops of pyridine were mixed in a sealed glass tube. Then the mixture were heated in 120℃ oven for overnight. Big green crystals were formed. Anal. Calcd. (%) for PCN-91, $C_{157}H_{273}Cu_9N_{33}O_{46}$: C, 47.97; H, 7.00; N, 11.76%. Found: C, 47.72; H, 7.69; N, 12.25%.

Synthesis of compound 1. In a glovebox, 5 mg Hdmpbae, 15 mg $Cu(CH_3CN)_4BF_4$, 1.6 mL THF were mixed in a small vial. Then the mixture was heated to 100 ℃ and get crystals.

X-ray crystallography. Crystallographic data for compound **1** were collected on a Bruker Smart APEXII CCD diffractometer with MoK_α (λ = 0.71073 Å) at low temperature. Single-crystal X-ray data of PCN-91 were collected on beamline 15ID at the Advanced Photon source in Argonne National Laboratory. All structures were solved by direct method and refined by full-matrix least-squares on F^2 using *SHELXTL*. The solvent molecules are highly disordered, and attempts to locate and refine the solvent peaks were unsuccessful. Contributions to scattering due to these solvent molecules were removed using the *SQUEEZE* routine of *PLATON*; structures were then refined again using the data generated. Solvent-accessible volume was calculated using PLATON.[137] The simulated PXRD spectra were obtained by the diffraction-crystal module of the *Mercury* program based on the single-crystal data. The program is available free of charge via internet at *http:/www.iucr.org*.

Table 1. Crystal Data for PCN-91 and compound **1.**

Compound	PCN-91	**1**
CCDC number	848655	848659
Formula	$C_{77}H_{65}O_{14}N_{13}Cu_9$	$C_{84}H_{90}O_{12}N_{12}Cu_6$
Formula weight	1968.28	1840.92
Crystal size (mm^3)	0.16 x 0.14 x 0.13	0.40 x 0.40 x 0.30
Crystal system	Tetragonal	Triclinic
Space group	$P4_2$ /nmc	*P*-1
a, b, c (Å)	39.705(6), 39.705(6), 27.201(4)	9.454, 19.435, 23.647
α, β, γ (°)	90, 90, 90	94.28, 91.84, 98.88
V ($Å^3$)	42881(12)	4276.5
Z	8	2
$d_{calc.}$ (g cm^{-3})	0.610	1.430
μ (mm^{-1})	0.474	0.474
T (*K*)	95(2)	240(2)
F(000)	7928	1896
θ range for data collection (°)	0.74 to 14.10	0.86 to 28.51
Reflections collected / unique	265460 / 18514	27227 / 20249
R(int)	0.1838	0.1094
Observed data [I>2σ(I)]	6004	3898
Data/restraints/parameters	18514 / 108 / 346	20249 / 1 / 1045
Completeness to θ_{max}	97.5%	93.3 %
GOF on F^2	0.946	0.706
*R*1, *wR*2 [I > 2σ(I)]	0.1076, 0.2579	0.0541, 0.1259
*R*1, *wR*2 (all data)	0.3095, 0.3362	0.2877, 0.1788

Gas adsorption measurements. The low-pressure nitrogen and hydrogen sorption isotherm measurements were performed at 77 K and 0-760 Torr on an ASAP 2020 surface area and pore size analyzer with ultra high purity (UHP) gases. An as-isolated sample of PCN-91 was immersed in methanol for 24 h, and the extract was decanted. Fresh methanol was subsequently added, and the crystals were allowed to stay for an additional 24 h to remove the nonvolatile solvates (DMA and water). The sample was collected by decanting and treated with dichloromethane similarly to remove methanol solvates. After the removal of CH_2Cl_2 by decanting, the sample was activated by drying under a dynamic vacuum at room temperature overnight. Before the measurement, the sample was dried again by using the "outgas" function of the surface area analyzer for 5 h at 50 °C. Nitrogen and hydrogen isotherms at 77 K were measured in liquid nitrogen baths using ultra high pure (UHP) grade gases. Oil-free vacuum pumps and oil-free pressure regulators were used to prevent contamination of the samples during the degassing processes and isotherm measurements.

2.3 Results and Discussion

The solvothermal reaction of the acid form of dmpba (H_2dmpba) and $Cu(NO_3)\cdot 2.5H_2O$ in DMA in the presence of pyridine (Py) gave rise to large block crystals of a MOF designated PCN-91. Single X-ray diffraction revealed that PCN-91 is a porous MOF with the formula of $Cu^{I}_6Cu^{II}_3(dmpba)_6(Py)(H_2O)_2\cdot 20DMA\cdot 12H_2O$, which was further confirmed by elemental analysis (EA), thermal gravimetric analysis (TGA) and X-ray photoelectron spectroscopy (XPS) (Figure 10, Figure 11).

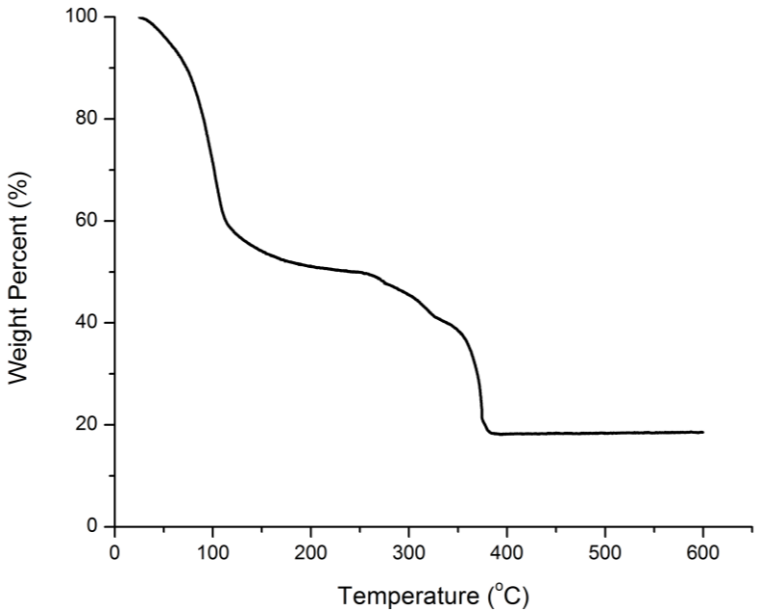

Figure 10. TGA curves of PCN-91.

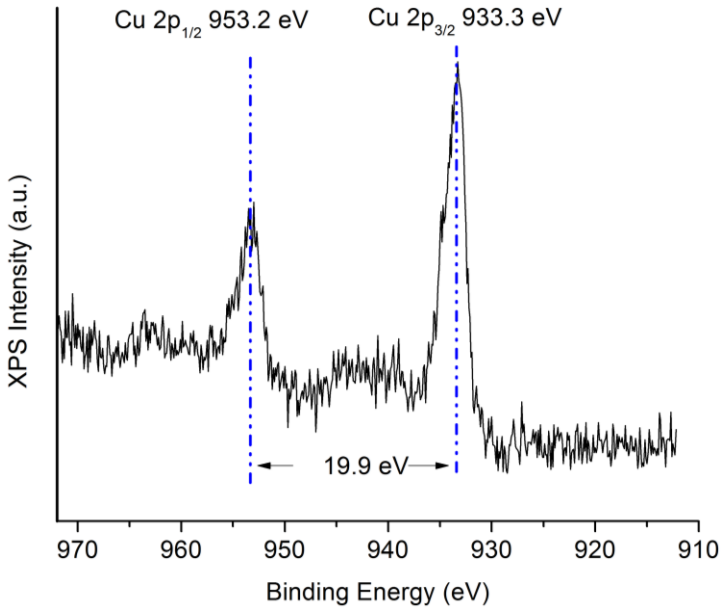

Figure 11. Binding energy of Cu 2p orbitals in PCN-91. The XPS indicates the appearance of Cu(I) ions. The peak at 933.3 eV is shifted toward from 933.5 eV (CuO) toward 933.2 eV (Cu_2O). And there is a clear shoulder on 933.2 eV. Moreover, the distance of two peaks is shortened to 19.9 eV compare to 20.0 eV in CuO.[138]

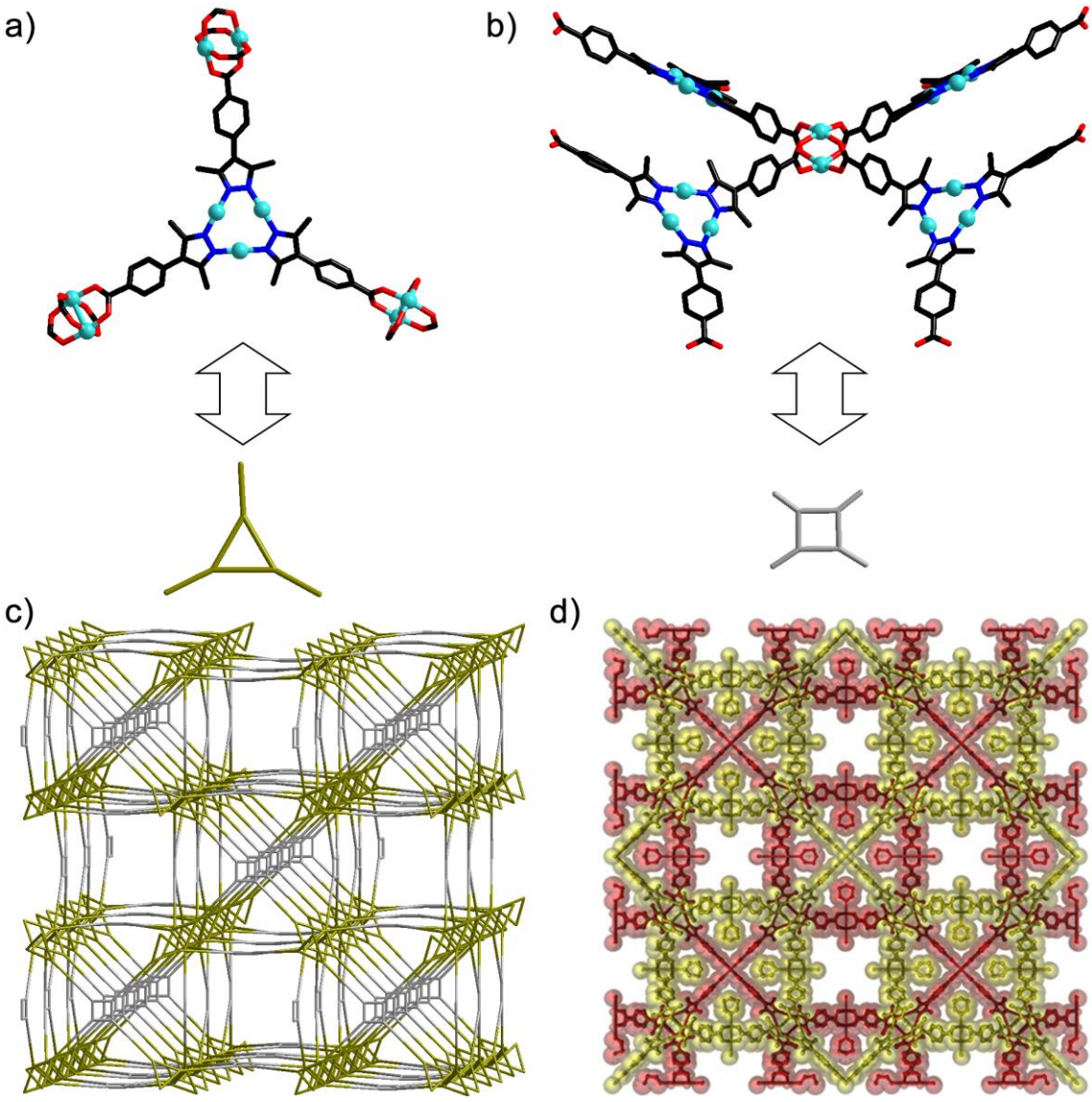

Figure 12. a) Cu^{I}-dmpba connect to 3 Cu_2 paddlewheel SBU, b) a di-copper paddlewheel SBU connected with 4 Cu^{I}-dmpba; c) the Pt_3O_4-net in PCN-91; d) the 3D framework of PCN-91 along *c* axis showing interpenetration.

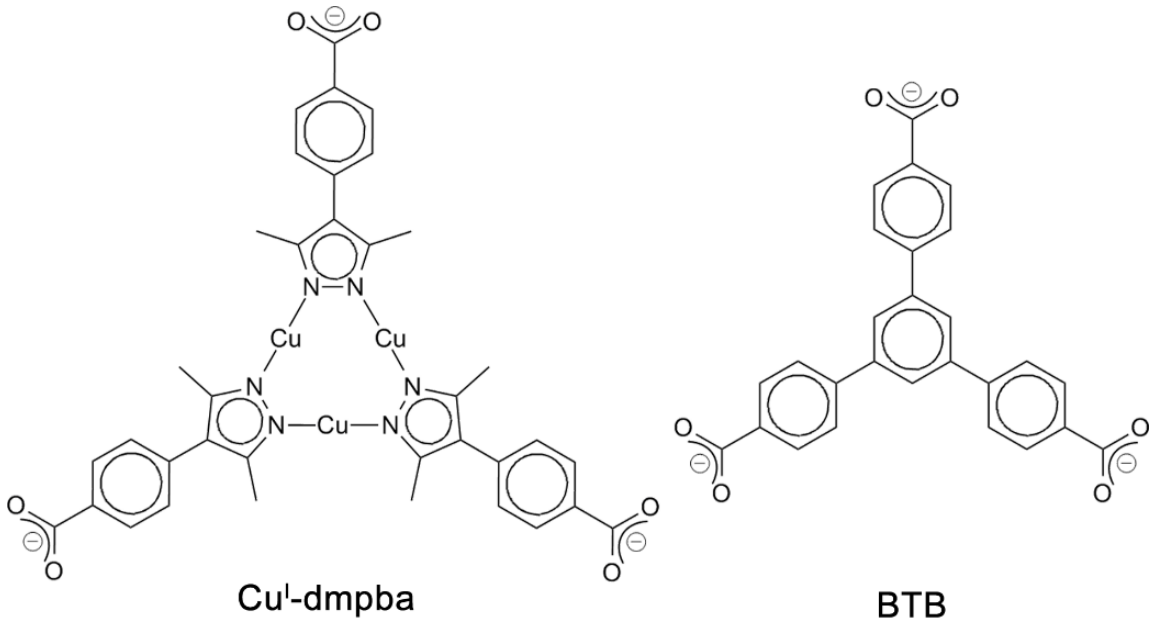

Figure 13. Extension of the non-planar linker.

In the crystal structure, there is one metal-coordination extended linker, Cu^{I}-dmpba, which consists of three dmpba short linkers and three Cu(I) ions (Figure 12). Clearly, Cu(II) ions were partially reduced to Cu(I) ions by an unidentified reducing agent. Every three of these Cu(I) ions selectively coordinate three soft nitrogen donor atoms of three dmpba linkers to form a Cu(I) triangle with an average Cu^{I}···N distance of 1.831 Å and an average Cu^{I}···Cu^{I} distance of 3.185 Å. These distances are comparable to those of other Cu(I) triangles of the same type.[129-131] It should be pointed out that the Cu^{I}-dmpba linker is non-planar, which is very similar to previously reported BTB (4',4'-henzene-1,3,5-triyl-tribenzoate) and TCBPB (1,3,5-tris(4′-carboxy[1,1′-biphenyl]-4-yl-) benzene) linkers, but quite different from our previous reported planar TATB (4,4,4-*s*-triazine-2,4,6-triyltri benzoate) (Figure 13).[139-141] The three pyrazolato rings and Cu(I)

ions are almost in the same plane and the average dihedral angle between a pyrazolato ring and a peripheral ring is 43.98º, slightly larger than those found in BTB and TCBPB.

Each carboxylate group of a Cu^{I}-dmpba linker selectively coordinate to two Cu(II) ions to form a Cu_2 paddlewheel secondary building unit (SBU) (Figure 12b), leading to a porous 3D framework. The large pores resulted destabilize the framework, thus a two-fold interpenetration is necessary to stabilize the MOF (Figure 12d); attempts to obtain a non-interpenetrated MOF were unsuccessful. If the Cu^{I}-dmpba metal-coordination-extended linker and the Cu_2 paddlewheel SBU can be considered as a 3-connected node and 4-connected node, respectively, the framework possesses Pt_3O_4-net topology (Figure 12c). The solvent accessible volume of PCN-91 is 71.0% (30457.7 $Å^3$ per 48391.0 $Å^3$) calculated using PLATON.[137] The interpenetrated framework possesses 1D channels with dimensions of 13.524 × 13.524 Å. TGA showed that PCN-91 is stable up to 270 °C (Figure 10). N_2 sorption at 77 K for PCN-91 was examined and a type-I isotherm was observed. The BET surface area, Langmuir surface area and total pore volume are calculated as 659.0 $m^2 g^{-1}$, 761.9 $m^2 g^{-1}$ and 0.27 $cm^3 g^{-1}$ (Figure 14). The gas adsorption capacities of PCN-91 for H_2, CO_2 and CH_4 were evaluated (Figure 15 to Figure 20).

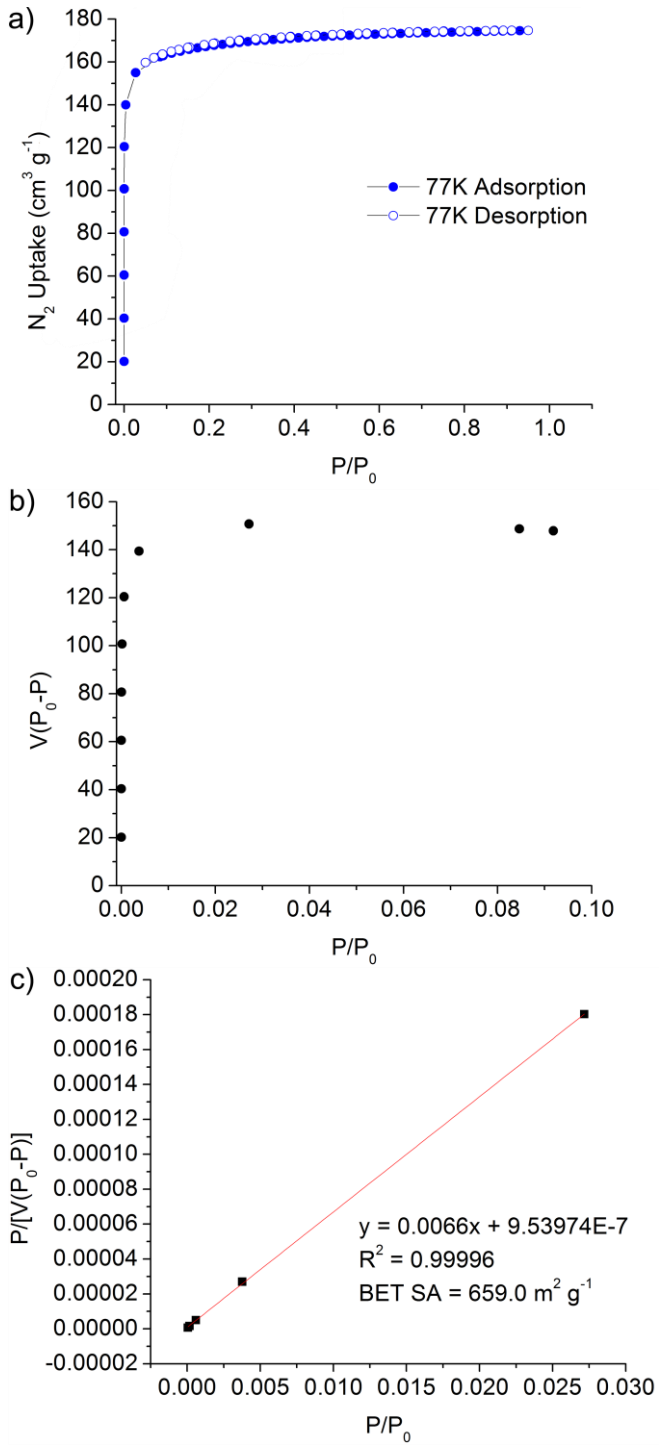

Figure 14. a) The N_2 isotherm of PCN-91 at 77K; b) plot [$V(P_0-P)$ vs. P/P_0] for N_2 isotherms of PCN-91 at 77 K and the range below $P/P_0 = 0.027171$ satisfies the BET analysis; c) plot of the linear region on the N_2 isotherm of PCN-91 for the BET equation.

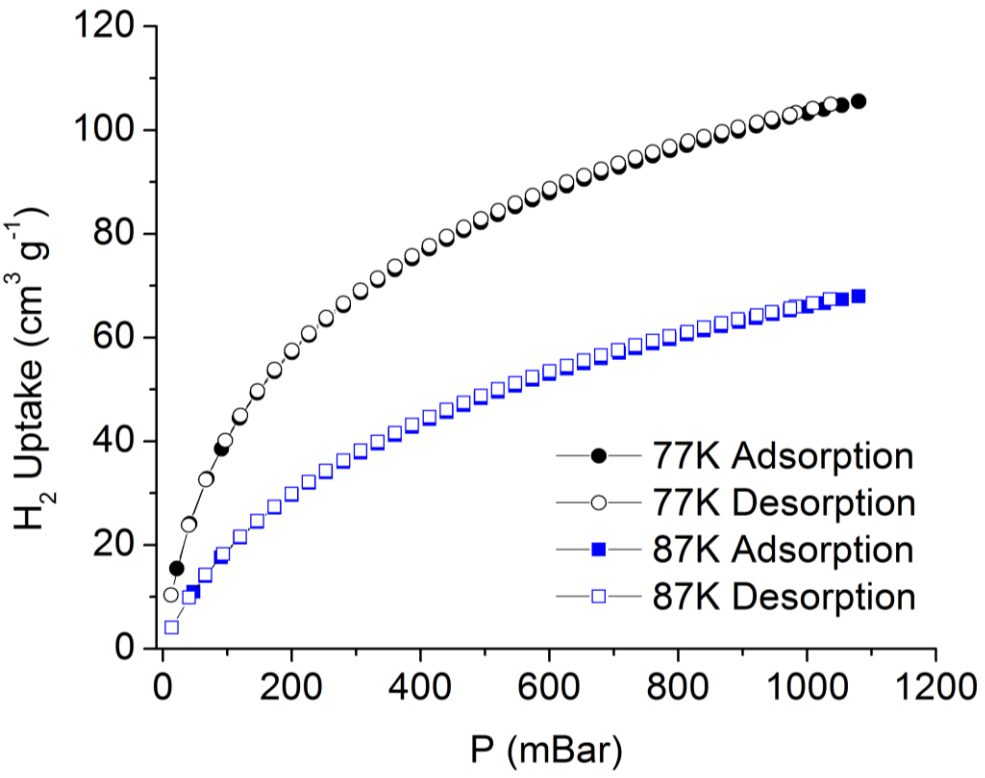

Figure 15. The H_2 isotherm of PCN-91at 77K and 87K.

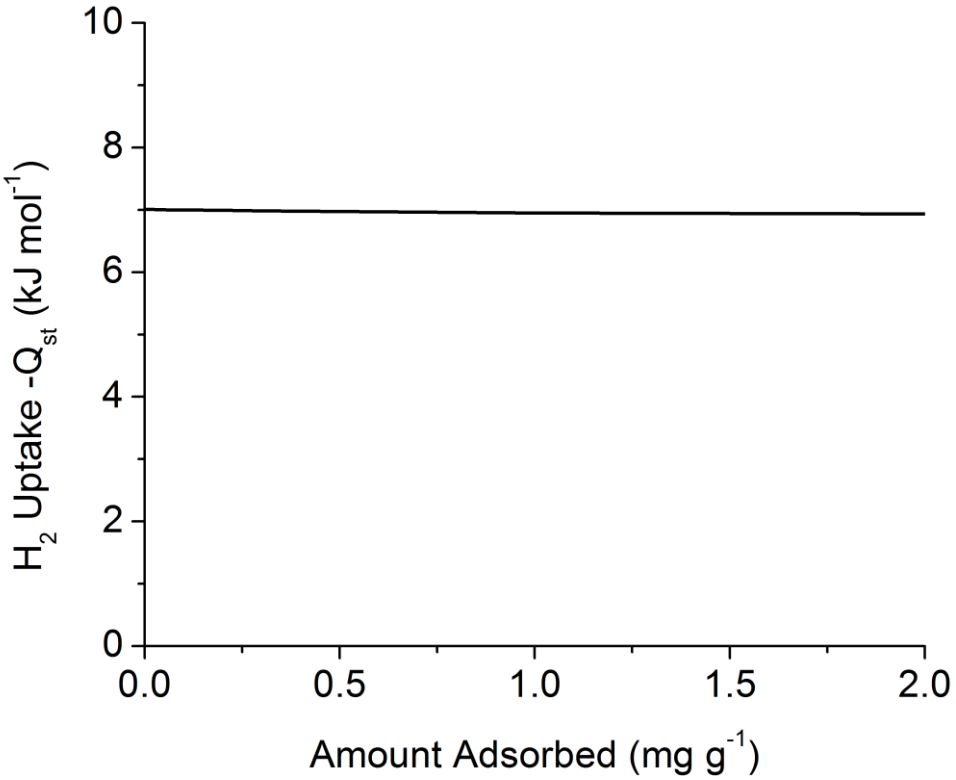

Figure 16. Coverage dependence of the isosteric heats of adsorption calculated from the isotherms for H_2.

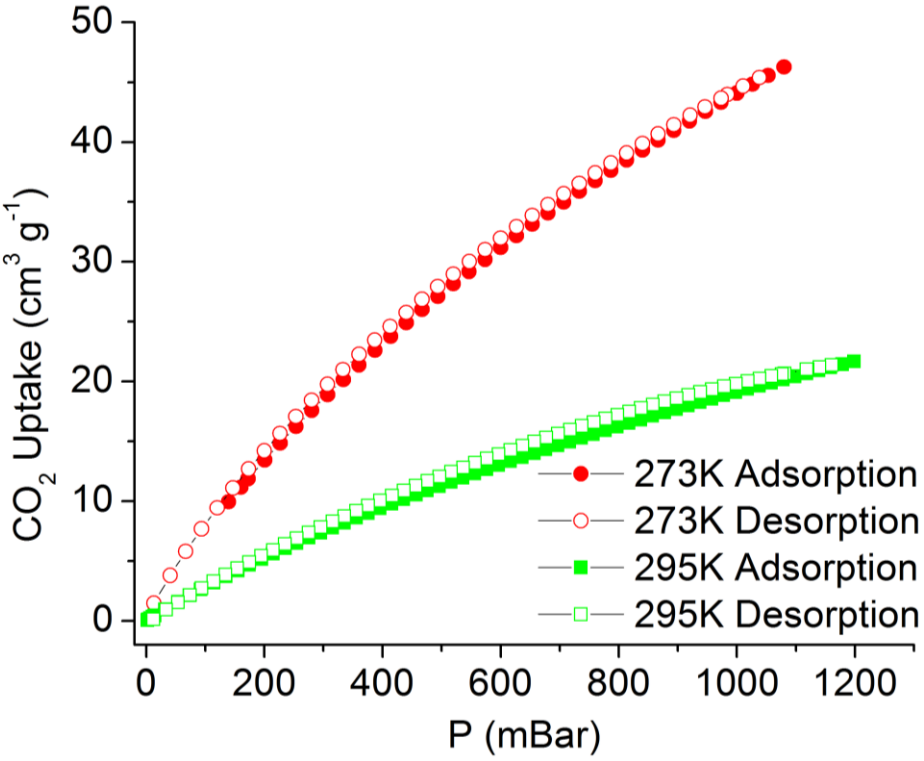

Figure 17. The CO_2 isotherm of PCN-91at 273K and 295K.

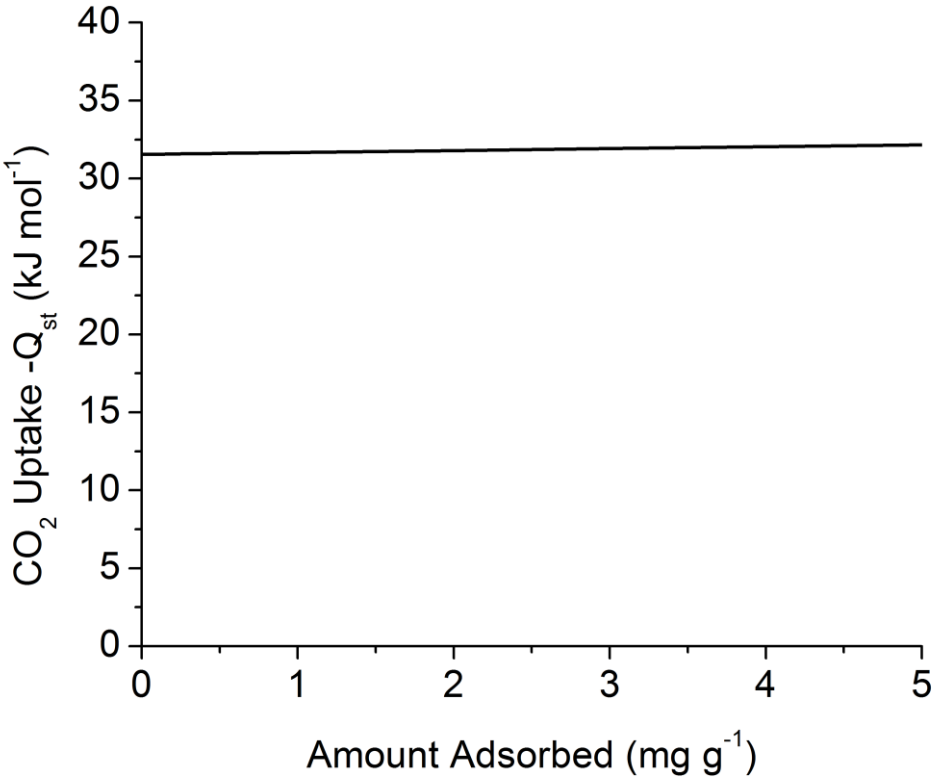

Figure 18. Coverage dependence of the isosteric heats of adsorption calculated from the isotherms for CO_2.

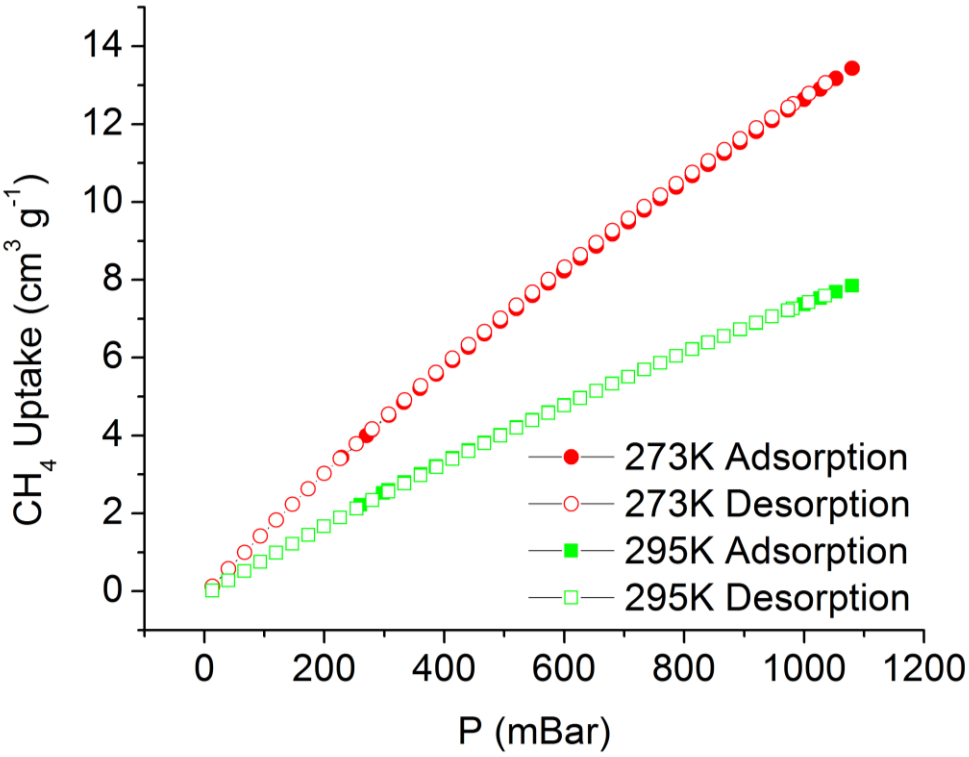

Figure 19. The CH_4 isotherm of PCN-91at 273K and 295K.

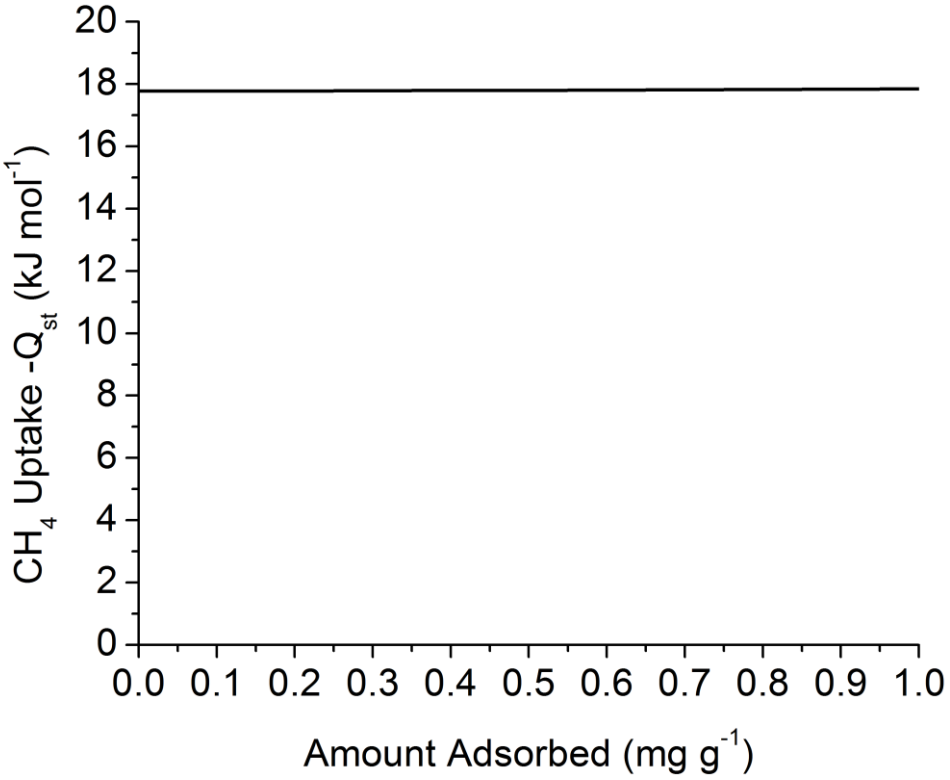

Figure 20. Coverage dependence of the isosteric heats of adsorption calculated from the isotherms for CH_4.

It is interesting to note that PCN-91 possesses the same topology with that of MOF-14 reported by Yaghi and co-workers, which was constructed from a tricarboxylate linker BTB.[139] Both BTB and Cu^{I}-dmpba are non-planar (Figure 13), which bind paddlewheel SBUs forming Pt_3O_4-nets.

To understand such a complicated assembly procedure involving two types of metal ions is not an easy task. Herein we propose a preliminary reaction mechanism, which is shown in Figure 21. The Cu(II) ions in the reaction mixture were partially reduced to Cu(I) ions in the reaction mixture. The resulted Cu(I) ions selectively coordinated to the soft nitrogen donor atoms of dmpba linkers to form Cu^{I}-dmpba linkers, which further connected the Cu_2 paddlewheel SBUs giving rise to PCN-91.

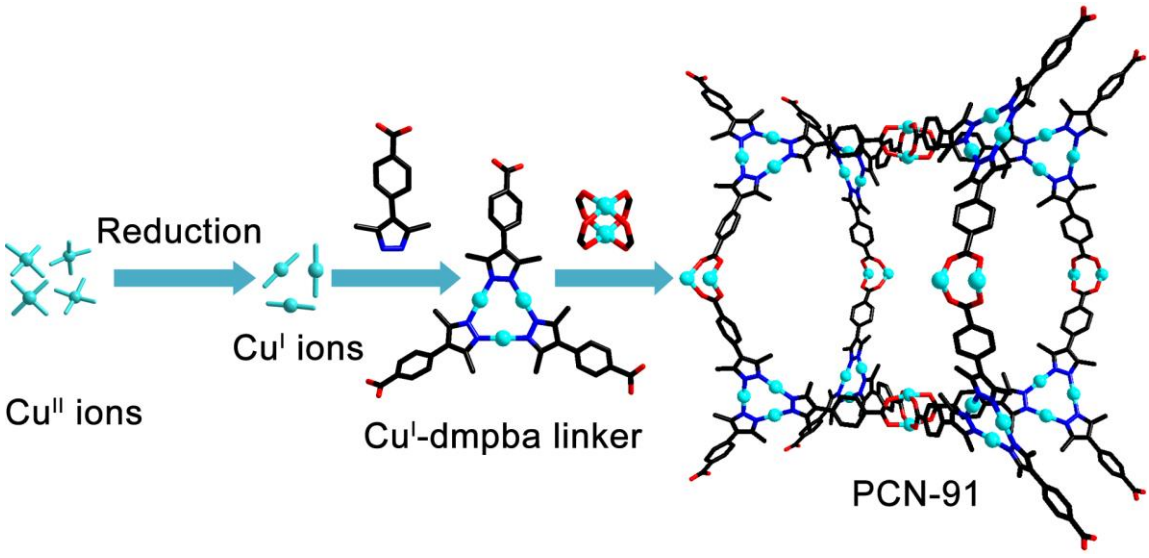

Figure 21. Schematic representation of a proposed mechanism for the assembly of PCN-91.

In order to support the proposed reaction mechanism, we decided to synthesize the reaction intermediate, the Cu^{I}-dmpba linker. A direct reaction between dmpba and a Cu(I) salt resulted in an uncharacterized precipitate. By using the ester derivative of dmpba (Hdmpbae), and $Cu(CH_3CN)_4BF_4$, a tri-nuclear Cu(I) cluster, $Cu^{I}_3(dmpbae)_3$ (compound **1**), which crystallized in triclinic space group *P*-1, has been synthesized and characterized. As shown in Figure 22, every Cu(I) ion was coordinated by two nitrogen atoms from two different dmpba linkers with an average Cu-N distance of 1.836 Å, and Cu···Cu distance of 3.201 Å, consistent with those found in PCN-91. The average dihedral angle between the pyrazolato rings and the peripheral rings is 44.8º, also comparable to that found in PCN-91. This tri-nuclear Cu(I) cluster may be applied as a starting material for MOF assembly reactions because the ester group can be hydrolyzed to a carboxylate group under basic or acidic condition. We are currently using **1** as a starting material to synthesize other MOFs.

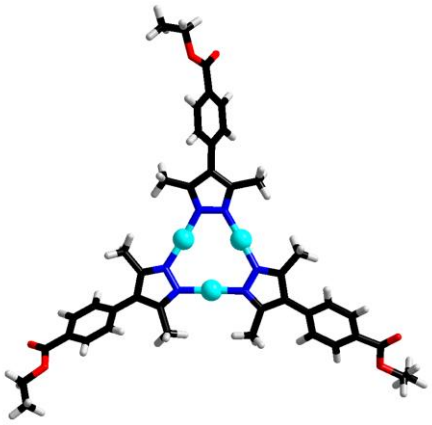

Figure 22. The structure of compound **1**.

Interestingly, it was found that the interpenetrated framework is flexible and can change its unit cell parameters reversibly under different temperatures. The length of *c* axis of the unit cell can vary from 26.35 Å to 27.52 Å while those of *a* and *b* axes remain almost unchanged (Table 2). Powder X-ray diffraction (PXRD) patterns were also simulated based on the crystal structures (Figure 23). The [2 2 2] diffraction peak was chosen as the basis for comparison because of its sensitivity toward unit cell change and the absence of interference. This peak lies at 9.05° at 95K and shifts to 8.51° at 295K. This low temperature non-rigidity is quite different from the frequently reported breathing effect of MOFs, and it is also observed for other Cu^{I}-pyrazolato complexes.[142-144] Recently, Li and coworkers suggested that this flexibility comes from the interactions between the two Cu^{I}-pyrazolato rings.[7, 145, 146] However, this cannot explain why only the *c* axis changes with the temperature variation. In our case, the translation of one of the

two interpenetrated frameworks in PCN-91 relative to the other along the crystallographic *c* axis is most likely responsible for this peculiar non-rigidity effect.

Table 2. Unit cell dimensions of PCN-91 under different temperatures.

T, K	a=b, Å	c, Å
110	39.88(11)	26.35
123	39.86(10)	26.37
173	39.92(8)	26.67
223	40.01(6)	27.39
220	39.80(5)	27.52
200	39.88(7)	27.16
180	39.73(4)	26.65
160	39.88(5)	26.49
140	39.83(5)	26.36
120	39.81(5)	26.29
110	39.65(6)	26.14

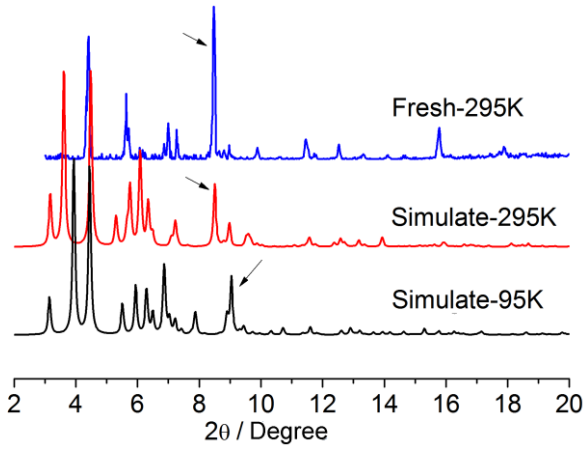

Figure 23. PXRD patterns of PCN-91, the arrows indicate the diffraction peak from the [2 2 2] lattice plane.

2.4 Conclusions

In conclusion, we have synthesized a porous MOF PCN-91 containing metal ions of two different oxidation states by using a simple bi-polar organic linker dmpba through the hard-soft-selective-coordination strategy. The metal-coordination-extended linker, Cu^{I}-dmpba, consists of three dmpba linkers and three Cu(I) ions, was generated *in situ* during the reaction. PCN-91 possessing Pt_3O_4-net topology is non-rigid, which most likely arises from the relative translation of the two interpenetrated frameworks along the crystallographic *c* axis. Although the surface area of PCN-91 is moderate, we have demonstrated a useful strategy for the construction of porous MOFs containing two types of metal ions by using a hard-soft-selective-coordination synthetic strategy. Using a series of bi-polar linkers to synthesize MOFs with different metal ions is currently underway in our laboratory.

3. A ROUTE TO METAL-ORGANIC FRAMEWORKS THROUGH FRAMEWORK-TEMPLATING*

3.1 Introduction

MOFs are composed of organic linkers and metal or metal-containing structural units, often called secondary building units (SBUs). To construct stable and highly porous MOFs for applications, especially for gas storage, using dentritic linker could be a direct and effective method.[53, 54, 59, 125, 147, 148] Thus the acid of an octatopic carboxylate linker, 4',4''',4'''''',4''''''''-(ethene-1,1,2,2-tetrayl)tetrakis(([1,1'-biphenyl]-3,5-dicarboxylic acid)) has been designed and synthesized (H_8ETTB, Figure 24 top). We are particularly interested in Cu_2 paddlewheel motif as a SBU because it is superior to Zn_2 paddlewheel motif in stability.[149] Moreover, after removal of the terminally coordinated solvent molecules, the unsaturated Cu centres have been demonstrated to enhance gas adsorption capacity due to their reported interaction with gas molecules.[150-154]

* Reprinted with permission from Wei, Z.; Lu, W.; Jiang, H.-L.; Zhou, H.-C., A Route to Metal–Organic Frameworks through Framework Templating. *Inorganic Chemistry* **2013,** *52* (3), 1164-1166. Copyright 2013 American Chemical Society.

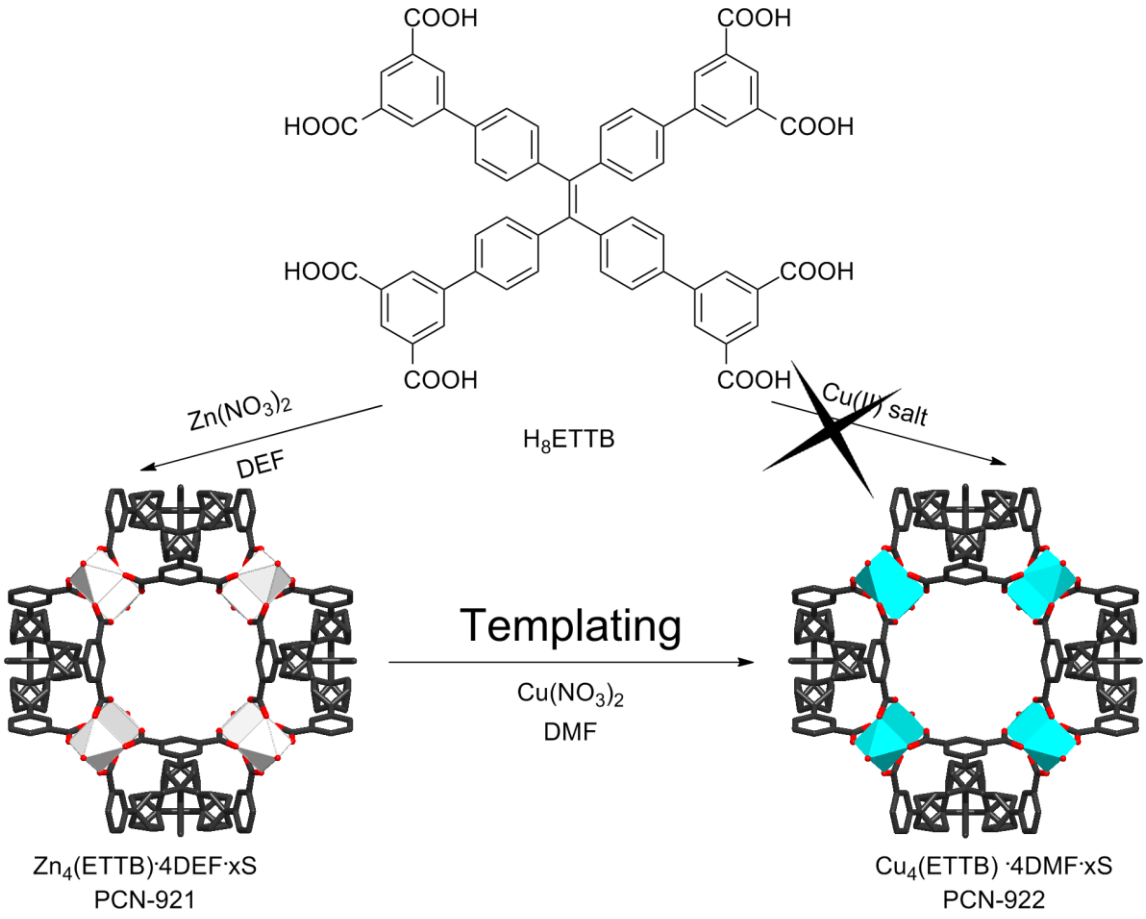

Figure 24. Schematic representation of synthesis of PCN-922 using PCN-921 as a template.

However, sometimes it is nontrivial to obtain single crystals of Cu-based MOFs, especially with extended linkers, for structure determination.[53, 125, 147] Direct synthesis of Cu-based MOF from solvothermal reactions between Cu(II) salt and H_8ETTB only yielded powders under various reaction conditions including different solvents, reaction temperatures, metal salts and pH values. Contrast to the labile Zn—O, the more inert Cu—O coordination bond may hamper defect-repair during crystal growth. On the other

hand, thanks to the d^{10} configuration of the Zn(II) ion, the labile Zn—O coordination bond may facilitate linker exchange and defect-repair during crystal growth, assisting the access of single crystals for X-ray diffraction (XRD) study and structure determination.[155, 156] Meanwhile, both the Zn_2 and Cu_2 paddlewheel SBUs, which possess very similar coordination environments and geometric parameters, are quite common in MOFs.[11, 125, 157] It has been showed that Zn_2 paddlewheel in MOF can be changed into Cu_2 paddlewheel.[158-164] Preparing metal-organic polyhedra (MOPs) by linker-substitution strategy has been reported by our group.[165] With these considerations in mind, we set out to produce the Cu-based MOF using a Zn-based MOF as a template to prearrange the linkers through a simple metal metathesis reaction.

3.2 Experimental Section

General information. Commercially available reagents were used as received without further purification. Elemental analyses (C, H, N) were obtained on a Perkin-Elmer 240 elemental analyzer. Nuclear magnetic resonance (NMR) data were collected on a Mercury 300 MHz spectrometer. Thermal gravimetric analyses (TGA) were performed under N_2 on a SHIMADZU TGA-50 TGA, with a heating rate of 5 °C min^{-1}. Gas adsorption-desorption isotherms were measured using a Micromeritics ASAP2020 system with ultra high purity (UHP) gases. X-ray photoelectron spectra (XPS) were acquired wiASth Axis Ultra DlD (Kratos) equipped with Al monochromatic X-rays operating at 12 kV and 10 mA.

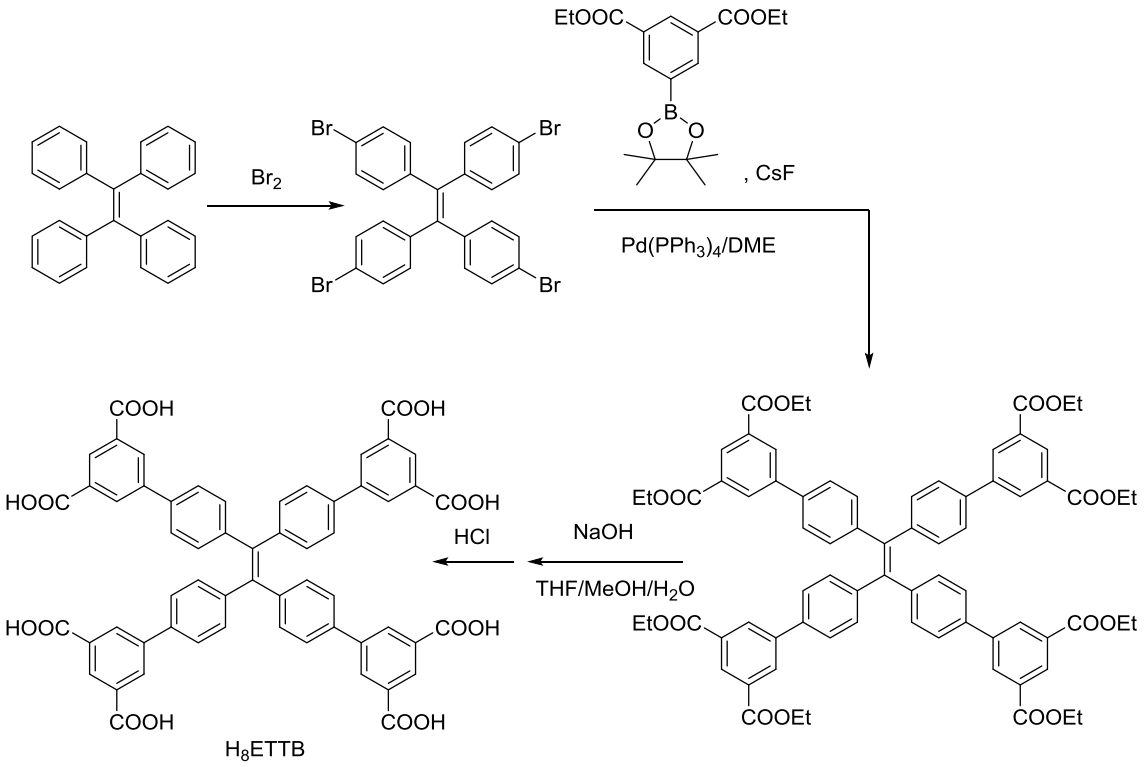

Figure 25. Schematic representation of synthesis of H_8ETTB.

Synthesis of Tetrakis(4-bromophenyl)ethene. Powdered tetraphenylethene (4.00 g, 12.0 mmol) was reacted with bromine (7.50 mL, 0.15 mol) vapor under room temperature for 4 days. The resulting solid was recrystallized in methanol and dichloromethane to yield white product (5.4 g, 8.4 mmol, 70% yield). ^{1}H NMR (300 MHz, $CDCl_3$): δ 6.85 (d, 8H), 7.28 (d, 8H).

Synthesis of octaethyl 4',4''',4'''',4''''''-(ethene-1,1,2,2-tetrayl)tetrakis([1,1'-biphenyl]-3,5-dicarboxylate). Tetrakis(4-bromophenyl)ethene[166] (1.0 g, 0.0015 mol), diethyl 5-(4,4,5,5-tetramethyl -1,3,2- dioxaborolan-2-yl)-1,3-benzene-dicarboxylate[167] (2.8 g, 0.0080 mol), cesium fluoride (3.0 g, 0.020 mol) and

tetrakis(triphenylphosphine)palladium (0.2g, 0.0002 mol) were added to a 250-mL three necked flask charged with stir bar. Then 150 mL degassed dimethoxyethane solvent was transferred to the system and the solution was refluxed for 48 hours. After the reaction mixture was cooled to room temperature, the solvent was evaporated, and the solid was dissolved in dichloromethane and washed with water. The organic part was dried with magnesium sulfate. After remove the dichloromethane, the solid was recrystalized from acetone to get light yellow product. (1.46 g, 0.0012 mol, 80% yield based on tetrakis(4-bromophenyl)ethene). ^{1}H NMR (300 MHz, $CDCl_3$): δ 1.43 (t, 24H), 4.45 (q, 16H), 7.23 (d, 8H), 7.52 (d, 8H), 8.44 (d, 8H), 8.61 (t, 4H). Elemental analysis - Calcd. (%) for Compound 1, $C_{74}H_{68}O_{16}$: C, 73.25; H, 5.65%. Found: C, 72.50; H, 5.56%. Figure 26 shows the ^{13}C NMR and Figure 27 shows the mass spectrum.

Synthesis of 4',4''',4'''''',4''''''''-(ethene-1,1,2,2-tetrayl)tetrakis(([1,1'-biphenyl]-3,5 -dicarboxylic acid)) (H_8ETTB). Octaethyl 4',4''',4'''',4''''''-(ethene-1,1,2,2-tetrayl)tetrakis([1,1'-biphenyl]-3,5-dicarboxylate) (1.46 g, 0.0012 mol) and sodium hydroxide (1.7 g, 0.0425 mol) were added into the mixture of THF, methanol and water (v/v/v=1:1:1). The solution was refluxed overnight. After removed the organic solvent, the aqueous phase was acidified with 6M HCl to yield yellow precipitate of H_8ETTB, which was filtered, washed with water, and dried under vacuum. Yield: 1.0 g, 0.0018 mol, 95%. ^{1}H NMR (300 MHz, DMSO-d^6): *δ*, 7.24 (d, 8H), 7.64 (m, 8H), 8.33 (d, 8H), 8.41 (s, 4H). Elemental analysis - Calcd. (%) for H_8ETTB, $C_{58}H_{36}O_{16}$: C, 70.44; H, 3.67%. Found: C, 69.02; H, 3.73%. Figure 28 shows the ^{13}C NMR and Figure 29 shows the mass spectrum.

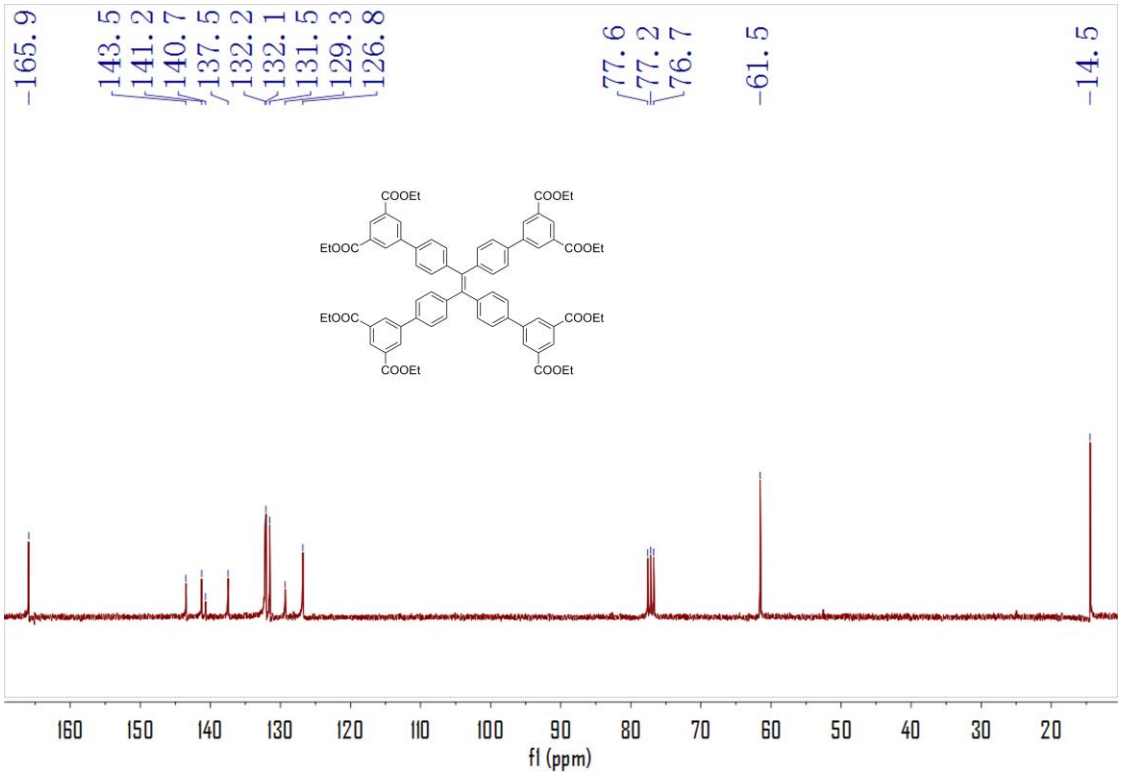

Figure 26. ^{13}C NMR (300 MHz, $CDCl_3$) of octaethyl 4',4''',4'''',4'''''-(ethene-1,1,2,2-tetrayl)tetrakis([1,1'-biphenyl]-3,5-dicarboxylate): δ 14.5, 61.5, 126.8, 129.3, 131.5, 132.1, 132.2, 137.5, 140.7, 141.2, 143.5, 165.9.

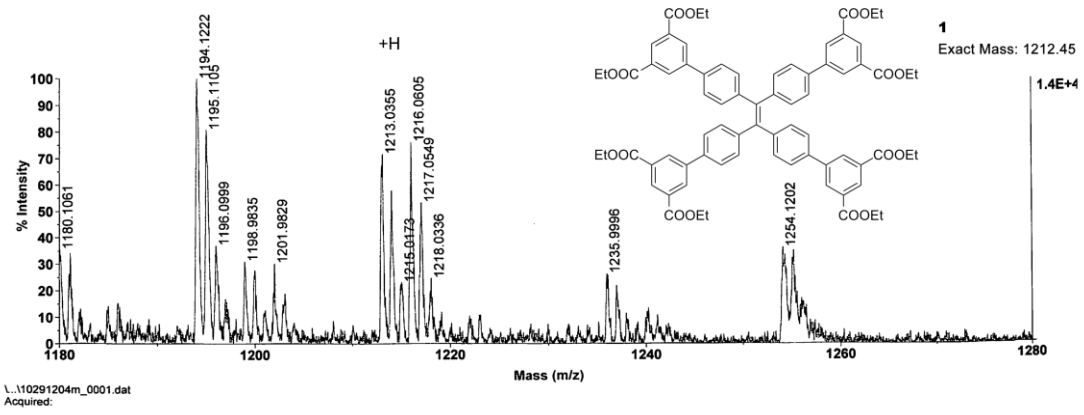

Figure 27. Mass Spectrum of octaethyl 4',4''',4'''',4'''''-(ethene-1,1,2,2-tetrayl)tetrakis([1,1'-biphenyl]-3,5-dicarboxylate).

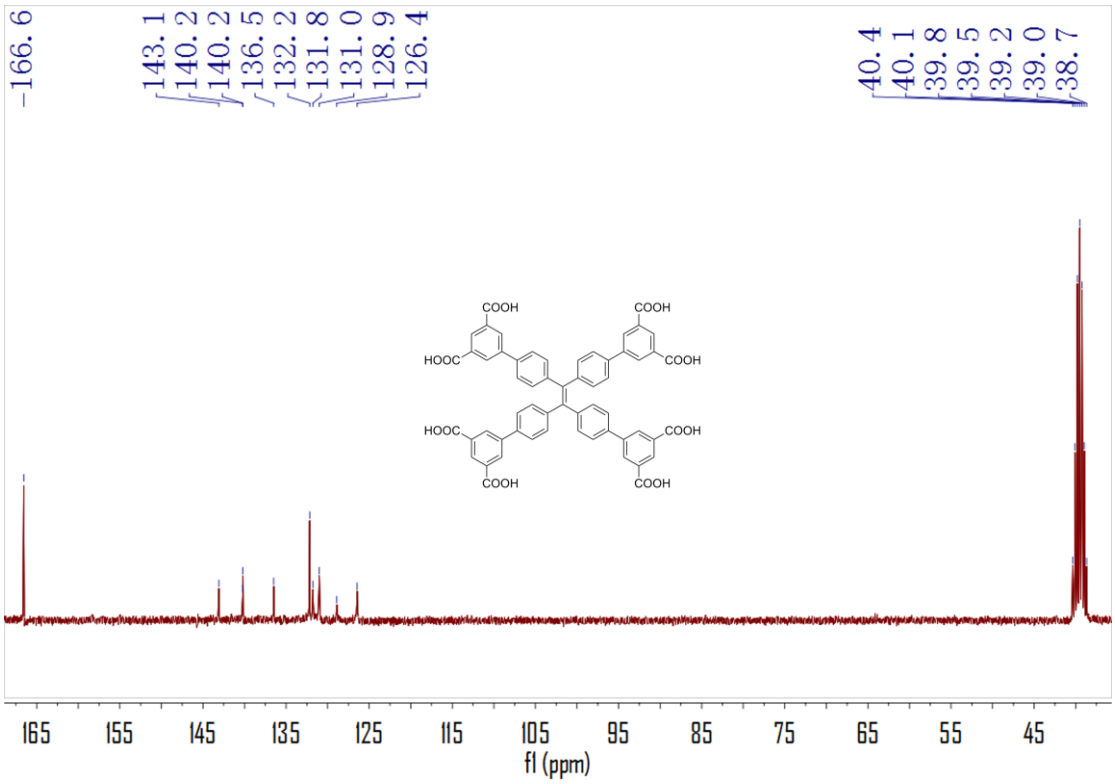

Figure 28. ^{13}C NMR (300 MHz, $CDCl_3$) of H_8ETTB: δ 126.4, 128.9, 131.0, 131.8, 132.2, 136.5, 140.2, 140.2, 143.1.

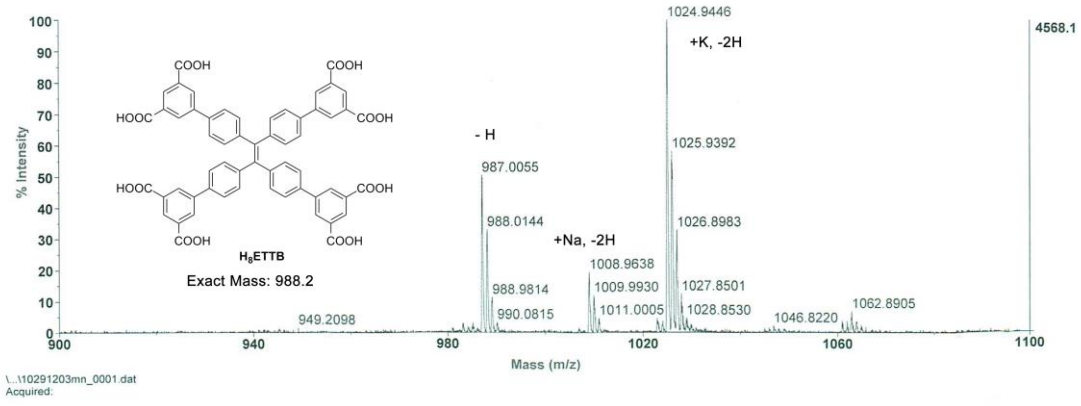

Figure 29. Mass Spectrum of H_8ETTB.

Synthesis of PCN-921. $Zn(NO_3)_2 \cdot 6H_2O$ (150 mg) and H_8ETTB (50 mg) were dissolved in 16 mL of N,N-diethylformamide in a 20 mL Pyrex vial, to which 10 drops of HBF_4 were added. The mixture was heated in 75 ºC oven for 96 hours to yield 50 mg of colourless crystals. Anal. Calcd. (%) for PCN-921, $C_{78}H_{72}Zn_4N_4O_{20}$: C, 56.88; H, 4.41; N, 3.40%. Found: C, 52.14; H, 4.82; N, 5.85%.

Synthesis of PCN-922. PCN-921 (50 mg) and $Cu(NO_3)_2 \cdot 2.5H_2O$ (150 mg) were added in 16 mL of *N,N*-dimthylformamide in a 20 mL Pyrex vial. The mixture was keep under room temperature for 4 days to yield 50 mg of green crystals. Anal. Calcd. (%) for PCN-922, $C_{70}H_{56}Cu_4N_4O_{20}$: C, 55.04; H,3.70; N, 3.67%. Found: C, 49.32; H, 5.31; N, 7.31%. Elemental Analysis for activated PCN-922, $C_{58}H_{28}Cu_4O_{16}$: C, 56.41; H, 2.29 %. Found: C, 55.76; H, 2.12 %.

Failed synthesis conditions for PCN-922 during direct synthesis. All reactions are performed in a 2 ml vial with 1.6 mL solvent. Typical conditions are listed, some more minor adjustment of conditions were performed.

Acid: Trifloroacetic acid

DMF: *N,N*-dimthylformamide DEF: *N,N*-diethylformamide

DMA: Dimethylacetamide DMSO: Dimethyl sulfoxide

NMP: *N*-methyl-2-pyrrolidone

NO3: $Cu(NO_3)_2 \cdot 2.5H_2O$ Br: $CuBr_2$

B: Benzoic acid D: Terephthalic acid

T: Benzene-1,3,5-tricarboxylic acid

Table 3. Failed synthesis conditions for PCN-922 during direct synthesis.

Linker Amount (mg)	Copper Salt and Amount (mg)	Solvent	Acid, (drop)	Water, (drop)	Temperature, (℃)	Note
5	NO3, 15	DMF	0		75	
5	NO3, 15	DMF	1		75	
5	NO3, 15	DMF	2		75	
5	NO3, 15	DMF	1		85	
5	NO3, 15	DMF	2		85	
5	NO3, 15	DMA	1		75	
5	NO3, 15	DMA	2		75	
5	NO3, 15	DMA	1		85	
5	NO3, 15	DMA	2		85	
5	NO3, 15	DMA: DMSO =1:1	1		85	
5	NO3, 15	DMA: DMSO =1:1	2		85	
5	Br, 15	DMF	0	3	75	
5	NO3, 15	DMF	0	1	100	
5	NO3, 15	DMF	0	2	100	
5	NO3, 15	DEF	7		75	
5	NO3, 15	DEF	9		75	
5	NO3, 15	DEF	11		75	
5	NO3, 15	DEF	13		75	
5	NO3, 15	DEF	9		85	
5	NO3, 15	DEF	12		85	
5	NO3, 15	DEF	15		85	

Table 3. continued

Linker Amount (mg)	Copper Salt and Amount (mg)	Solvent	Acid, (drop)	Water, (drop)	Temperature, (℃)	Note
5	NO3, 15	DEF			75	EtOH 3drop
5	NO3, 15	DEF			75	Cyclohexane, 3 drop
5	NO3, 15	NMP	3		75	
5	NO3, 15	DMF	2		75	B, 30 mg
5	NO3, 15	DEF	2		75	B, 30 mg
5	NO3, 15	DMA	2		85	B, 30 mg
5	NO3, 15	DMA : DMSO= 1:1	2		85	B, 30 mg
5	NO3, 15	DMF	0		60	
5	NO3, 15	DMF	1		60	
5	NO3, 15	DMF : DMSO= 1:1	0		60	
5	NO3, 15	DMF : DMSO= 1:1	2		85	
5	NO3, 15	DMF	2		85	B, 10 mg
5	NO3, 15	DMF	5		85	B, 10 mg
5	NO3, 15	DEF	2		85	B, 10 mg
5	NO3, 15	DEF	5		85	B, 10 mg
5	NO3, 15	DMF	2		75	B, 10 mg
5	NO3, 15	DMA	2		85	B, 10 mg

Table 3. continued

Linker Amount (mg)	Copper Salt and Amount (mg)	Solvent	Acid, (drop)	Water, (drop)	Temperature, (℃)	Note
5	NO3, 15	DMF	2		75	D, 10 mg
5	NO3, 15	DMF	2		85	D, 10 mg
5	NO3, 15	DMA	2		85	D, 10 mg
5	NO3, 15	DMF	2		75	T, 10 mg
5	NO3, 15	DMA	2		85	T, 10 mg
5	NO3, 15	DMA	4		85	
5	NO3, 15	DMA	5		85	
5	NO3, 15	DMA	6		85	
5	NO3, 15	DMA	7		85	
5	NO3, 15	DMA	8		85	
5	NO3, 15	DMA	9		85	
5	NO3, 15	DMA	6		85	H_2O, 2 drop
5	NO3, 15	DMA	6		85	H_2O, 5 drop
5	NO3, 15	DMA	6		85	DMSO, 3 drop
5	NO3, 15	DMA	6		85	DMSO, 6 drop
5	NO3, 15	DMA	6		75	
5	NO3, 15	DMA	6		75	B, 10 mg
5	NO3, 15	DMA	6		85	DMSO, 10 drop
5	NO3, 15	DMA : DMSO= 1:2	6		85	

Table 3. continued

Linker Amount (mg)	Copper Salt and Amount (mg)	Solvent	Acid, (drop)	Water, (drop)	Temperature, (℃)	Note
5	NO3, 15	DMSO	6		60	DMA, 6 drop
5	NO3, 15	DMA	6		75	
5	NO3, 15	DMA	7		75	
5	NO3, 15	DMA	8		75	

Single-crystal X-ray crystallography. Single-crystal crystallographic data were collected on a Bruker single-crystal APEXII CCD Diffractometer with MoK_α (λ = 0.71073 Å) at 110K. All structures were solved by direct method and refined by full-matrix least-squares on F^2 using *SHELXTL*.[168] Non-hydrogen atoms were refined with anisotropic displacement parameters during the final cycles. Organic hydrogen atoms were placed in calculated positions with isotropic displacement parameters set to 1.2 × U_{eq} of the attached atom. The solvent molecules are highly disordered, and attempts to locate and refine the solvent peaks were unsuccessful. Contributions to scattering due to these solvent molecules were removed using the *SQUEEZE* routine of *PLATON*;[137] structures were then refined again using the data generated. Crystal data are summarized in Table 4.

Table 4. Crystal Data for PCN-921 and PCN-922.

MOF	PCN-921	PCN-921
Formula	$Zn_4C_{58}H_{28}O_{20}$	$Cu_4C_{58}H_{28}O_{20}$
Formula weight	1306.28	1298.96
Color	Colorless	Blue
Crystal size (mm^3)	0.07 x 0.07 x 0.03	0.05 x 0.05 x 0.03
Crystal system	Tetragonal	Tetragonal
Space group	*I*4/*mmm*	*I*4/*mmm*
a/b/c (Å)	19.38/19.38/35.04	18.583/18.583/35.68
$\alpha/\beta/\gamma$ (°)	90/90/90	90/90/90
V, $Å^3$	13160	12320
Z	4	4
d_{calc} (g cm^{-3})	0.659	0.700
μ (mm^{-1})	0.753	0.716
F(000)	2624	2608
T (K)	110	110
θ range for data collection (°)	1.89 to 29.30	1.14 to 24.69
Reflections collected	68255	57162
Independent reflections	4896	2964
R(int)	0.1846	0.2204
Observed data [I>2σ(I)]	1858	1322
Completeness to θ_{max}	97.4%	99.4%
GOF on F^2	0.860	1.053
Data/restraints/parameters	4896/0/122	2964/17/96
*R*1, *wR*2 [I > 2σ(I)]	0.0567, 0.1133	0.0902, 0.2130
*R*1, *wR*2 (all data)	0.2081, 0.1480	0.2133, 0.2621

Powder X-ray diffraction (PXRD) patterns. PXRD patters were obtained on a BRUKER D8-Focus Bragg-Bretano X-ray Powder Diffractometer equipped with a Cu sealed tube (λ = 1.54178) at a scan rate of 0.2 s deg^{-1}. The simulated PXRD spectra were obtained by the diffraction-crystal module of the *Mercury* program based on the single-crystal data. The program is available free of charge via internet at *http:/www.iucr.org*. The activated PCN-922 is sensitive toward moisture. So a special PXRD plate with cover was used when running the PXRD patterns (Figure 30).

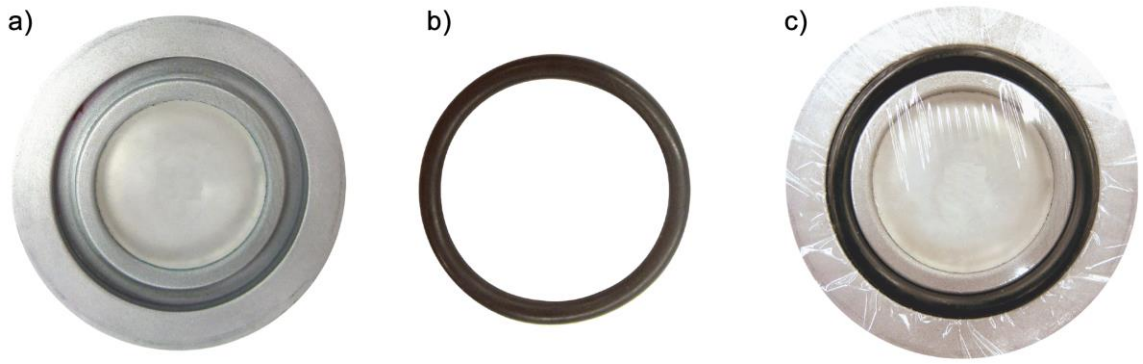

Figure 30. a) Special PXRD sample plate; b) the o-ring; c) sample plate covered with Kapton film held by the o-ring.

Gas adsorption measurements. The low-pressure gas sorption isotherm measurements were performed on an ASAP 2020 surface area and pore size analyzer using ultra high pure (UHP) grade gases. An as-isolated sample of PCN-921/PCN-922 was immersed in methanol for 24 hours, and the extract was decanted. Fresh methanol was subsequently added, and the crystals were allowed to stay for an additional 24 hours

to remove the nonvolatile solvates (DMF and water). The sample was collected by decanting and treated with dichloromethane (CH_2Cl_2) similarly to remove methanol solvates. After the removal of CH_2Cl_2 by decanting, the sample was activated by drying under a dynamic vacuum at room temperature overnight. Before the measurement, the sample was dried again by using the "outgas" function of the surface area analyzer for 10 hours at 85 °C. Oil-free vacuum pumps and oil-free pressure regulators were used to prevent contamination of the samples during the degassing processes and isotherm measurements.

3.3 Results and Discussion

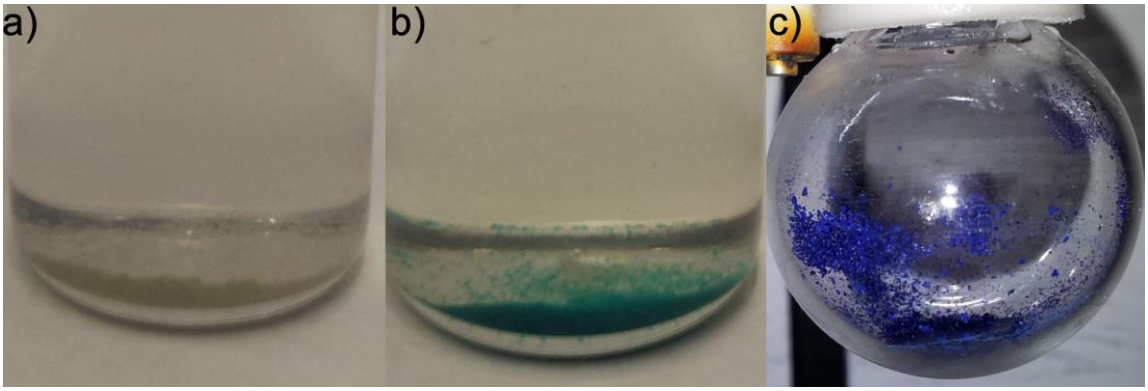

Figure 31. a) The colorless crystals of PCN-921; b) the green crystals of PCN-922; c) the deep blue crystals of activated PCN-922.

The first step is to synthesize the MOF template containing Zn_2 paddlewheel structural motif. As expected, the reaction between H_8ETTB and $Zn(NO_3)_2 \cdot 6H_2O$ in

DEF (*N*,*N*-diethylformamide) in the presence of HBF_4 produced a Zn-based MOF, Zn_4(ETTB)·4DEF·x*S* (*S* represents non-coordinated solvent molecules), named as PCN-921 (PCN stands for porous coordination network). A single-crystal XRD[168] study reveals that PCN-921 is a porous 3D framework composed of ETTB linkers and Zn_2 paddlewheel as desired. Subsequently, the colourless crystals of PCN-921 was immersed in a DMF (*N*,*N*-dimethylformamide) solution of $Cu(NO_3)_2$ at room temperature for four days (Figure 24) to ensure complete metal replacement and permanent porosity. The colorless crystals (Figure 31a) became green in color (Figure 31b) and XPS studies on a thoroughly washed and grinded MOF sample clearly indicate that no Zn was left in the framework (Figure 32 & Figure 33). The resultant Cu-based MOF, Cu_4(ETTB)·4DMF·x*S* (designated as PCN-922), was obtained as green crystals. Single-crystal XRD studies have revealed that PCN-921 and PCN-922 are isostructural with only a slight difference in cell parameters. In the following, only the structure of PCN-922 will be illustrated in detail.

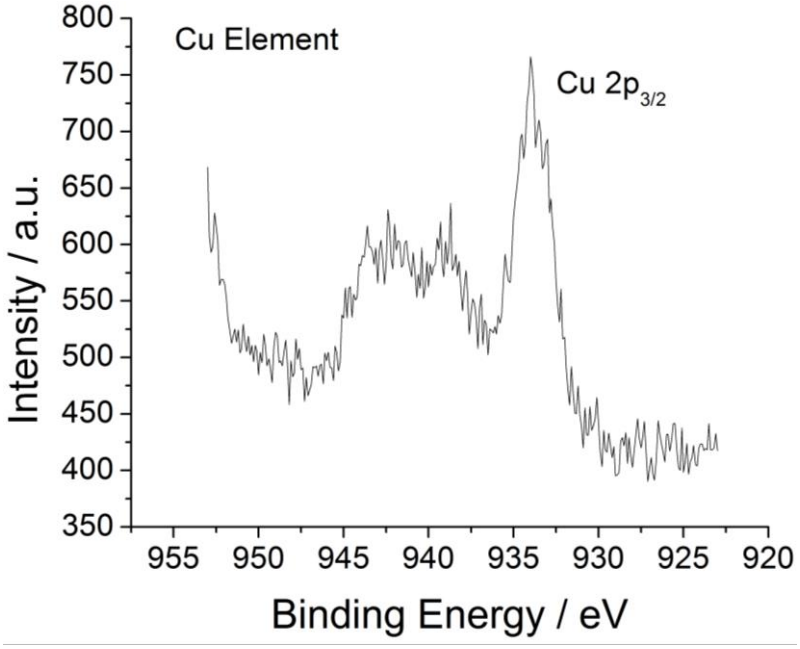

Figure 32. XPS spectra of Cu 2p.

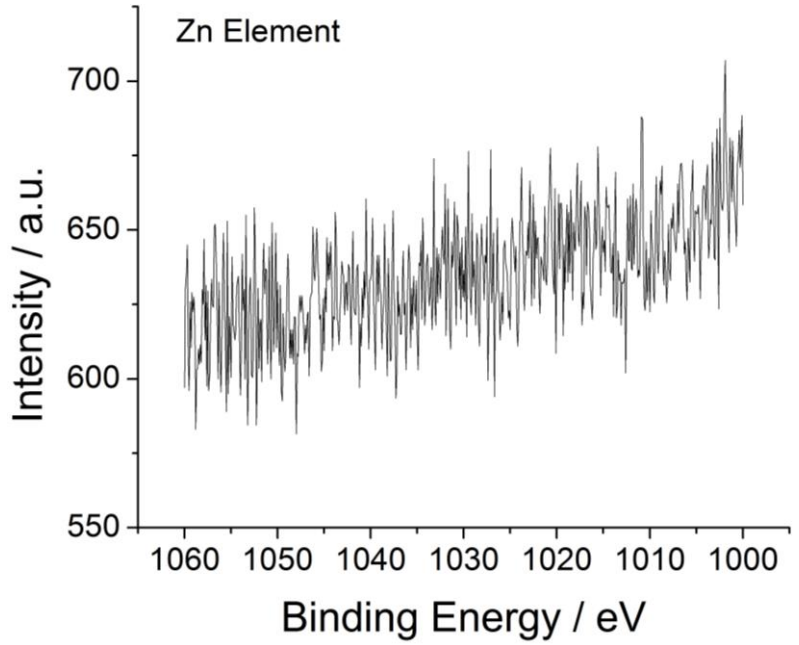

Figure 33. XPS spectra of Zn 2p. The Zn content is lower than the detect limit.

PCN-922 crystallizes in *I*4/*mmm* space group with $a = b = 18.583(16)$ and $c = 35.68(3)$ Å (Table 4). In the structure of PCN-922, the bond angle (107.96°) between the two single bonds at each end sp^2 carbon atom of the central ethene fragment highly deviate from the ideal value (120°). The six carbon atoms at the center of the linker are coplanar; the dihedral angle between the benzene ring of one isophthalic moiety and the *central* plane is 90°. Each carboxylate group of an ETTB linker connects one Cu_2 paddlewheel so that each ETTB linker, in a rectangular prismatic arrangement, connects eight Cu_2 SBUs leading to a highly porous 3D network. The framework contains two types of microporous cages with different sizes. The small one (14 Å in diameter) is composed of eight Cu_2 SBUs and eight ETTB linkers (Figure 34a), while the large one (18 Å) is formed by eight Cu_2 SBUs and twelve ETTB linkers (Figure 34b). The two types of cages alternate in 1:1 to form 1D channels of 9 Å running down the *c*-axis of the framework (Figure 34c). If the paddlewheel SBU and ETTB are viewed as 4-connected nodes and 3,4-connected nodes, respectively, the framework can be simplified as 3,4-c 2 nodal net with **tbo** topology. If ETTB is further simplified as 8-connected nodes, the framework can be seen as a 4,8-*c* 2-nodal net with **scu** topology, which is the same as other reported MOFs assembled with octatopic linkers and 4-connected SBUs (Figure 34d).[54, 59, 147, 148]

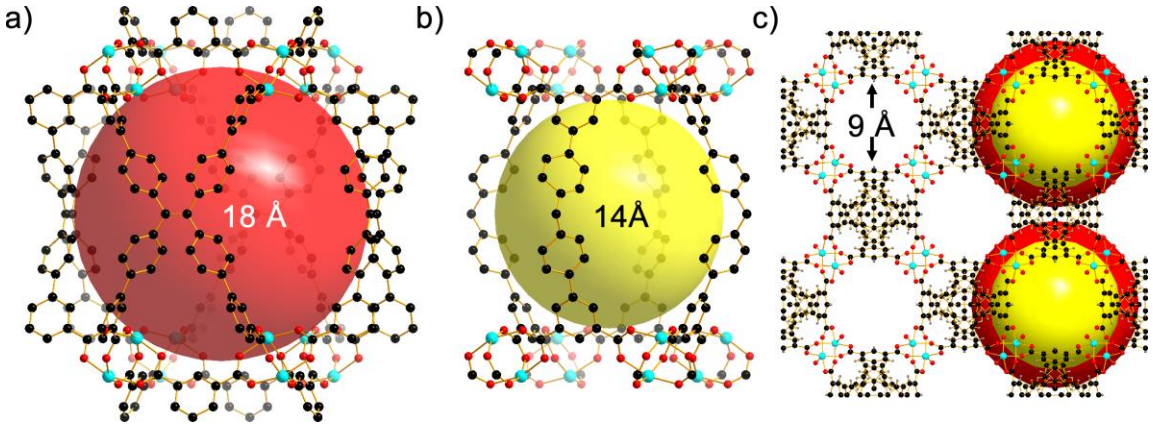

Figure 34. a) The large cage with 18 Å pores; b) the small cage with 14 Å pores; c) a view of the structure of PCN-222 along the *c*-axis. (Hydrogen atoms and disordered structural components are omitted for clarity).

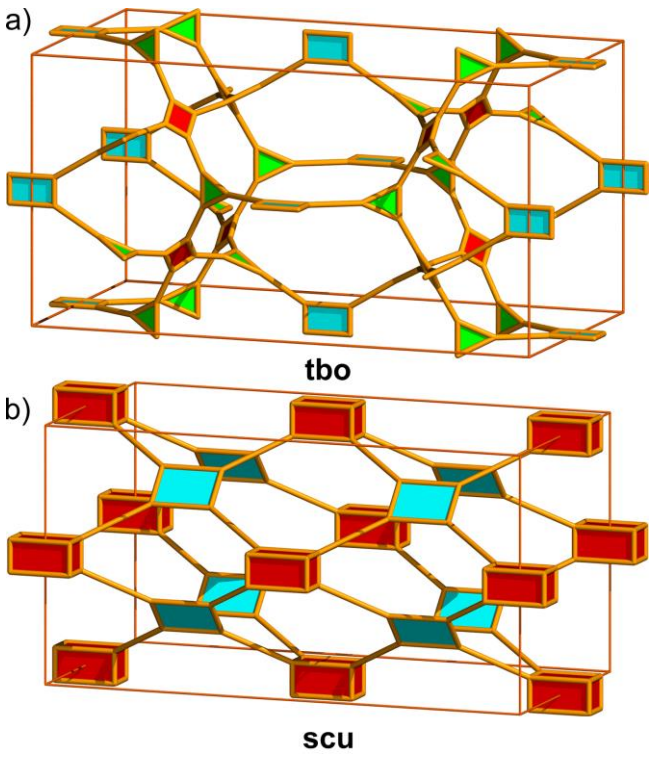

Figure 35. PCN-922 simplified as a) **tbo** and b) **squ** topology respectively.

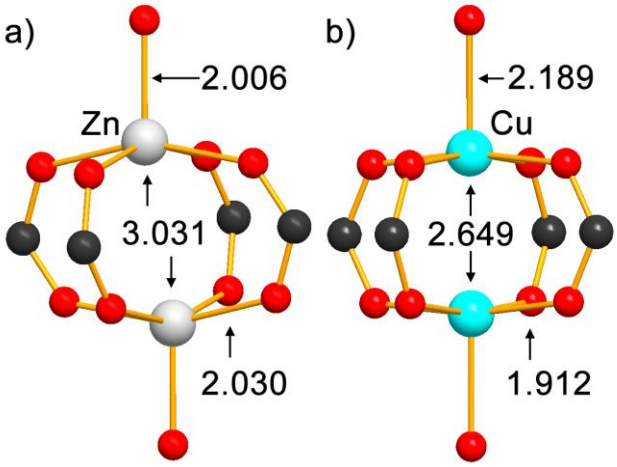

Figure 36. a) Zn_2 paddlewheel and b) Cu_2 paddlewheel SBUs in PCN-221 and PCN-222, respectively.

In the frameworks, both Zn(II) and Cu(II) ions adopt distorted square pyramidal geometry with each metal atom sitting above the square base of the pyramid (Figure 36). With simple Valence Shell Electron Pair Repulsion (VSEPR) theory, Zn(II) would prefer trigonal bipyramidal coordination geometry instead of the square pyramid. So the Zn(II) paddlewheel is actually unstable geometry. Meanwhile, after removal of the apical solvent molecule, Zn(II) ion prefers tetrahedral to square-planar ligand field.[156] Therefore, Zn_2 paddlewheel SBU which could lose coordinated solvent usually collapse upon activation. Based on the simple angular overlap model (AOM), we can estimate the preference energy in terms of e_σ (based on an ideal overlap between the d_{z2} orbital and a σ-donor ligand) and e_π (based on an ideal overlap between a d_{xz} or d_{yz} orbital and a p π-donor ligand), respectively.[156] Based on the orbital diagrams constructed from the AOM, the net stabilization energy of Cu(II) in a square pyramidal coordination environment is

$3e_\sigma$ (Figure 37), and that of a trigonal bipyramidal coordination environment is 11/4 $3e_\sigma$ (Figure 38). Thus, the Cu_2 paddlewheel with stabilization is more stable than the Zn_2 one in a square pyramidal coordination environment, shifting the metathesis equilibrium toward the Cu-based MOF. And the stabilization energy of those for square planar and tetrahedral coordination environment are $3e_\sigma$ and ($4/3\ e_\sigma + 8/9\ e_\pi$), respectively (Figure 39 & Figure 40).Furthermore, since e_σ is often much larger than $2e_\pi$, four-coordinated Cu(II) is more stable in square planar than in tetrahedral structures, which is why the Cu_2 paddlewheel can survive the activation process (Figure 41 & Figure 42).

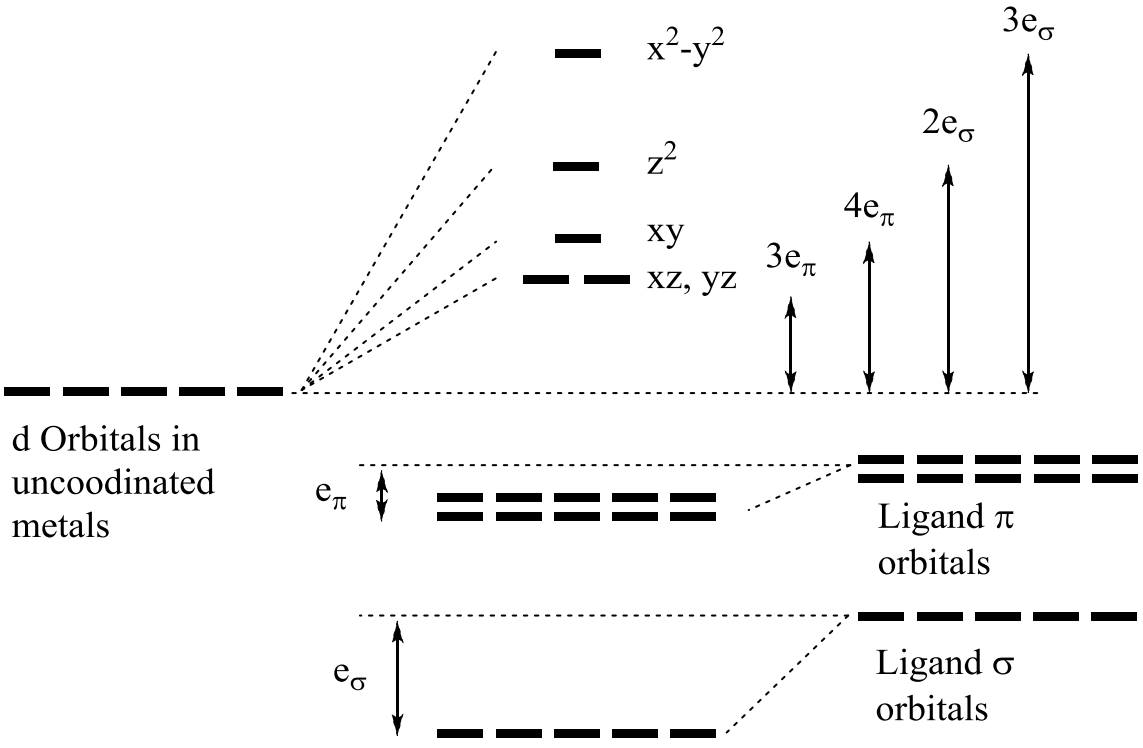

Figure 37. Energy diagram of Cu(II) in square pyramidal mode.

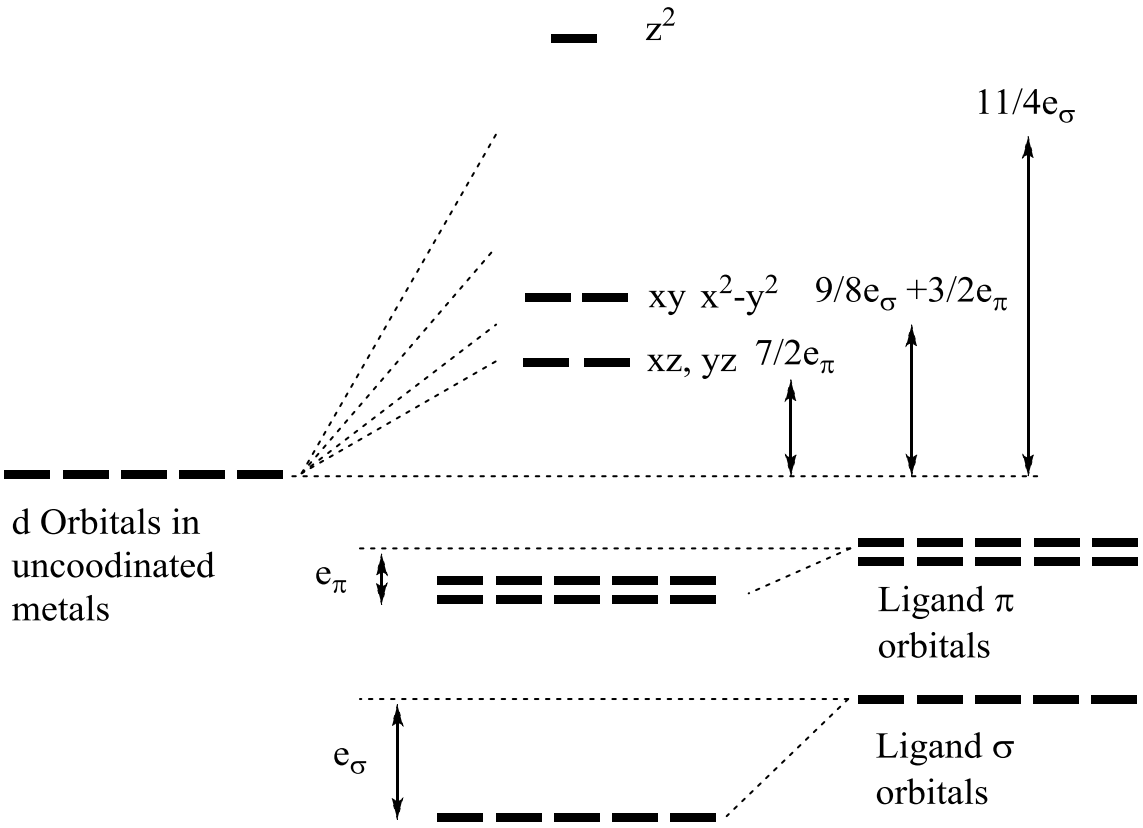

Figure 38. Energy diagram of Cu(II) in trigonal bipyramidal mode.

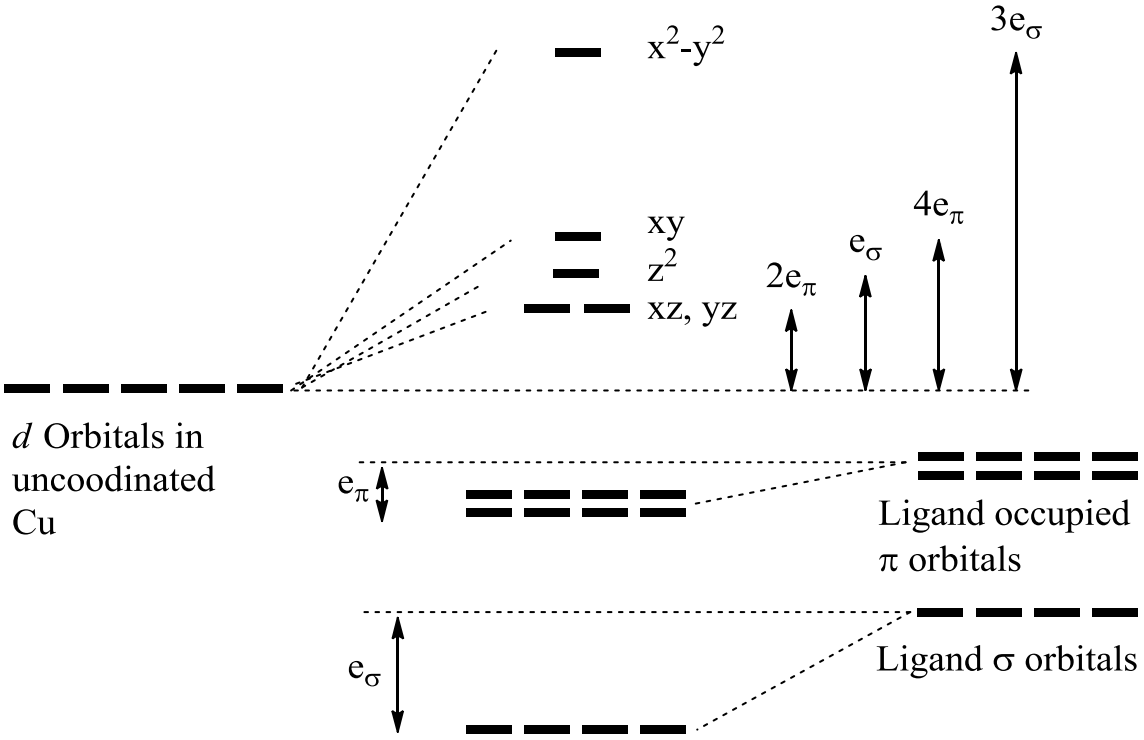

Figure 39. Energy diagram of Cu(II) in square planar mode.

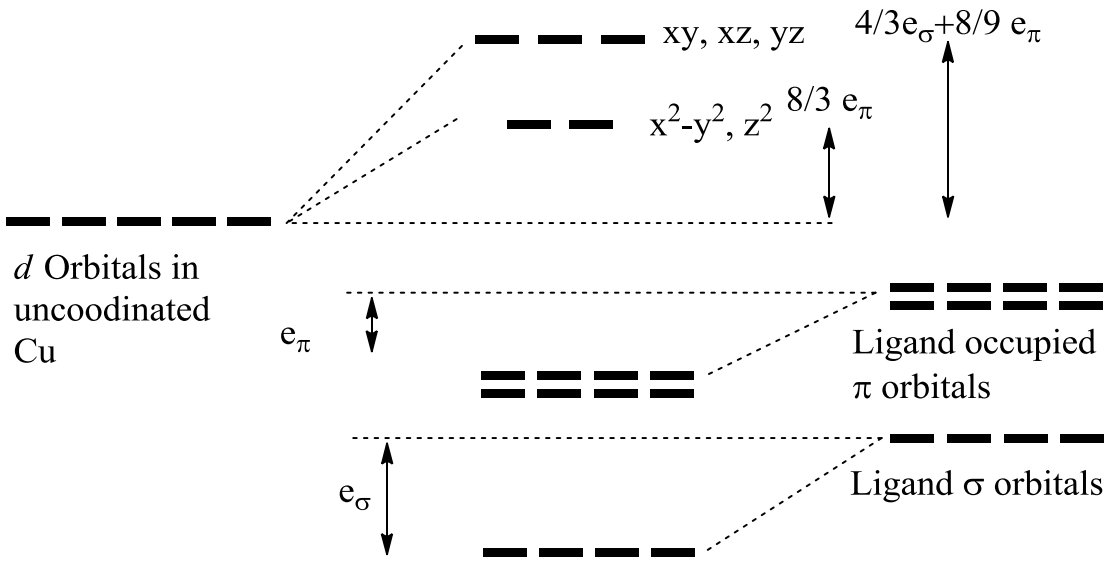

Figure 40. Energy diagram of Cu(II) in tetrahedral mode.

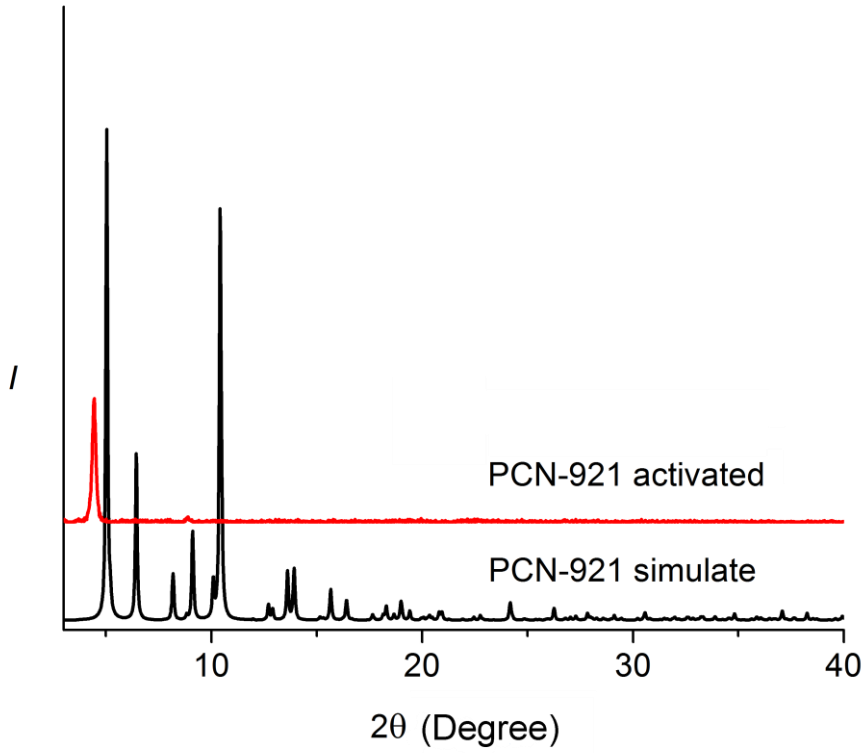

Figure 41. PXRD patterns of activated PCN-921.

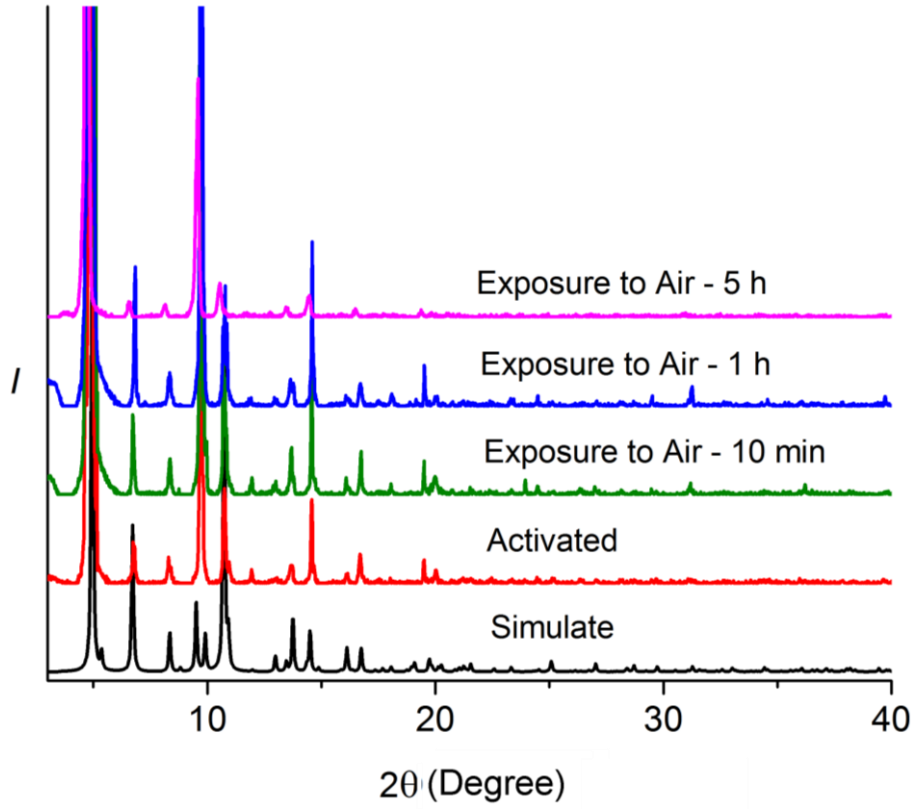

Figure 42. PXRD patterns of activated PCN-922 sample exposed to air for stability test.

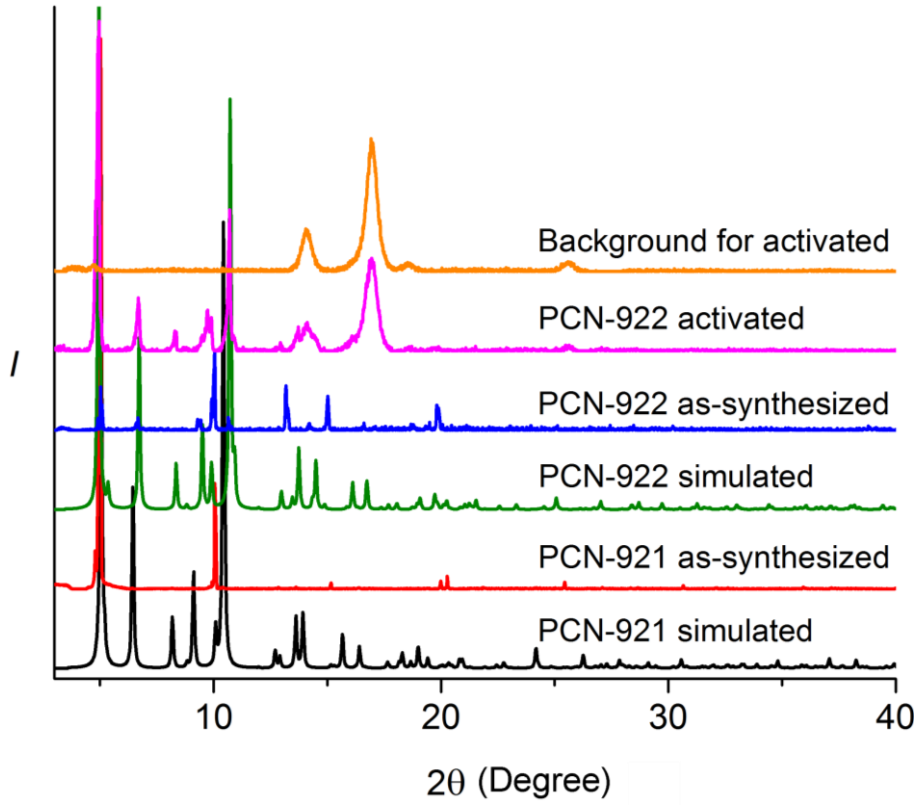

Figure 43. PXRD patterns of PCN-921 and PCN-922.

Calculations using the CALCSOLV routine in *PLATON* software were performed to evaluate the porosities of PCN-921 and PCN-922.[137] The results indicate that the solvent accessible volume of fully desolvated MOFs (1.8 Å probe radius) is 66.0% for PCN-921 and 66.2% for PCN-922, respectively. To confirm the porosities, both samples were degassed under dynamic vacuums at 85 °C for ten hours each after solvent exchange with methanol and dichloromethane. The phase purity of the MOFs was evaluated by PXRD pattern (Figure 43). After activation, the colourless PCN-921 became yellow in color, possibly a sign of crystal decomposition. Indeed, it showed no

N_2 adsorption as expected. Upon activation, the color of PCN-922 changed from green to deep blue, indicating the generation of open metal sites in Cu-based MOFs (Figure 31c).[34, 147] PCN-922 showed type-I isotherm for N_2 sorption at 77 K and 1 bar, revealing the microporous nature of the framework, consistent with the observed porosity from the crystal structure (Figure 44). Langmuir and Brunauer-Emmett-Teller (BET) surface areas are 2615 m^2g^{-1} and 2322 m^2g^{-1}, respectively.[85, 169] The total pore volume is 0.94 cm^3g^{-1}, approaching the value (0.99 cm^3g^{-1}) calculated from the crystal structure using the *PLATON* routine.

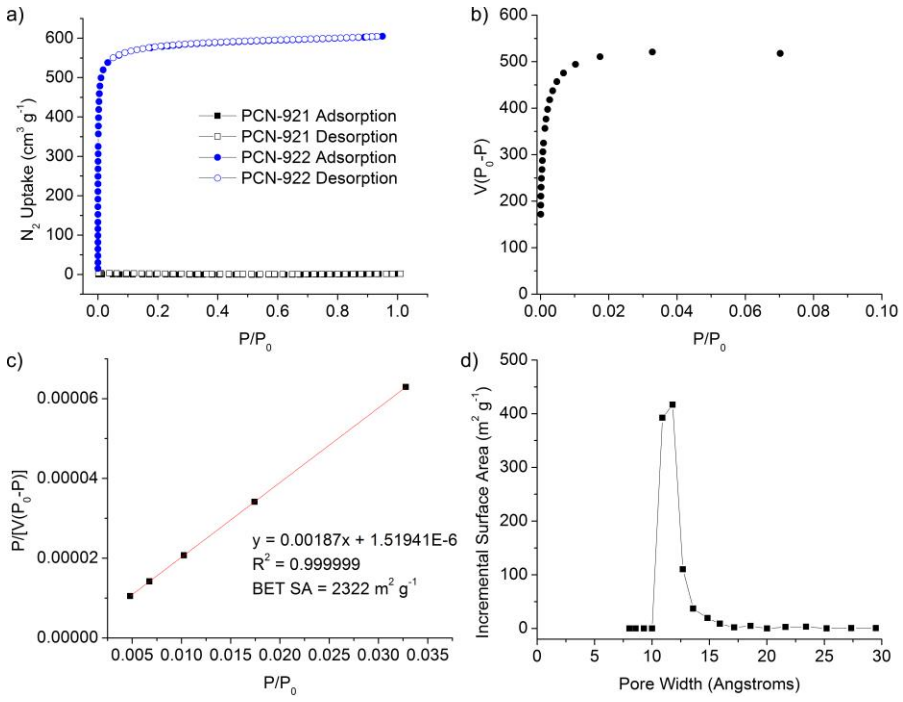

Figure 44. a) N_2 sorption isotherms for PCN-921 and PCN-922 at 77K; b) plot [$V(P_0-P)$ vs. P/P_0] for N_2 isotherms of PCN-922 at 77 K and the range below $P/P_0 = 0.032779$ satisfies the BET analysis; c) plot of the linear region on the N_2 isotherm of PCN-922 for the BET equation. d) DFT pore size distribution for PCN-922.

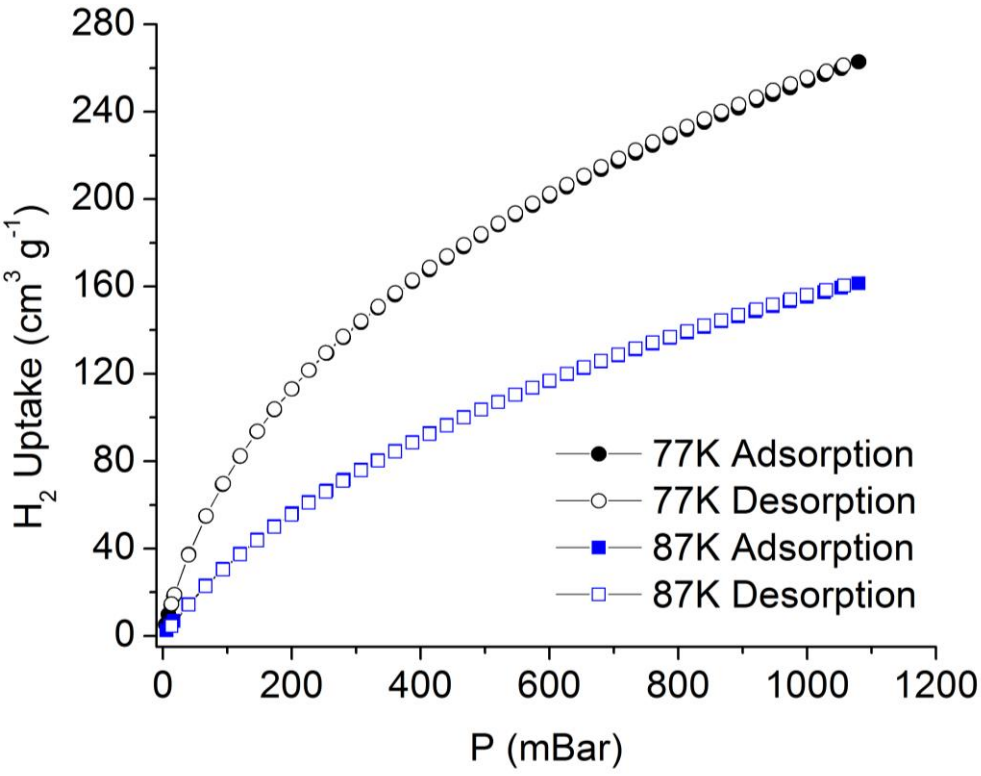

Figure 45. H_2 gas sorption isotherms of PCN-922.

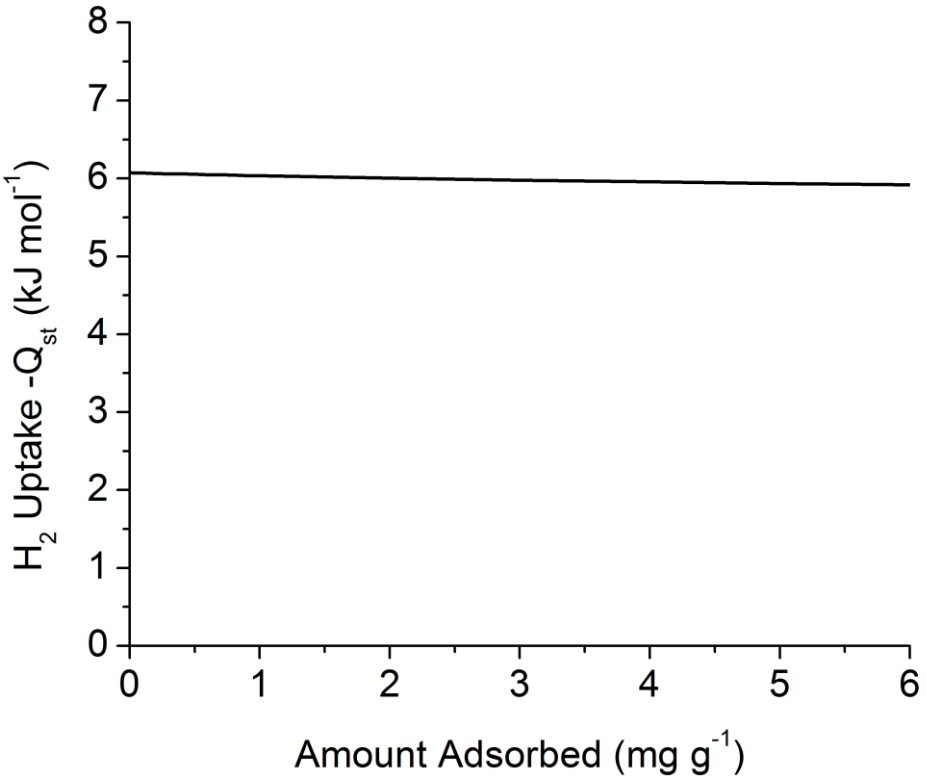

Figure 46. Coverage dependence of the isosteric heats of adsorption calculated from the H_2 sorption isotherms of PCN-922.

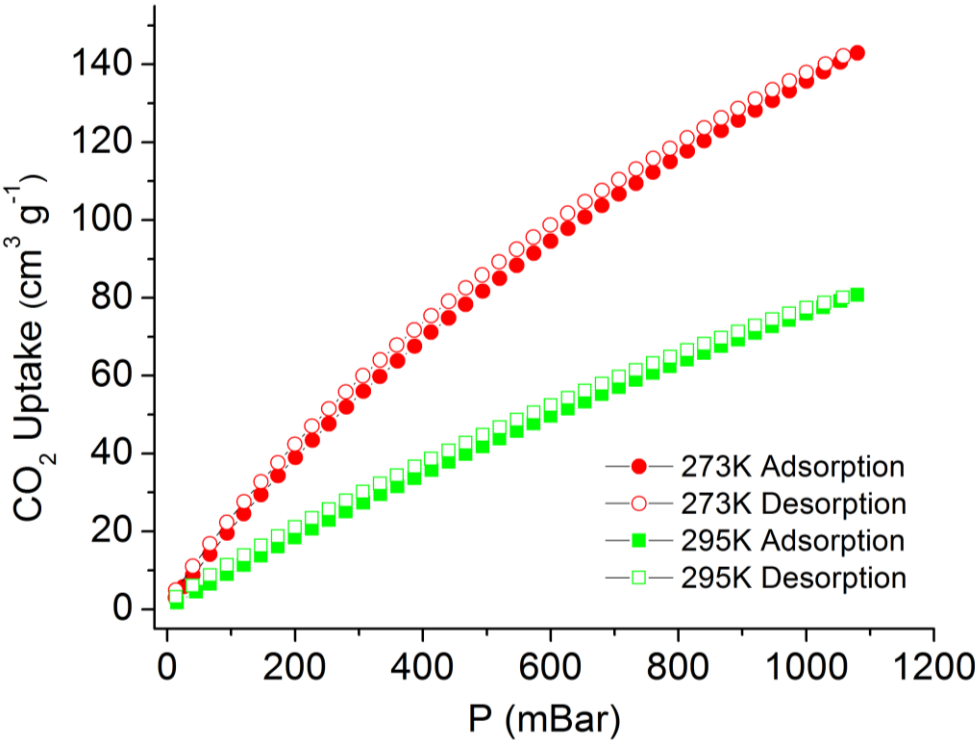

Figure 47. CO_2 gas sorption isotherms of PCN-922.

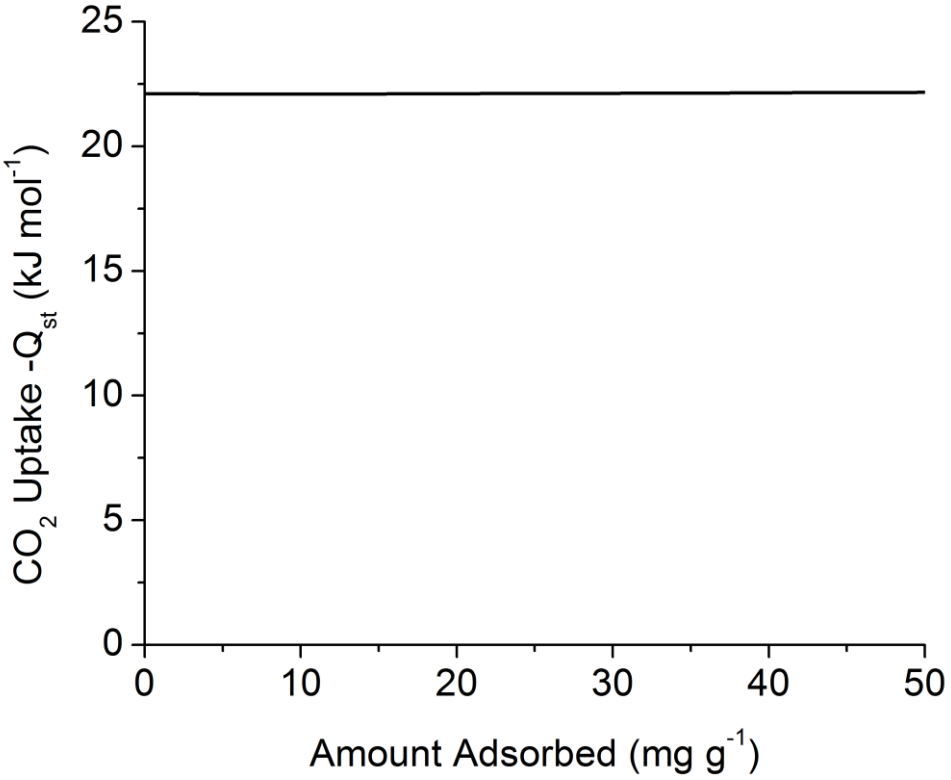

Figure 48. Coverage dependence of the isosteric heats of adsorption calculated from the CO_2 sorption isotherms of PCN-922.

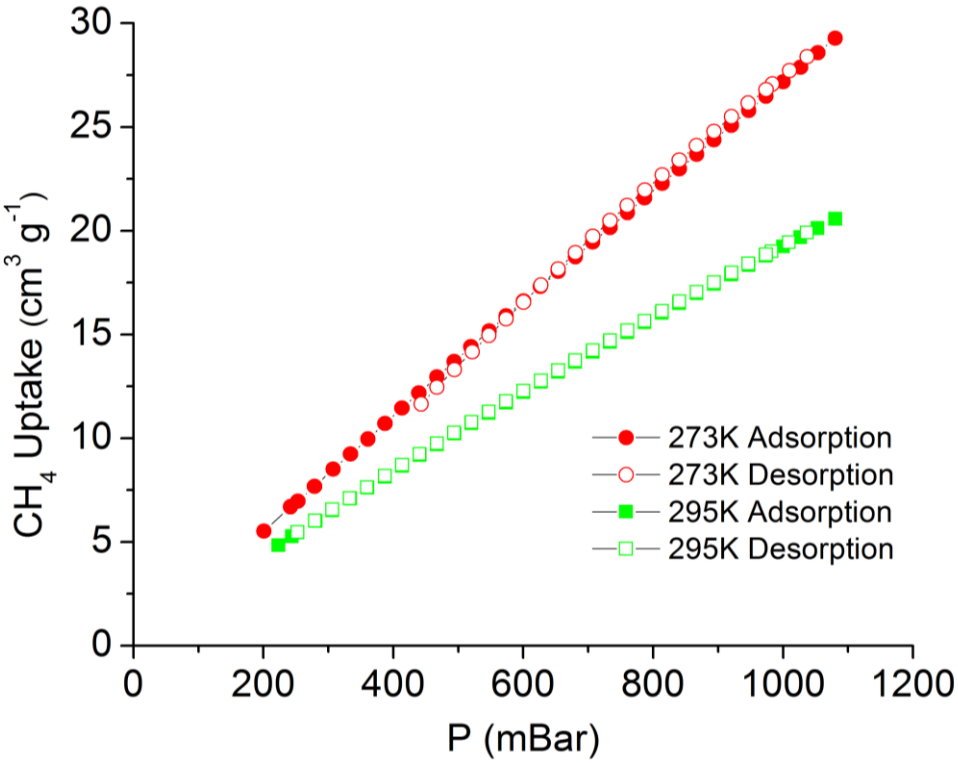

Figure 49. CH_4 gas sorption isotherms of PCN-922.

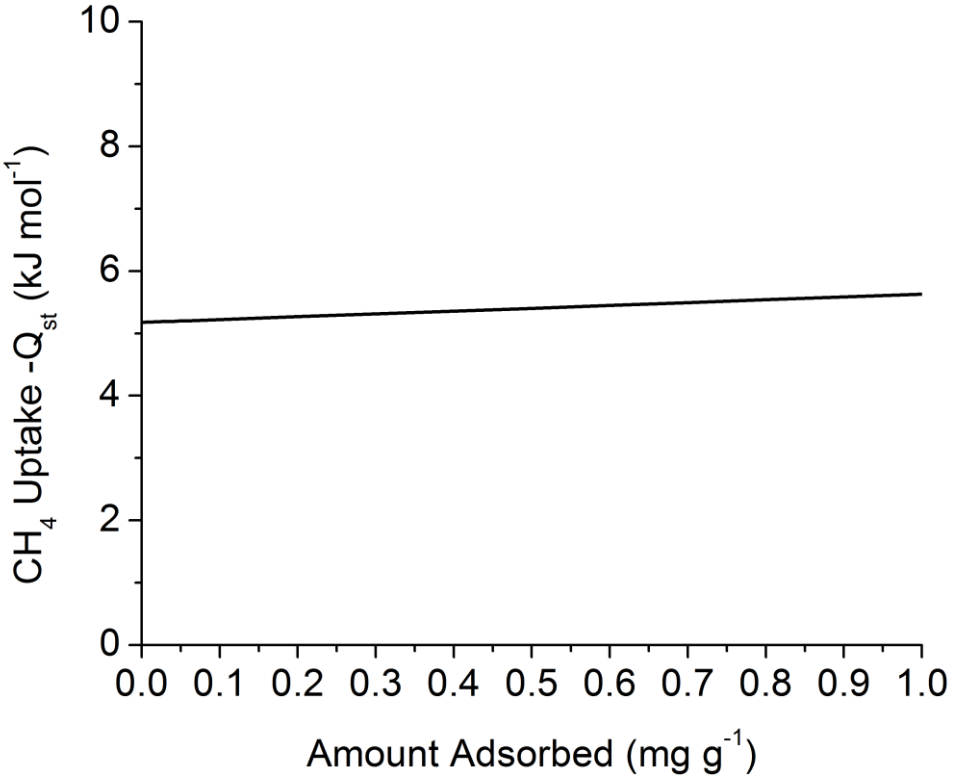

Figure 50. Coverage dependence of the isosteric heats of adsorption calculated from the CH_4 sorption isotherms of PCN-922.

The microporosity, high density of open metal sites, and the robustness of PCN-922 encouraged us to investigate its gas adsorption capacity (Figure 45 to Figure 50). Hydrogen uptake of PCN-922 can reach 263 $cm^3\ g^{-1}$ (2.3 wt%) at 77K and 1 bar.[19] PCN-922 also exhibited high CO_2-uptake (142.97 and 80.78 cm^3g^{-1} at 273 and 298 K, respectively). Both the H_2 and CO_2 uptakes of PCN-922 are higher than those of most reported MOFs.[19, 22] Meanwhile, the CH_4 sorption isotherms indicate that PCN-922 has an adsorption capacity of 29.3 and 20.56 cm^3g^{-1} at 273K and 298K, respectively.

3.4 Conclusions

In summary, a robust and porous MOF, PCN-922, which could not be assembled directly from Cu(II) salts and an octatopic carboxylate linker ETTB by conventional one-step synthesis, has been successfully synthesized with a framework-templating strategy by using a Zn-based MOF as a template to prearrange the linkers in place. PCN-922 has high gas uptakes and may be used for carbon capture and hydrogen/methane storage. This framework-templating synthetic route may become a general way for the preparation of MOFs that are otherwise difficult to crystallize.

4. RIGIDIFYING FLUORESCENT LINKERS BY MOF FORMATION FOR FLUORESCENCE BLUE SHIFT AND QUANTUM YIELD ENHANCEMENT

4.1 Introduction

Fluorescent solid materials have attracted significant attention because of their wide applications especially as inorganic and organic light-emitting diodes (LEDs and OLEDs, respectively) and solid state sensors.[170-174] Discovering new fluorescent materials with intriguing properties, such as stimulus responsiveness and high porosity, will facilitate the development of functional materials to the current inorganic and organic solid semiconductors. Despite the large diversity of small organic fluorescent molecules providing infinite potential candidates to prepare fluorescent and phosphorescent solids, these materials usually suffer from self-quenching and consequent low quantum yield of their photo- or electro-luminescence.[16] Herein we propose a unique strategy, rigidifying fluorescent linkers by metal-organic frameworks (MOFs) formation, to effectively tune the frontier orbital energy gap (or semiconductor band gap) and improve the photoluminescence quantum yield.

MOFs, which are constructed from inorganic metal-containing nodes and organic linkers bearing large internal surface areas, diverse structures, and versatile functionalities,[1, 3-5, 7-9, 13, 14, 16, 18-20, 22-26, 28, 60, 62, 66, 68, 73, 74, 78, 116-119, 123, 124, 175-178] are promising candidates as tunable OLED emitters and luminescent sensors. Their

luminescence originates from metal cations - most commonly lanthanides, the organic linkers, or charge transfers between transition metal centers and their linkers.[16, 179-186]

Rigidifying linkers in MOFs has two distinctive advantages. First, the linkers can adopt some special conformations that would otherwise be impossible, hence producing different fluorescence and/or absorption energies. Second, the linkers fixed in the porous frameworks have longer intermolecular separations and, as a result, increased photoluminescence quantum yield due to decreased self-quenching. It will be of great scientific and technological significance to show a proof-of-concept demonstration that rigidifying fluorescent linkers by fixing them into a MOF would efficiently and substantially tune the electronic transition energies and raise the quantum yields.

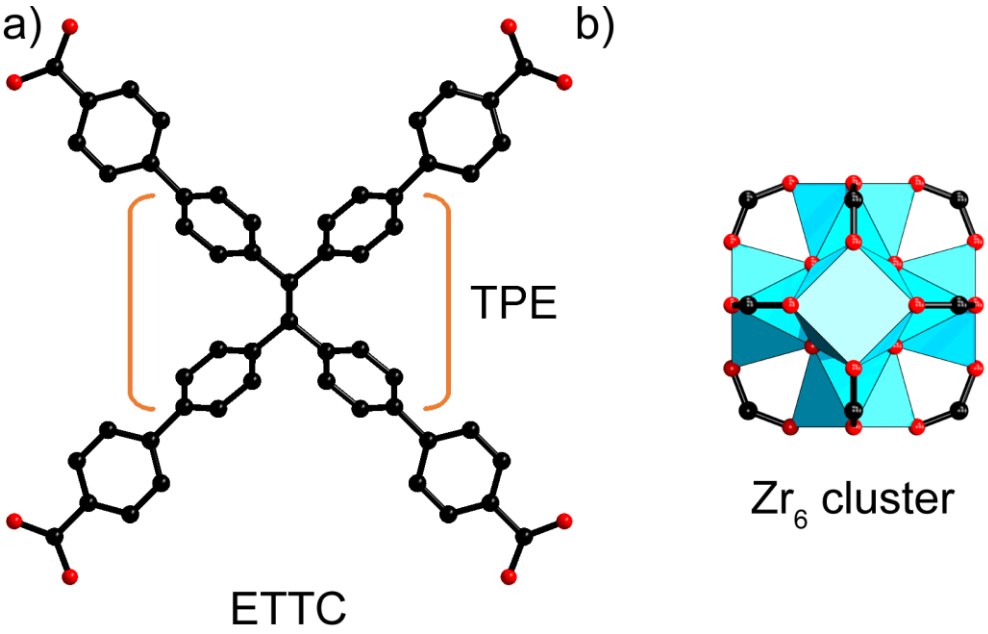

Figure 51. a) ETTC in PCN-94, orange brackets indicate the TPE core; b) Zr_6 cluster.

As a conventional fluorophore, tetraphenylethylene (TPE) (Figure 51a), is well-known for its aggregation-induced emission (AIE) character.[187] Nevertheless, only several pioneering papers have discussed the utilization of TPE in MOFs to turn-on its fluorescence.[188-191] On the other hand, further applications of reported TPE-based MOFs are limited due to their moisture-sensitivity originating from the labile coordination bonds between divalent metal cations and carboxylate linkers.

Here we undertake a combined structural/spectroscopic study of a new extended TPE-based linker and a robust zirconium MOF thereof (PCN-94, where PCN stands for "porous coordination network") that exhibits remarkably-high fluorescence quantum yield in the solid state, among other unusual photophysical properties. We designed and synthesized a tetracarboxylate linker, 4',4''',4'''',4''''''-(ethene-1,1,2,2-tetrayl)tetrakis(([1,1'-biphenyl]-4-carboxylic acid)), henceforth denoted as "H_4ETTC", and crystallized it with Zr(IV) (Figure 52). Given the loss of 5s and 4d electrons in Zr(IV), the resulting closed-shell electronic configuration is employed for building fluorescent MOFs that preclude paramagnetic quenching by the metal center[192] yet maintain the extraordinary chemical and thermal stability known for Zr-MOFs.[35, 39, 69, 193-196] Rigidifying the yellow-emitting TPE-based organic linker, H_4ETTC into PCN-94 produced ultra-bright blue fluorescence with quantum yield as high as 91% under inert atmosphere and room temperature. This rigidifying methodology provided a promising approach for the development of deep-blue emitters with high fluorescence quantum yield, which are highly coveted in white OLEDs for solid-state lighting or video display applications.[173, 174]

4.2 Experimental Section

General information. The electronic absorption spectra were measured on a Hitachi U-4100 UV-Vis-NIR spectrophotometer. Steady-state luminescence spectra were acquired with a PTI QuantaMaster Model QM-4 scanning spectrofluorometer equipped with a 75-watt xenon lamp, emission and excitation monochromators, excitation correction unit, and a PMT detector. The excitation and emission spectra have been corrected for the wavelength-dependent lamp intensity and detector response, respectively. Lifetime data were acquired using a nitrogen laser interfaced with a tunable dye laser and a frequency doubler, as part of fluorescence and phosphorescence sub-system add-ons to the PTI instrument. The 337.1 nm line of the N_2 laser was used either directly or to pump a freshly-prepared 1×10^{-2} M solution of an organic continuum laser dye such as Coumarin-540A in ethanol, the output of which was tuned and frequency doubled to attain the appropriate excitation used to generate the time-resolved data. Temperature-dependent studies were acquired with an Oxford optical cryostat using liquid nitrogen as the coolant. Quantum yields were measured with integration sphere coupled to the PTI spectrofluorometer. Elemental analyses (C, H) were obtained on a Perkin-Elmer 240 elemental analyzer. Thermogravimetry analysis (TGA) was conducted on a TGA-50 (SHIMADZU) thermogravimetric analyzer. Nuclear magnetic resonance (NMR) data were collected on a Mercury 300 spectrometer. Gas adsorption-desorption isotherms were measured using a Micromeritics ASAP2020 system with ultra high purity (UHP) grade gases. The Kratos Axis Ultra Imaging X-ray photoelectron spectrometer (XPS) was used to get the binding energy of Zirconium (IV) cation. The

powder X-ray diffraction patterns (PXRD) were recorded on a BRUKER D8-Focus Bragg-Brentano X-ray Powder Diffractometer equipped with a Cu sealed tube (λ = 1.54178 Å) at room temperature. Unless otherwise specified, all chemicals were purchased from the chemical source provider and used as received.

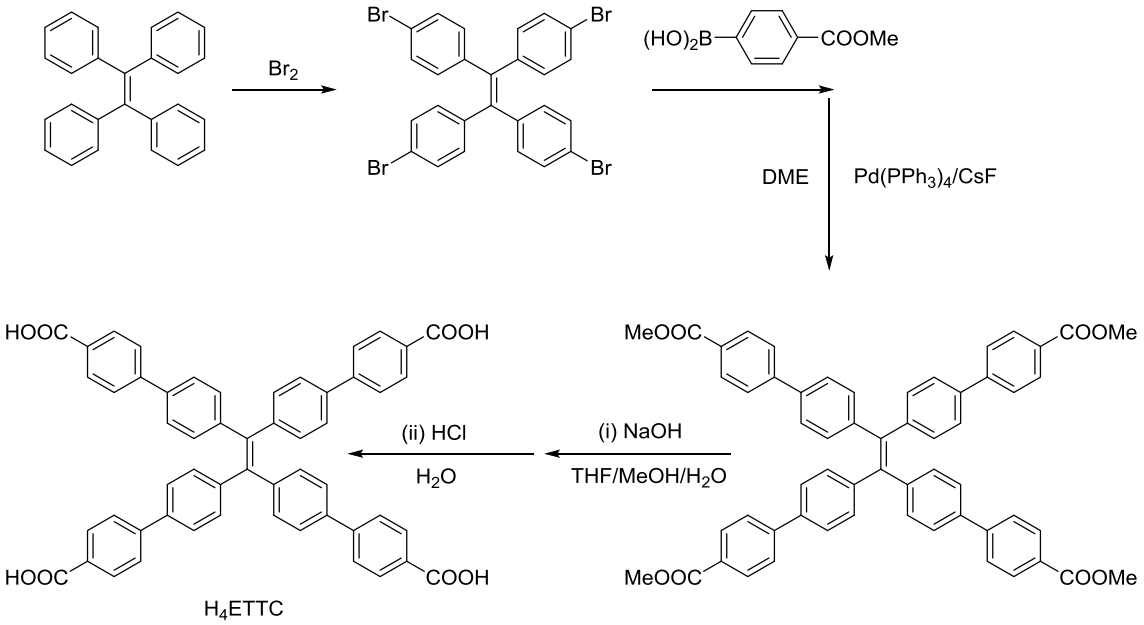

Figure 52. Schematic representation of synthesis route for H_4ETTC.

Synthesis of 4',4''',4'''',4''''''-(ethene-1,1,2,2-tetrayl)tetrakis(([1,1'-biphenyl]-3-carboxylic acid)) (H_4ETTC). (a) Tetrakis(4-bromophenyl)ethane. Powdered tetraphenylethene (4.00 g, 12.0 mmol) was reacted with bromine (7.50 mL, 0.15 mol) vapor under room temperature for 4 days. The resulting solid was

recrystallized in methanol and dichloromethane to yield a white product (5.4 g, 8.4 mmol, 70% yield). ^{1}H NMR (300 MHz, $CDCl_3$): δ 6.85 (d, 8H), 7.28 (d, 8H).

(b) Tetramethyl 4',4''',4'''''',4''''''''-(ethene-1,1,2,2-tetrayl)tetrakis ([1,1'-biphenyl]-4-carboxylate). Tetrakis(4-bromophenyl)ethene (1.5 g, 0.0023 mol), 4-methoxycarbonylphenylboronic acid (2.5 g, 0.014 mol), cesium fluoride (4.2 g, 0.028 mol) and tetrakis(triphenylphosphine)palladium (0.2 g, 0.0002 mol) were added to a 250-mL three-necked flask charged with stir bar. Then 150 mL degassed dimethoxyethane was transferred to the system and the solution was refluxed for 48 hrs. After the reaction mixture was cooled to room temperature, the solvent was evaporated, and the solid was dissolved in dichloromethane and washed with water. The organic part was dried with magnesium sulfate. After removal of the dichloromethane with rotavapor, the solid was recrystallized from acetone to attain light yellow product. (1.6 g, 0.018 mol, 80% yield based on tetrakis(4-bromophenyl)ethene). ^{1}H NMR (300 MHz, $CDCl_3$): δ 3.93 (s, 12H), 7.19 (d, 8H), 7.44 (d, 8H), 7.62 (d, 8H), 8.05(d, 8H).

(c) 4',4''',4'''''',4''''''''-(ethene-1,1,2,2-tetrayl)tetrakis(([1,1'-biphenyl] -4-carboxylic acid)) (H_4ETTC). Tetramethyl 4',4''',4'''''',4''''''''-(ethene-1,1,2,2-tetrayl)tetrakis([1,1'-biphenyl]-4-carboxylate) (1.6 g, 0.0018 mol) and sodium hydroxide (1.7 g, 0.0425 mol) were added into the mixture of tetrahydrofuran (THF), methanol and water (v/v/v=1:1:1). The solution was refluxed overnight. After removal of the organic solvent, the aqueous phase was acidified with 6M HCl to yield a yellow precipitate of 4',4''',4'''''',4''''''''-(ethene-1,1,2,2-tetrayl)tetrakis(([1,1'-biphenyl]-3-carboxylic acid)) (H_4ETTC), which was filtered, washed with water, and dried under vacuum. Yield: 1.4 g

(0.0018 mol, 95%). ^{1}H NMR (300 MHz, DMSO-d^6): δ 7.19 (d, 8H), 7.61 (m, 8H), 7.75 (d, 8H), 7.95 (s, 8H).

Synthesis of PCN-94. (a) $ZrCl_4$ (30 mg), H_4ETTC (15 mg) and benzoic acid (260 mg) in 1.8 mL of *N*,*N*-diethylformamide (DEF) were ultrasonically dissolved in a 4 mL Pyrex vial. The mixture was heated in 120 ºC oven for 24 h. After cooling to room temperature, colorless cubic single crystals were obtained for X-ray structure determination.

(b) $ZrCl_4$ (30 mg), H_4ETTC (15 mg) and acetic acid (0.2 mL) in 1.8 mL of *N*,*N*-dimethylformamide (DMF) were ultrasonically dissolved in a 4 mL Pyrex vial. The mixture was heated in 120 ºC oven for 24 h. After cooling down to room temperature, a white powder of pure-phase PCN-94 was obtained for characterization. Anal. Calcd. (%) for PCN-94: C, 62.73; H, 3.12. Found: C, 61.02; H, 3.41.

Single-Crystal X-ray crystallography. Crystallographic data were collected on a Bruker single-crystal APEXII CCD Diffractometer with Mo K_α (λ = 0.71073 Å) at 110K. All structures were solved by direct method and refined by full-matrix least-squares on F^2 using *SHELXTL*.[168] Non-hydrogen atoms were refined with anisotropic displacement parameters during the final cycles. Organic hydrogen atoms were placed in calculated positions with isotropic displacement parameters set to 1.2 × U_{eq} of the attached atom. The solvent molecules are highly disordered, and attempts to locate and refine the solvent peaks were unsuccessful. Contributions to scattering due to these solvent molecules were removed using the *SQUEEZE* routine of *PLATON*;[137] structures were then refined again using the data generated. Crystal data are summarized in Table 5.

The CIF file can be obtained free of charge from the Cambridge Crystallographic Data Centre via www.ccdc.cam.ac.uk/data_request/cif (CCDC 951017).

Gas adsorption measurements. After cooling to room temperature, as-synthesized PCN-94 (~100 mg) sample was washed twice with DMF and acetone, respectively. Fresh acetone was subsequently added, and the sample was allowed to stay for 24 h to exchange and remove the nonvolatile solvates (DMF). After removal of acetone by decanting, the sample was activated by drying under vacuum overnight, then was dried again by using the "outgas" function of the adsorption instrument for 10 h at 120 ºC prior to gas adsorption/desorption measurement.

Density Functional Theory (DFT) computations. The computations were performed with the DFTB+ and DMol3 programs of Materials Studio 6.0.[197] The resultant energy data of calculated structures are listed in Table 6. Frequency calculations were carried out and analyzed to assess whether the optimized structures represent true minima.

(a) The twisted conformation of H_4ETTC was obtained by changing four Zr cations to protons and removing other Zr cations connected to the ETTC unit in PCN-94. The molecule was optimized through the DFTB+ program by fixing all C and O atoms and relaxing only the H atoms.

(b) The H_4ETTC in free conformation was relaxed with DFTB+ from H_4ETTC in the PCN-94 conformation. Then DMol3 optimization using the PBE functional and DNP 4.4 basis file was performed to attain the final H_4ETTC structure in free conformation.

(c) The HOMO, LUMO, and simulated UV-Vis spectra were obtained with the DMol3 energy calculation using PBE and DNP 4.4 basis files.

Table 5. Crystal Data for PCN-94.

Formula	$C_{162}H_{96}O_{32}Zr_6$
Formula weight	3101.71
Color / Shape	Colorless / Cube
Crystal size (mm^3)	0.30 x 0.25 x 0.20
Crystal system	Cubic
Space group	$Pm\bar{3}m$
a, b, c (Å)	21.104(3)
α, β, γ(º)	90
V ($Å^3$)	9399.1(19)
Z	1
$d_{calc.}$ (g/cm^3)	0.548
μ(mm^{-1})	0.189
T (K)	110(2)
F(000)	1564
Reflns collected	98813
Independent reflns	1867
Obsd data [I>2σ(I)]	1634
Data/restraints/parameters	1867 / 19 / 28
Completeness	99.4 %
GOF on F_2	1.006
Rint	0.1513
R_1, wR_2 [I > 2σ(I)]	0.1188, 0.2496
R_1, wR_2 (all data)	0.1352, 0.2605
$\Delta\rho_{max}$/ $\Delta\rho_{min}$ [$e \cdot Å^{-3}$]	1.579 / -0.890

Table 6. Computational results of H_4ETTC in twist and free conformation.

	H_4ETTC in Twist Conformation	H_4ETTC in Free Conformation
Total Energy (kcal/mol)	-1680963.3	-1681163.3
Zero Point Vibrational Energy (kcal/mol)	464.4	467.4
First Vibrational Frequency (cm^{-1})	—	4.8

4.3 Results and Discussion

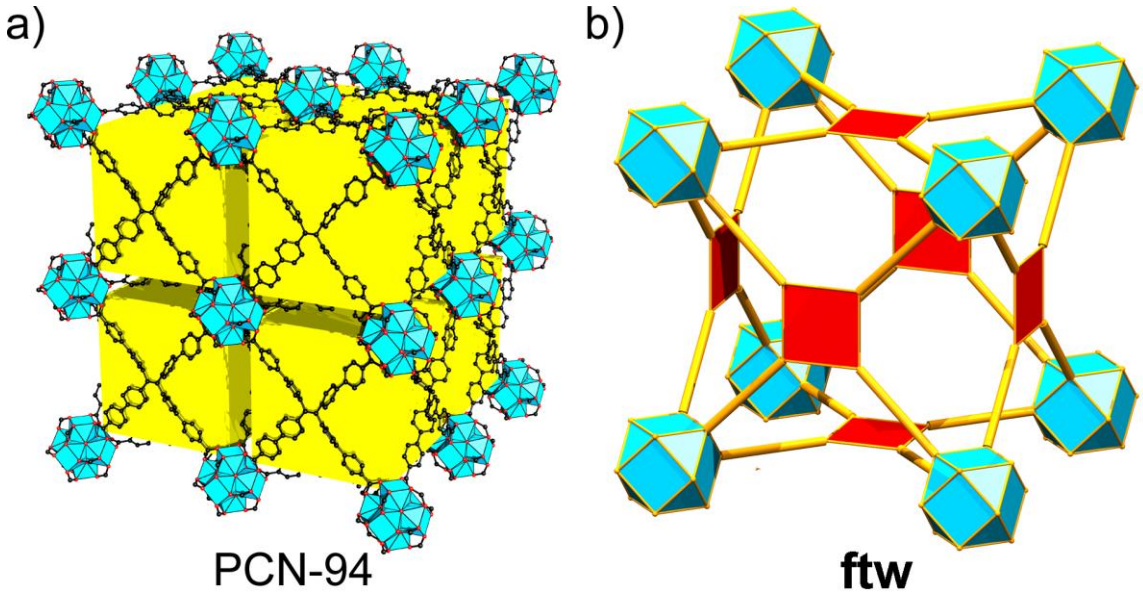

Figure 53. a) PCN-94 framework; b) the **ftw** topology. All H atoms are omitted, and only one orientation of disordered atoms is shown for clarity. Atom color: black, C; red, O; blue polyhedron, Zr; yellow cube, cavity with 17.5 Å edge.

Rigidifying the TPE-based Linkers by MOF Formation. PCN-94 crystallizes in space group *Pm*$\bar{3}$*m* with a = 21.104(3) Å (Figure 53). Each disordered ETTC connects to four Zr_6 clusters (Figure 54 & Figure 55). Every Zr_6 cluster is linked to the other eighteen clusters through twelve ETTCs. The framework contains only one type of cubic cages having ca. 17.5 Å edges, with eight Zr_6 clusters occupying the vertices and six ETTCs covering the faces. These cubes are packed as standard containers in the framework (Figure 53a). Along the <1 1 0> direction are windows with size of 14 × 14 $Å^2$ connecting the cubic cavities (Figure 56). From the topological viewpoint, Zr_6 cluster serves as a 12-connected node and the ETTC is simplified as a 4-connected node; the structure of PCN-94 can be simplified as a 4,12-c 2-nodal net with **ftw** topology and the topological point symbol is denoted as $\{4^{36};6^{30}\}\{4^4;6^2\}_3$ (Figure 53b). Similar structures with non-TPE linkers were reported as MOF-525 and MOF-535.[38]

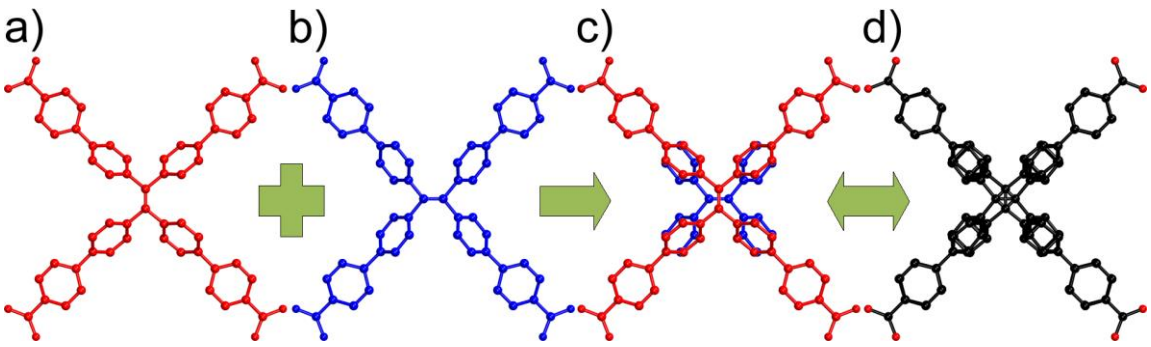

Figure 54. a) ETTC with central C=C double bond in vertical position; b) ETTC with central double bond in horizontal position; c) overlap of the ETTC in different positions; d) the disorder signal of ETTC in solved single crystal structure of PCN-94. All H atoms are omitted.

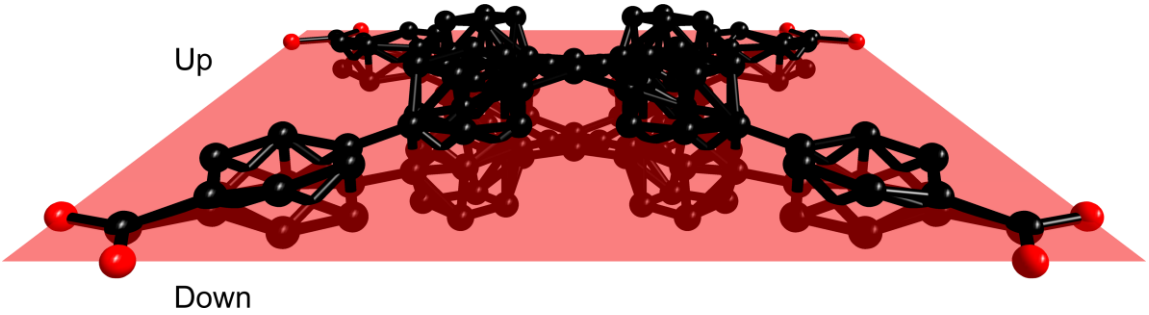

Figure 55. ETTC randomly appeared on both sides of the plane defined by its O atoms in PCN-94. All H atoms are omitted.

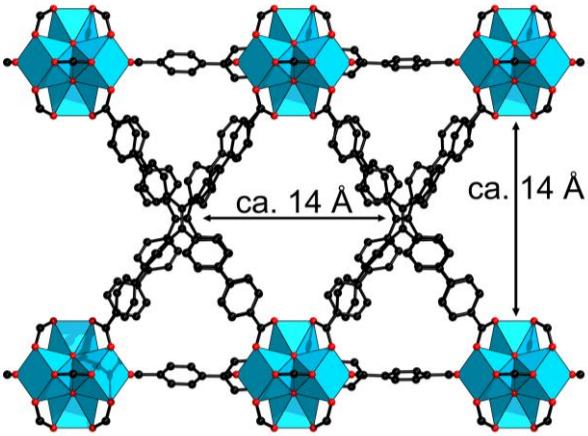

Figure 56. The windows in the PCN-94 along the (1, 1, 0) direction.

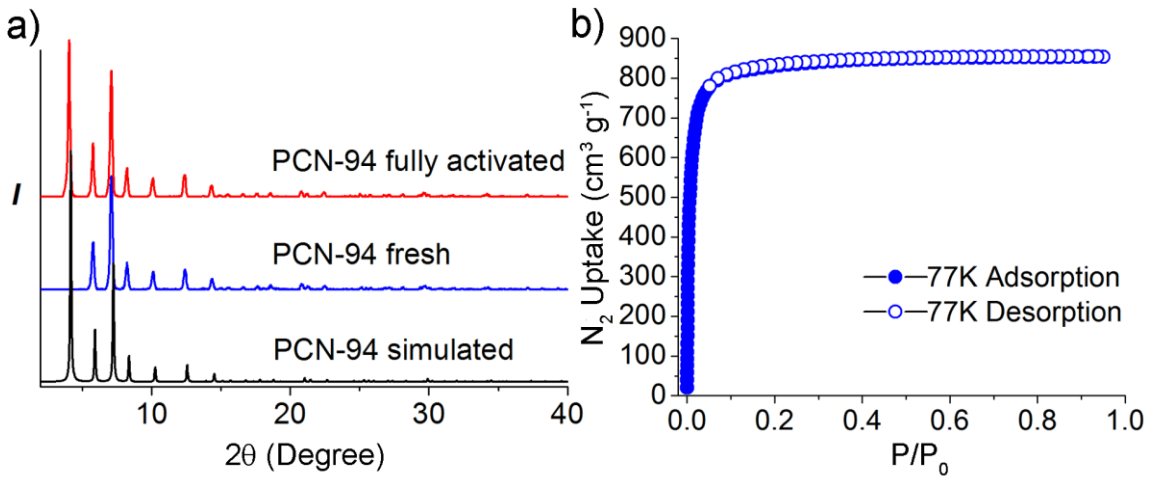

Figure 57. a) PXRD patterns of PCN-94; b) N_2 uptake of PCN-94 under 77 K and 1 atm.

The purity of PCN-94 was examined by powder X-ray diffraction (PXRD) after drying the sample under vacuum at room temperature (Figure 57a). *In-situ* PXRD confirmed that PCN-94 can retain its framework until 473 ℃ under argon atmosphere, which is also supported by traditional TGA (Figure 58). As-synthesized PCN-94 sample was subject to a normal solvent exchange with acetone and heating-vacuum activation process. Then its porosity was evaluated by nitrogen gas adsorption under 77 K (Figure 57b). The Brunauer-Emmett-Teller (BET) and Langmuir surface areas are 3377 and 3732 $m^2 g^{-1}$, respectively (Figure 59).[198] The total pore volume is 1.32 $cm^3 g^{-1}$, matching the calculated value of 1.32 $cm^3 g^{-1}$ from *PLATON* with 1.8 Å probe, indicating that the sample was fully activated.[137] The BET and Langmuir surface areas measured with Ar are 3758 and 4012 $m^2 g^{-1}$, respectively (Figure 60). The gas storage potential of PCN-94

was evaluated by hydrogen, carbon dioxide and methane adsorption measurements (Figure 61 to Figure 66).

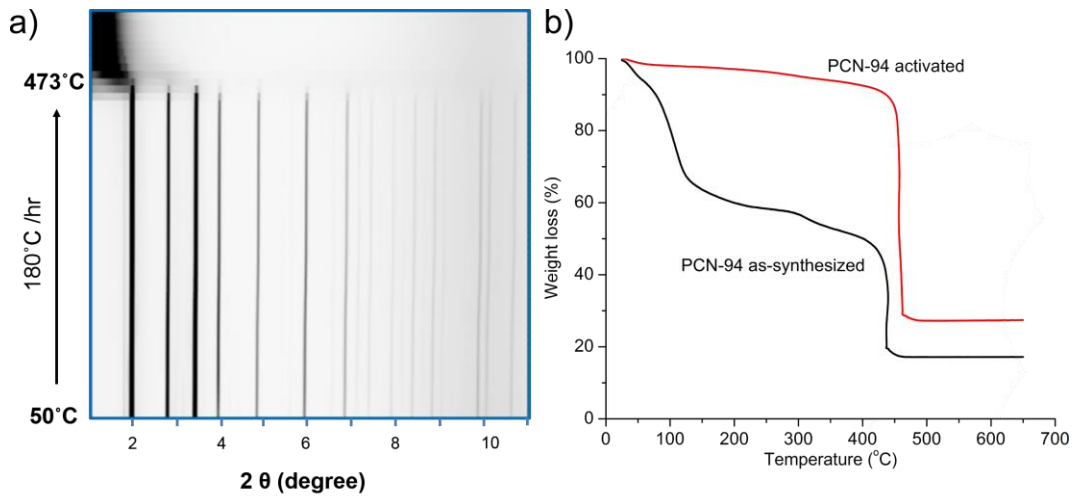

Figure 58. a) Top view of the in situ temperature dependent synchrotron-based powder diffraction (SPD) patterns; b) TGA curves of PCN-94 fresh sample that the decomposition temperature is around 430 °C for fresh sample (black, bottom) and 450 °C for the activated sample (red, top).

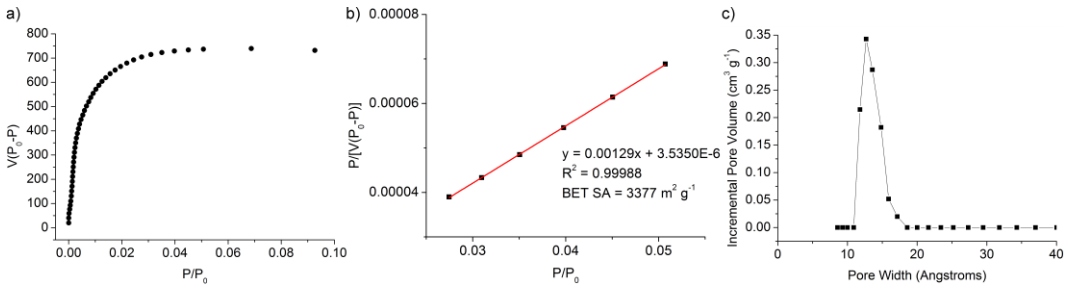

Figure 59. a) Plot [$V(P_0-P)$ vs. P/P_0] for N_2 isotherms of PCN-94 at 77 K and the range below $P/P_0 = 0.06873$ satisfies the BET analysis; b) plot of the linear region on the N_2 isotherm of PCN-94 for the BET equation; c) DFT pore size distribution for PCN-94 using data measured with N_2 at 77K.

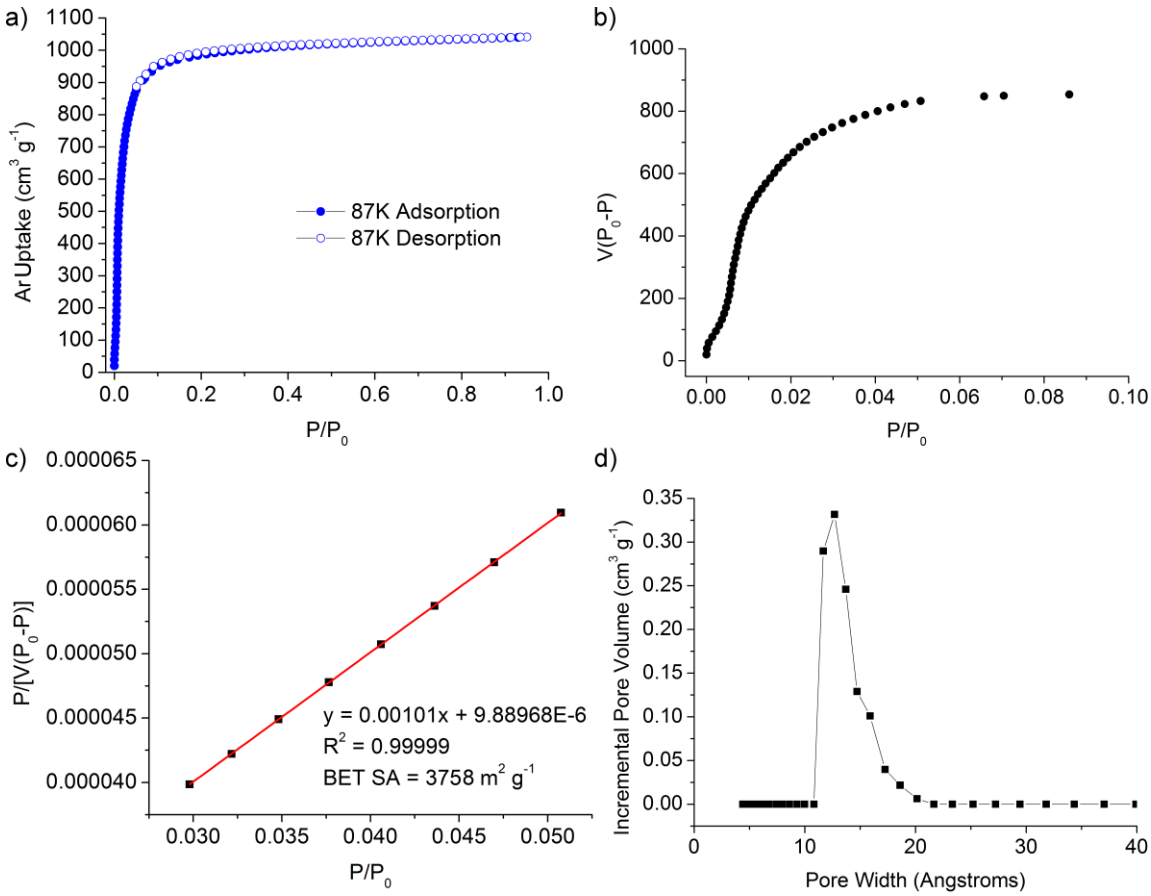

Figure 60. a) Ar uptake of PCN-94 under 87 K and 1 atm; b) Plot [$V(P_0-P)$ vs. P/P_0] for Ar isotherms of PCN-94 at 87 K and the range below $P/P_0 = 0.08596$ satisfies the BET analysis; c) plot of the linear region on the Ar isotherm of PCN-94 for the BET equation; d) DFT pore size distribution for PCN-94 using data measured with Ar at 87K.

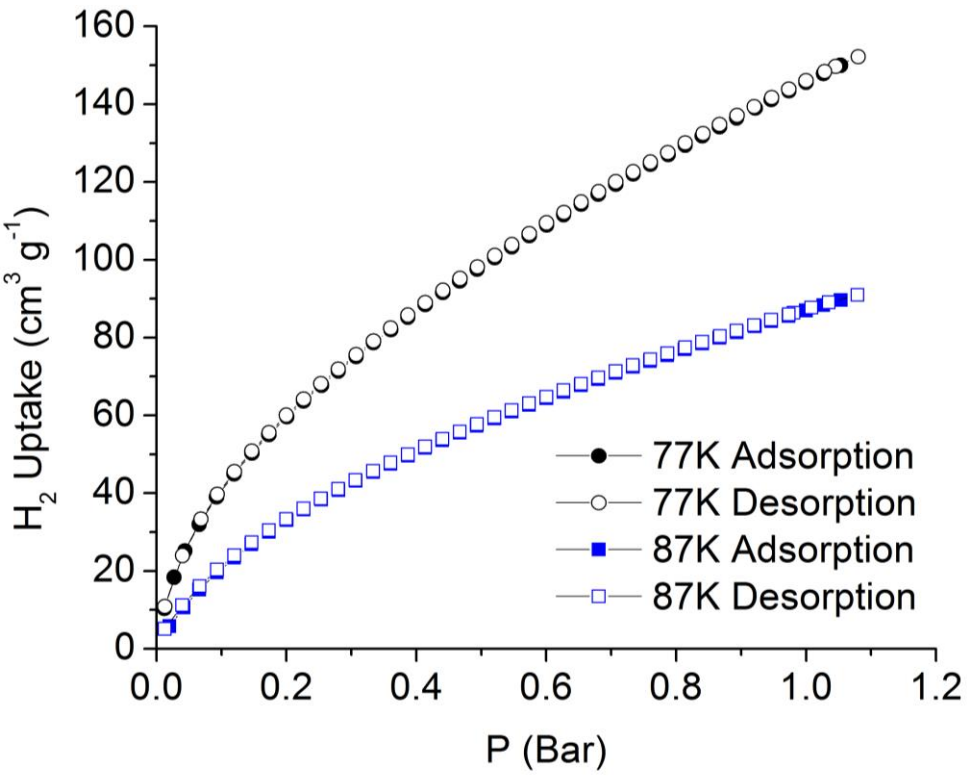

Figure 61. H_2 gas sorption isotherm of PCN-94.

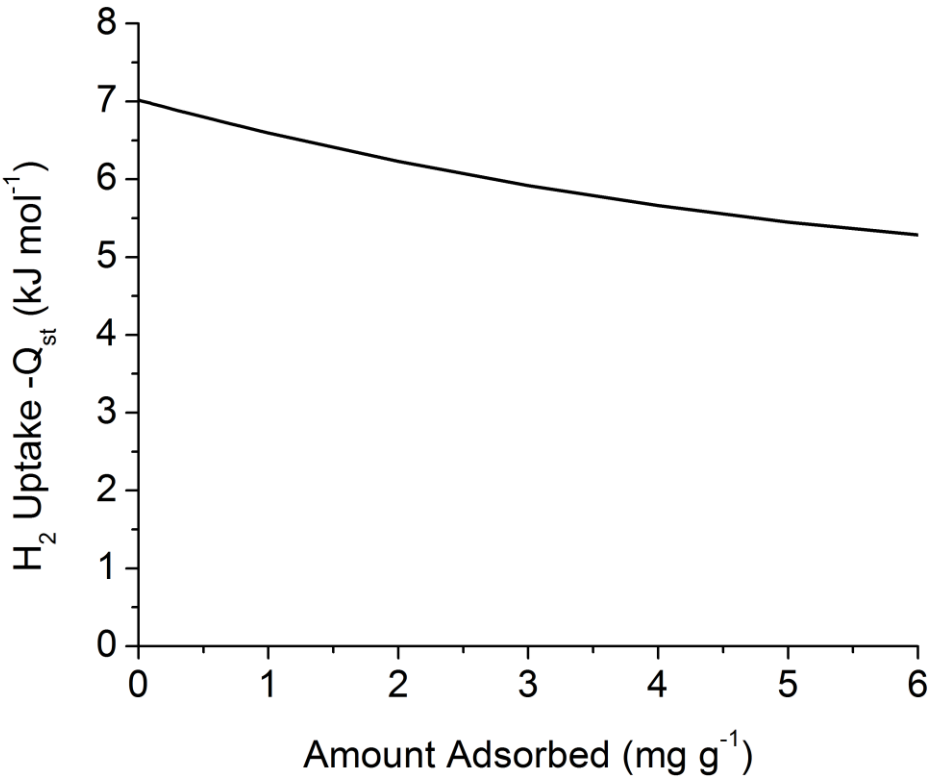

Figure 62. Coverage dependence of the isosteric heats of adsorption calculated from the H_2 sorption isotherms of PCN-94.

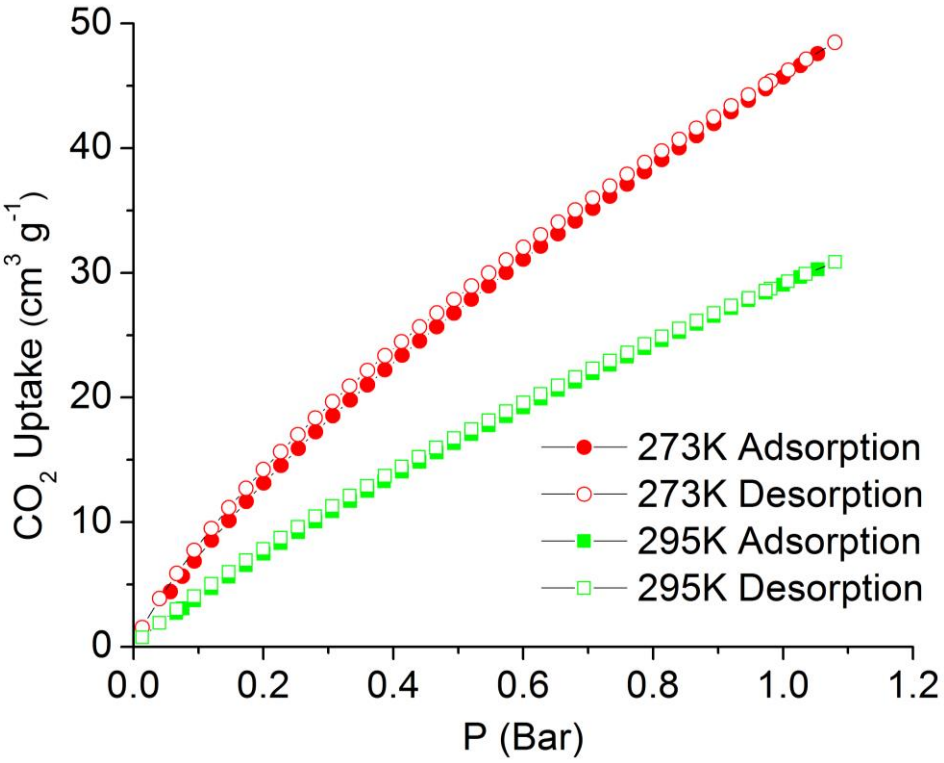

Figure 63. CO_2 gas sorption isotherm of PCN-94.

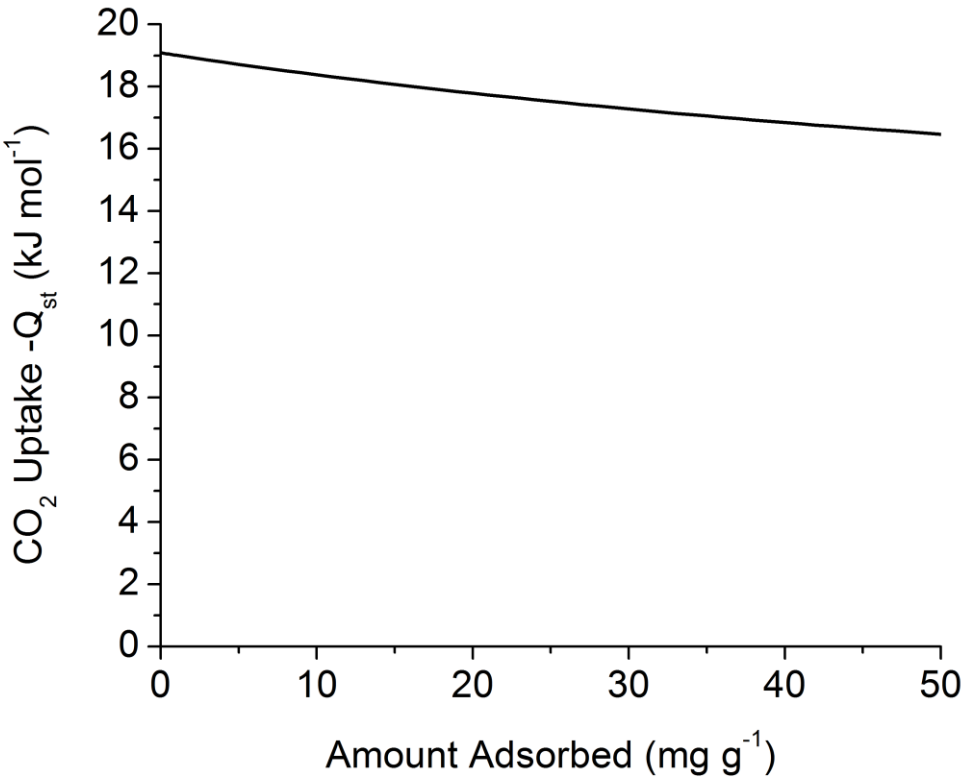

Figure 64. Coverage dependence of the isosteric heats of adsorption calculated from the CO_2 sorption isotherms of PCN-94.

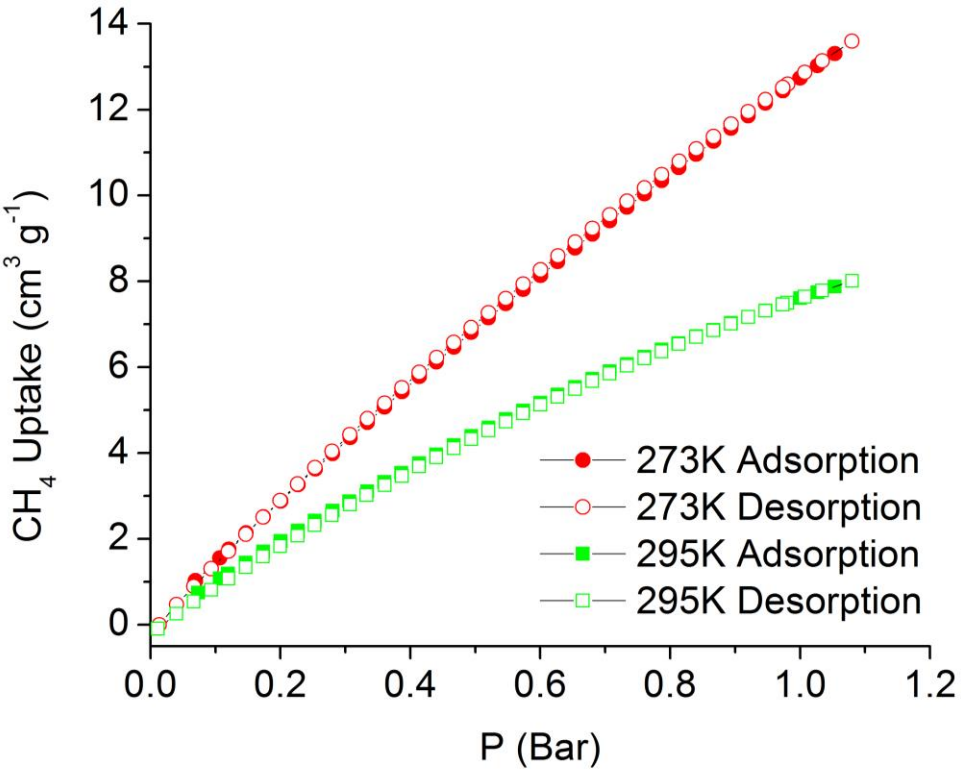

Figure 65. CH_4 gas sorption isotherm of PCN-94.

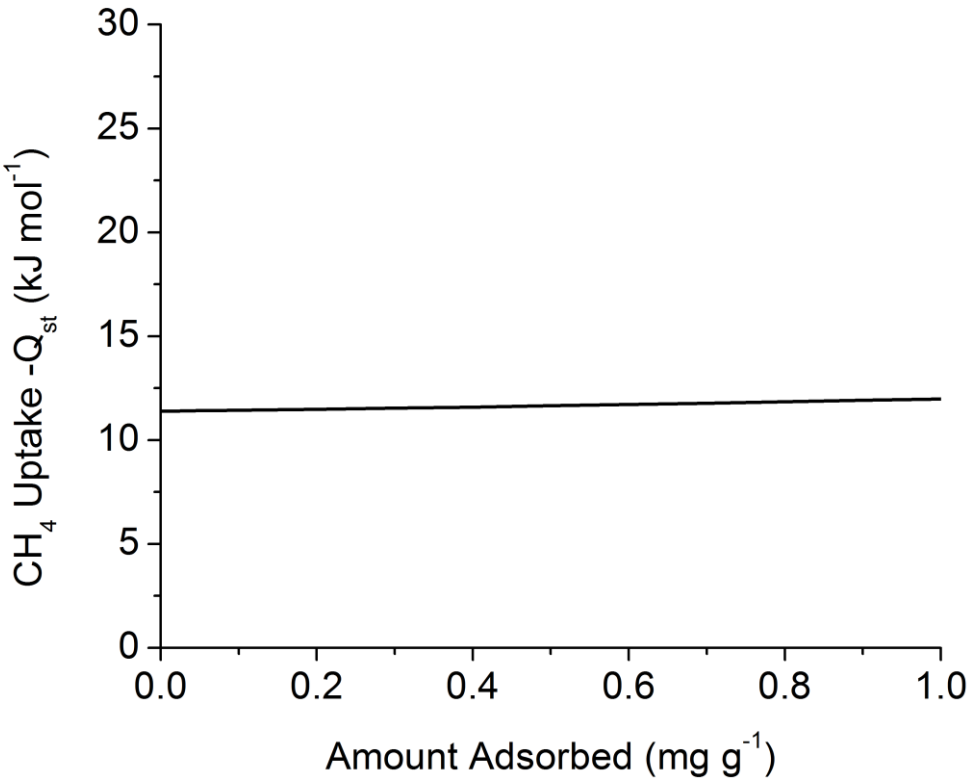

Figure 66. Coverage dependence of the isosteric heats of adsorption calculated from the CH_4 sorption isotherms of PCN-94.

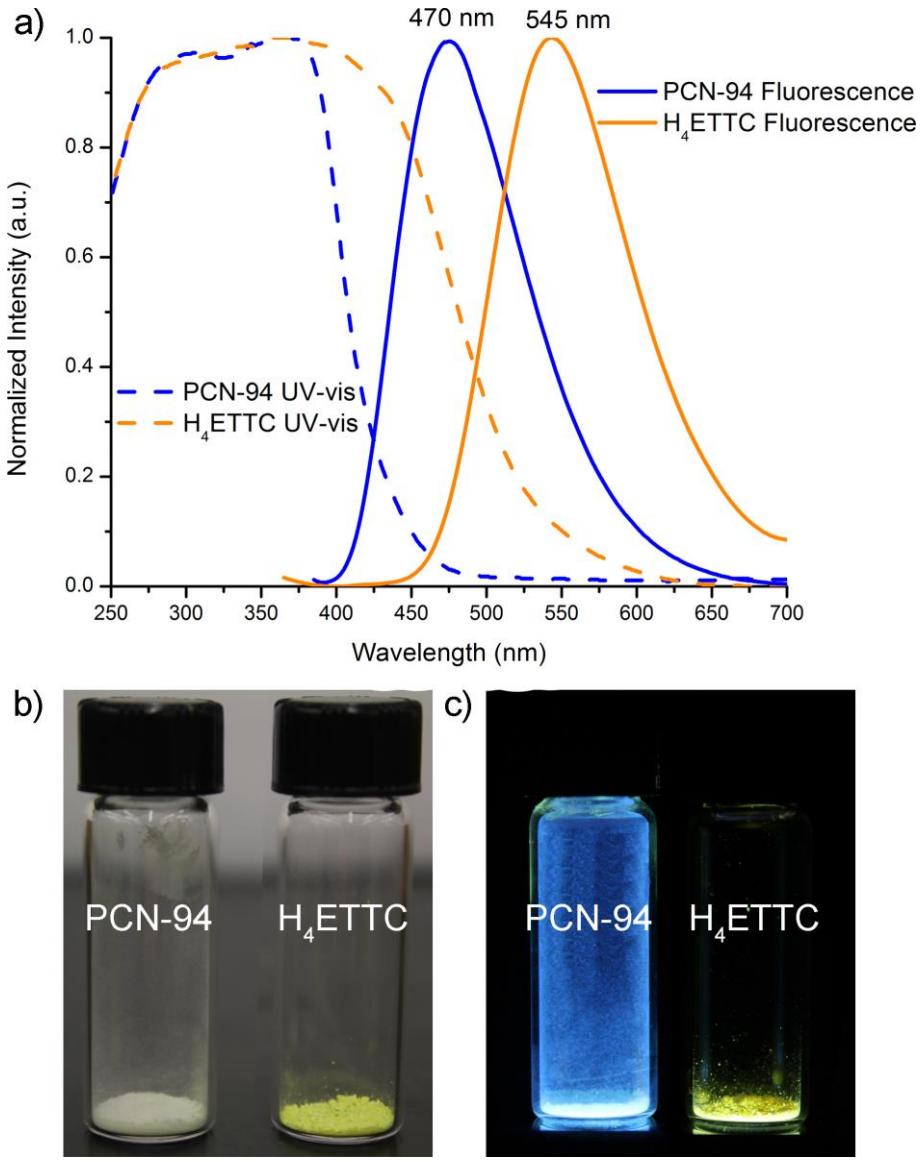

Figure 67. a) Solid-state absorption (via diffuse reflectance; dash lines) and emission spectra (solid lines) of PCN-94 (blue) and H_4ETTC (orange) at room temperature. Photos of PCN-94 and H_4ETTC are shown under b) ambient light and c) UV light**.**

Photophysical properties of the PCN-94. To investigate the solid-state absorption and photoluminescence properties, the diffuse reflectance as well as the solid-state photoluminescence spectra of PCN-94 and its linker precursor H_4ETTC were measured (Figure 67a). The diffuse reflectance spectrum shows that H_4ETTC has a broad absorption profile extending between 250 and 600 nm with two discernible features, whereas PCN-94 exhibits significantly sharper absorption range from 250 to 500 nm, which is clearly blue-shifted compared to the H_4ETTC absorption. Thus PCN-94 and H_4ETTC show distinct colors: H_4ETTC is a bright yellow powder owing to absorbing blue light while PCN-94 is white with slight discoloration because of only absorbing UV light but reflecting all visible light (Figure 67b). The shorter-wavelength absorption feature and the onset of the overlap from the second longer-wavelength feature nearly coincide for the two materials whereas the second band for the H_4ETTC linker precursor extends to the visible region, consistent with self-aggregation of the linker but not the MOF chromophore.

Table 7. Photophysical parameters for PCN-94 and H_4ETTC solids under various conditions.

	PCN-94	H_4ETTC
Quantum yield (%)	76.2±3.5 (air; RT[a])	30.0±0.5 (air; RT)
	91.3±0.5 (N_2; RT)	
Lifetime (ns)	2.06±0.02 (RT)	τ_1=24.74± 0.28
		τ_2=4.15±0.07 (RT)
	1.57±0.01 (70 K)	τ_1=31.54± 0.55
		τ_2=4.87±0.19 (90 K)
	1.83±0.02 (140 K)	
	1.87±0.02 (250 K)	
$\lambda_{em}/\lambda_{exc}$ (nm)	470/375	545/420
		575/500

[a]RT is short for room temperature.

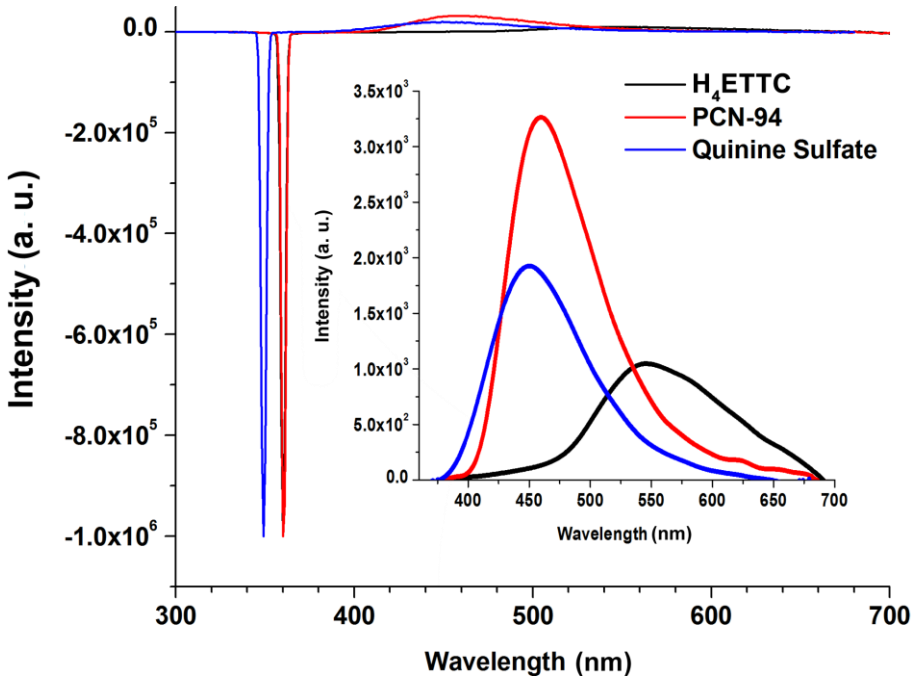

Figure 68. A plot of the emission spectra used for the absolute quantum yield determination of PCN-94, H_4ETTC solids and quinine sulfate solution. The spectra are normalized for the absorption signal at the excitation wavelength used for each sample. The inset shows the expanded portion of the emission scanned within 380-700 nm.

Solid-state photoluminescence measurements show that the emission maxima of PCN-94 and H_4ETTC are at 470 and 545 nm, respectively (Figure 67a). The emission color shifts to blue in PCN-94 from the yellow emission of H_4ETTC (Figure 67c). Moreover, the photoluminescence quantum yield is 76% for PCN-94 in the solid state at room temperature under ambient atmosphere and increases to nearly-unity upon N_2 deaeration (Table 7). This quantum yield is extremely high for PCN-94 compared to all reported fluorescent MOFs, including other TPE-core based MOFs.[188-191] Figure 68 shows the normalized absolute quantum yield of H_4ETTC solid, PCN-94 solid, and the standard reference material quinine sulfate in 1N sulfuric acid/ethanol solution, for

which we obtained 55%, reproducing the reported value, to validate the direct quantum yield methodology followed in this work.[199]

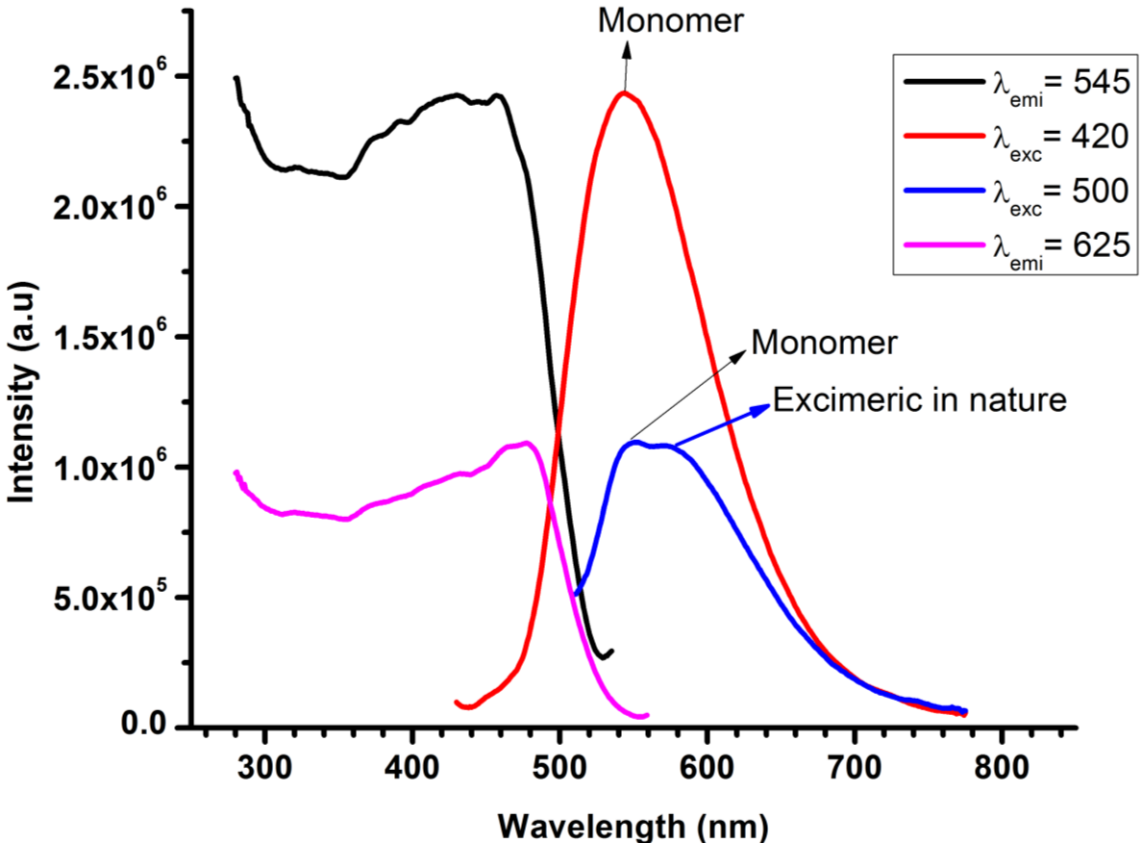

Figure 69. Excitation dependent photoluminescence spectra of H_4ETTC showing monomer and excimeric nature of H_4ETTC in free conformation.

The high quantum yield of PCN-94 is primarily attributed to the immobilization of the ETTC linker as it is strongly coordinated to Zr(IV), and to the diminution of concentration quenching that is very common for luminescent organic molecules.[200] The

coordination of the ETTC to the Zr(IV) cation prevents the free rotation of the phenyl rings, which is the major deactivation pathway for the absorbed energy. The modest increase in the quantum yield of PCN-94 to 91% under blanket nitrogen atmosphere indicates that this complex is highly stable and not prone to significant quenching by oxygen in the atmosphere. The emission decay of PCN-94 is monoexponential with a fluorescence lifetime of 2.06 ns at room temperature (RT), whereas H_4ETTC exhibits a biexponential fluorescence decay. The dual H_4ETTC lifetimes likely originates from monomer and excimer combination with the latter stemming from phenyl ring interactions in adjacent H_4ETTC molecules, which is excimeric in nature (Figure 69).

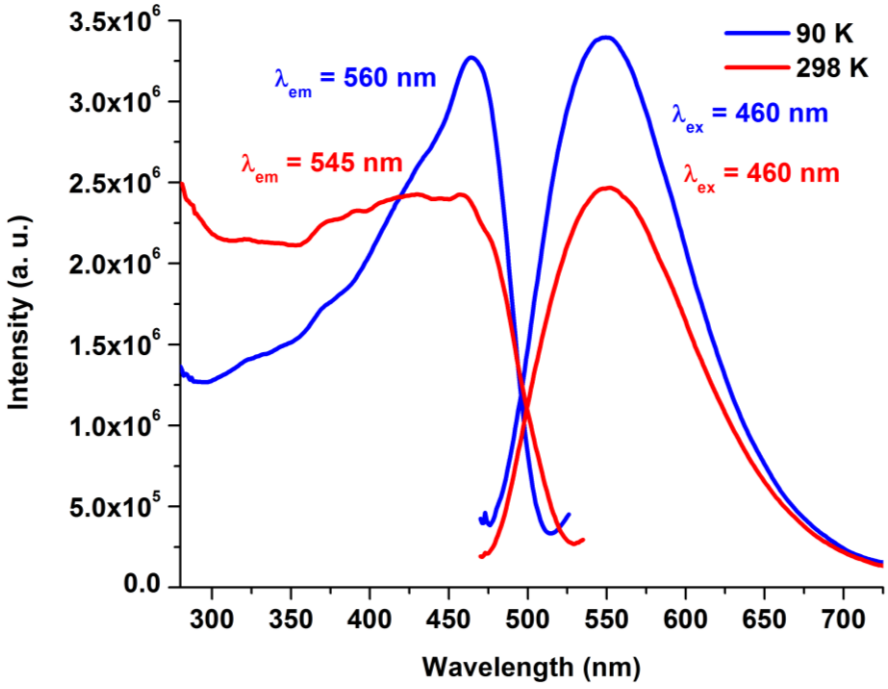

Figure 70. Steady state photoluminescence spectra of H_4ETTC.

Apart from the high quantum yield of PCN-94, an anomalous fluorescence behavior relate to temperature is observed. Generally, as temperature is increased from cryogenic to ambient temperatures, the fluorescence intensity is expected to decrease for most fluorescent materials owing to thermal quenching via multiphoton relaxation pathways. This general behavior is, indeed, observed for H_4ETTC (Figure 70). For PCN-94, however, increasing the temperature from 70 K toward 298 K results in fluorescence intensity exhibits an ascending nature (Figure 71), which also holds true for the corresponding lifetimes (Table 7).

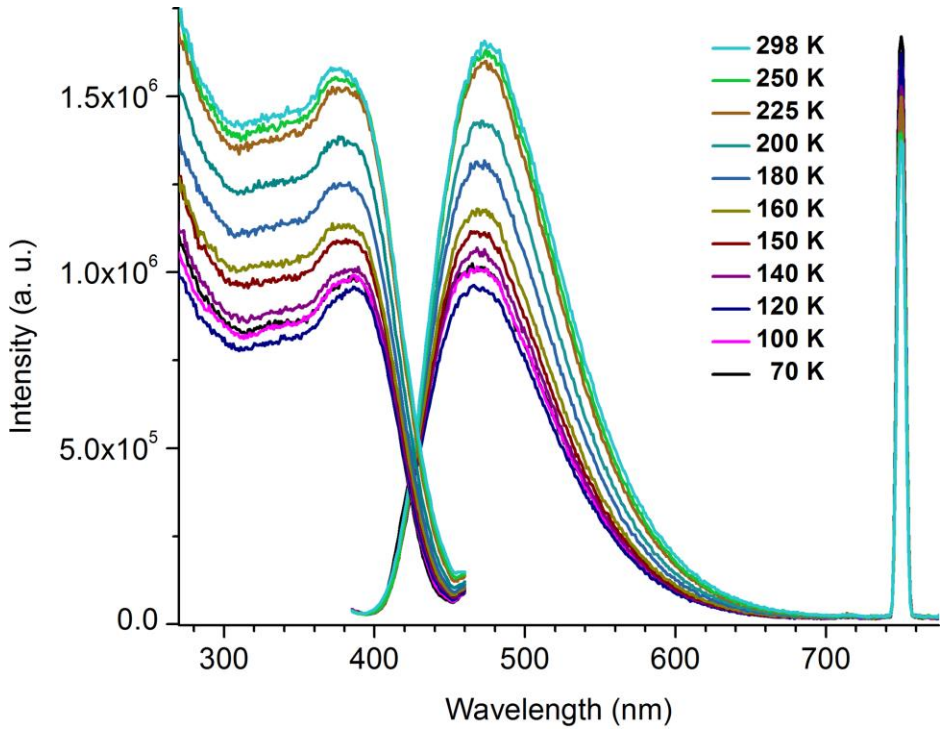

Figure 71. Temperature dependent steady state fluorescence excitation (left) and emission (right) spectra for PCN-94. λ_{exc}= 375 nm and λ_{em}= 470 nm. The 2nd harmonic peak is shown to validate relative fluorescence intensity at different temperature.

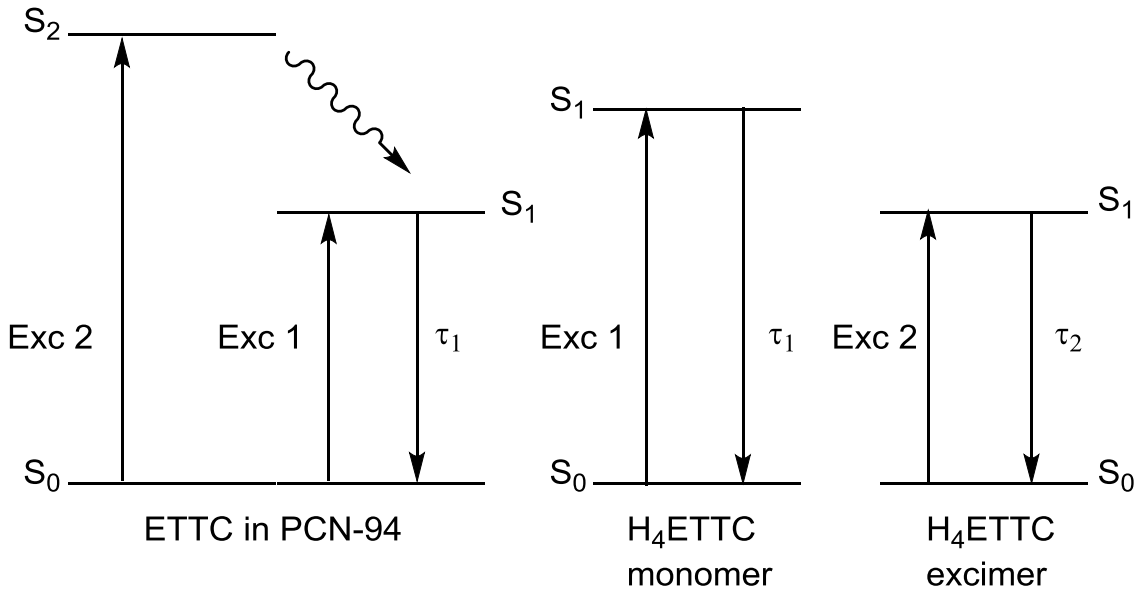

Figure 72. Schematic representation of the electronic transition levels of ETTC in PCN-94 and H_4ETTC.

This seemingly indicates a paradoxical decrease in the non-radiative fluorescence pathways as temperature increases. Aromatic rings would contracts at lower temperatures to increase self-quenching and result in lower fluorescence intensity. Since π-stacking interactions does not exist in PCN-94, it is ruled out as a possible cause for such uncommon behavior. A more reasonable explanation is thermal assistance of the S_2-S_1 internal conversion that supplements the direct excitation route to S_1. The spectral profile of the diffuse reflectance and excitation spectra support such a dual excitation pathway. For H_4ETTC, on the other hand, the biexponential decay comes from different excitation routes of the monomer and dimer/excimer species, each with its characteristic decay independently as discussed above based on the time-resolved data (Figure 70).

Figure 72 summarizes the likely models for the photophysical pathways that account for the PCN-94 and H_4ETTC fluorescence bands.

Based on the peak profile, lifetime, and energy, the emission is described as linker-centered fluorescence. The hypsochromic shift of PCN-94 comparing to H_4ETTC suggests an increase in the HOMO-LUMO energy gap of the ETTC moiety. This blue shift is originally attributed to linker-field stabilization of the filled π levels and/or destabilization of the vacant π^* of the $ETTC^{4-}$ linker upon coordination to Zr(IV) in PCN-94. The high-valence Zr(IV) cation has a closed-shell configuration with all the 5s and 4d valence orbitals empty. These orbitals could overlap with the linker π orbitals and extend the delocalized conjugate system, leading to red-shifted emission.[192] However, we obtain the opposite result. In such case, we propose that the conjugation is not extended to the Zr(IV) metal center in the emissive excited state, which is largely localized on the ETTC moiety. The lack of vibronic structure in the spectral profile even at cryogenic temperatures is likely due to the π-system conjugation involving eight aromatic rings and an unsaturated C=C bond, although we cannot completely rule out partial metal participation in the emissive state. The next section offers more insights on spectral shifts upon rigidified conformation.

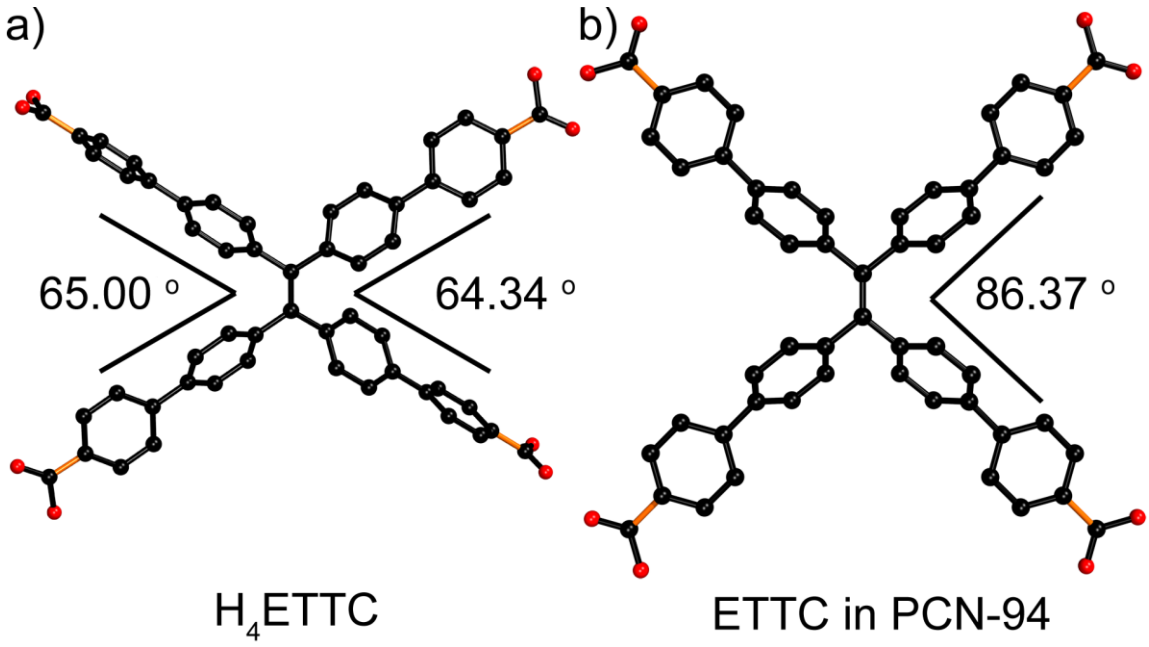

Figure 73. a) H_4ETTC in DFT simulated free conformation; b) ETTC in PCN-94 conformation. The angle between the orange C–O bonds is labeled. H atoms are omitted.

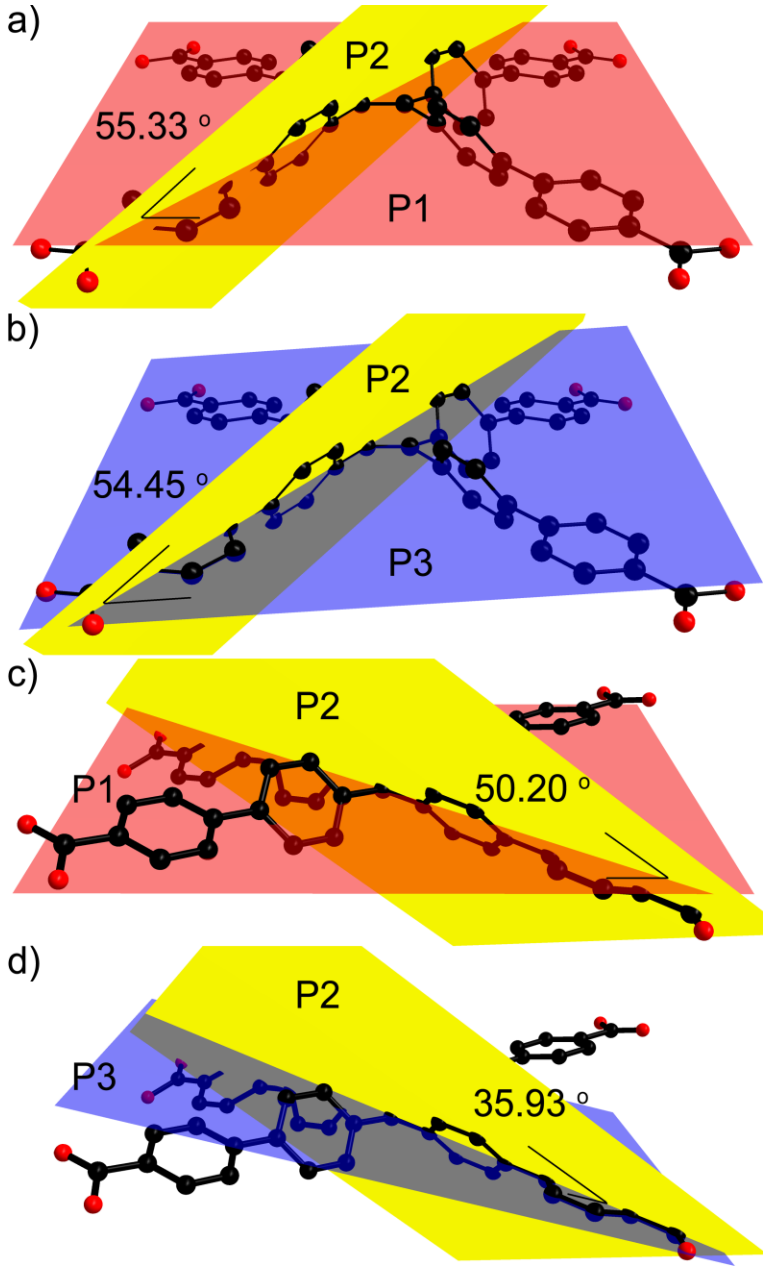

Figure 74. P1 is the average plane of the two C atoms forming central C=C double bound and four C atoms surround them. P2 is the average plane of the phenyl ring adjacent to C=C bond. P3 is the average plane of the phenyl ring adjacent to carboxylate group. The average of dihedral angles are labeled for a) P1-P2 and b) P2-P3 in PCN-94 optimized conformation; c) P1-P2 and d) P2-P3 in free conformation. All H atoms are omitted.

Rigidifying mechanism and molecular simulations. Unlike the free conformation of H_4ETTC, prominent conformational change was observed from the twisted ETTC linker in PCN-94, where the minimum angle between adjacent carboxylate groups of ETTC enlarged from ca. 65° to 86° (Figure 73). The average dihedral angles between the phenyl rings as well as between phenyl rings and the central plane defined by central six carbon atoms of ETTC, P1-P2 and P2-P3, in PCN-94 is much larger than those in free conformation (Figure 74). The larger dihedral angles result in less efficient overlap of the p orbitals of all the sp^2-hybridized C atoms. Thus the delocalized conjugate system of the linker breaks down, leading to a widened band gap between HOMO and LUMO. This breakdown of the conjugate system is mainly responsible for the large blue-shift of light-absorption and emission. To clearly and quantitatively demonstrate the mechanism, DFT calculations were performed on both free and twisted H_4ETTC (Figure 75). By calculating the orbital energies of H_4ETTC in both the free and twisted conformation, the results indicate that the energy gap between the HOMO and LUMO is widened from 2.132 to 2.543 eV, which should lead to higher excitation and emission energies in the latter. Indeed, the simulated UV-Vis spectra (TD-DFT simulations) of H_4ETTC in the twisted conformation shows absorption bands between 400 nm and 500 nm, whereas the free conformation covers longer wavelengths up to 550 nm (Figure 76). The blue-shifted UV-Vis absorption bands for the twisted conformation in these simulated spectra are in agreement with the experimental results. The twisted conformation of ETTC produces a widened band gap, thus producing not

only largely blue-shifted UV-Vis absorption bands, but also blue-shifted fluorescence bands.

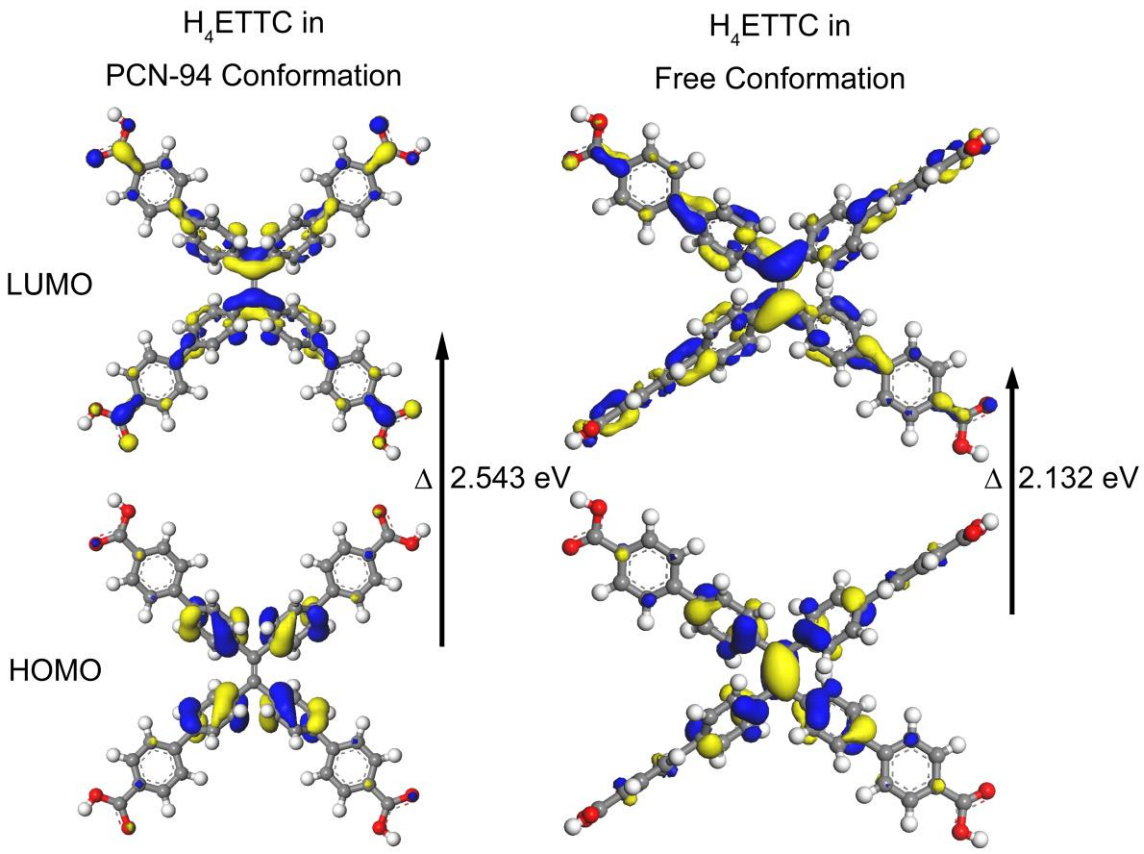

Figure 75. Contour plots of the HOMO and LUMO for H_4ETTC in PCN-94 conformation and in free conformation, respectively.

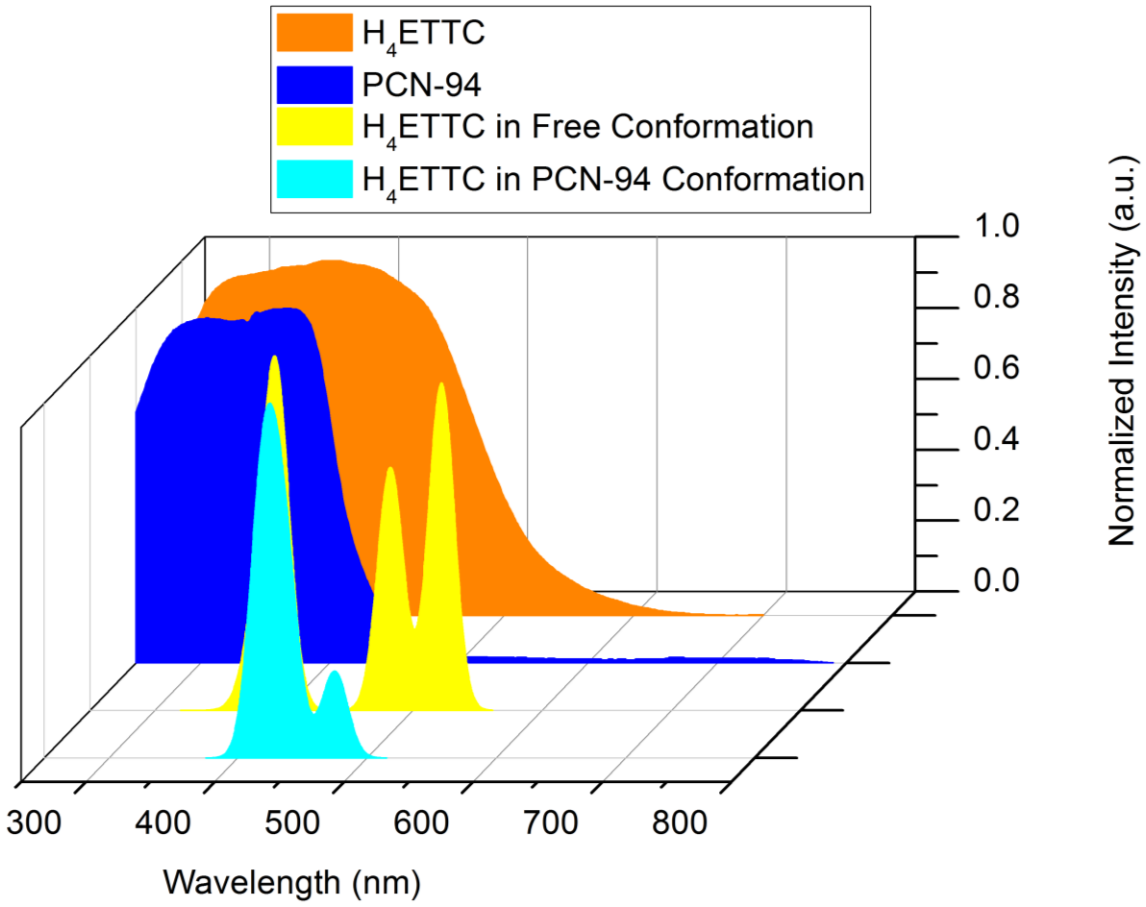

Figure 76. The simulated UV-Vis spectra of H_4ETTC in PCN-94 conformation and in free conformation, as well as the experimental UV-Vis spectra of PCN-94 and H_4ETTC.

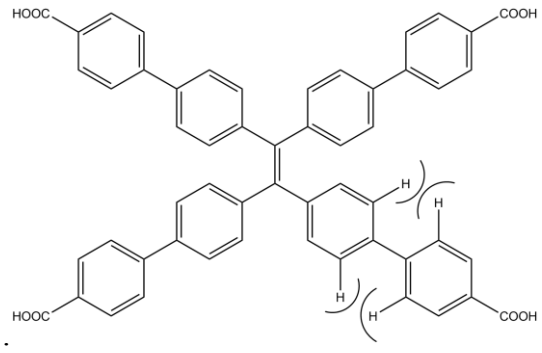

Figure 77. The repulsion between H atoms on adjacent phenyl rings.

Rigidifying linkers also contribute to the quantum yield increase. Fixation of twisted ETTC by the MOF formation separates every ETTC moiety from each other, decreasing the intermolecular interactions. In addition, the repulsion between H atoms on adjacent phenyl rings of ETTC decreases the thermal motion of phenyl rings and intramolecular interactions (Figure 77). Both effectively eliminate thermal motions of ETTC, making the excited linker release the extra energy through fluorescence and substantially increase the quantum yield.[190]

4.4 Conclusions

We have demonstrated that the band gap and quantum yield of fluorophore can be tuned by rigidifying as linkers of metal-organic framework. A highly fluorescent MOF, PCN-94, composed of a TPE-core linker and Zr_6 cluster, was synthesized. The twisted linker conformation in PCN-94 induced bright-blue fluorescence emission at 470 nm, which is hypsochromically-shifted from the 545 nm yellow emission of linker precursor H_4ETTC. The quantum yield of PCN-94 is as high as 91%, which comes from the reduced intra- and inter-molecular interactions. This work has demonstrated a rare example that linker conformation can produce significant effects on photophysical properties of MOFs, which represents a new strategy to attain light-emitting MOFs that may be suitable for potential applications in molecular electronics.

5. PORE SIZE TAILORED METAL-ORGANIC FRAMEWORK FOR METHANE STORAGE

5.1 Introduction

Methane, which is the main content of natural gas, has less C content and releases less CO_2 after combustion compared to gasoline. Methane can also be used in fuel cells, which have higher energy efficiency than combustion engines. Methane is also more naturally abundant and cheaper than oil. Thus, methane is an alternative green energy source to replace oil in many applications. One important application of methane is to replace the gasoline in automobiles.

The current methane storage techniques are mainly liquefied natural gas (LNG) and compressed natural gas (CNG) systems. LNG systems require large amounts of energy to cool methane to nearly 112K (-161 ^{o}C), while CNG systems also demand extra energy to compress methane to 200~248 bar at room temperature.[20, 201, 202] Both systems require special equipment and containers for preparation and storage. All suffer from high expense, safety issues, large energy consumption, and are not compatible with small vehicles. This is why adsorbed natural gas (ANG) systems have attracted a lot of attention. These systems could store methane under relatively low pressure (35~60 bar) and room temperature, avoiding the related issues. For on-board methane storage systems, the main challenge is reach a reasonable volumetric capacity.

Metal-organic frameworks (MOFs) are a class of porous materials showing great application potential for gas storage. At present, the affinity of methane toward adsorbent has been nearly optimized. Strategies have changed from introducing strong interaction sites to designing pores which efficiently wrap methane molecules without dead space (Figure 78). MOFs with large BET surface area are usually mesoporous, and as such cannot pack methane molecules closely and efficiently, leading to low packing density and low volumetric capacity. Thus BET surface areas are not the main target in the search for proper materials. The previous experimental and calculation studies have also demonstrated that MOFs with optimized pores that could accommodate methane molecules efficiently without dead space will have high volumetric capacities.

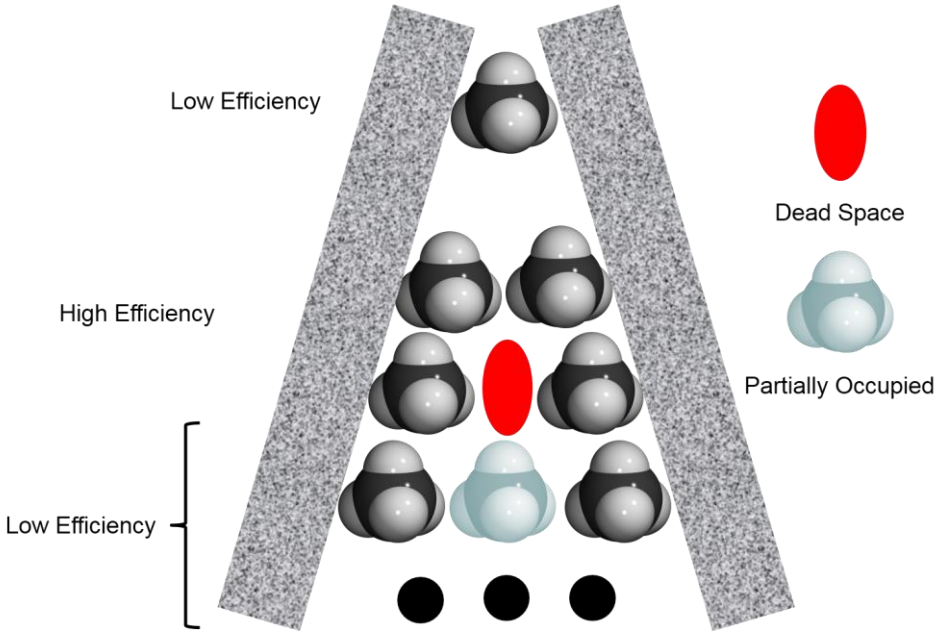

Figure 78. Presentation of high-efficient and low-efficient packing methane molecules in adsorbent pores.

Rht-MOFs are a series of MOFs constructed from planar hexatopic linkers and binuclear paddlewheel SBUs. These MOFs are known for highly porous structures and non-interpenetrated topology. Our group has reported PCN-6X series MOFs with excellent gas storage capacities (Figure 79a).[53, 125] It is worth to indicating that as the linker size become larger, although the gravimetric uptake becomes higher, the volumetric uptake for methane becomes lower, confirming that mesopores have a negative effect on volumetric uptake (Figure 79b & c).[53] PCN-61 contains three types of polyhedral cages (Figure 80). The cuboctahedron cage with 12 Å pore size, which also appears in PCN-66 and PCN-68, could efficiently pack 8 methane molecules. Keeping the cuboctahedron intact and reducing the size of other two polyhedra may effectively increase the methane volumetric uptake.

We reported that by tailoring the pore size of PCN-61, PCN-62, which has been reported as Cu-TPBTM,[203] has been synthesized and evaluated, showing excellent methane storage working capacities.

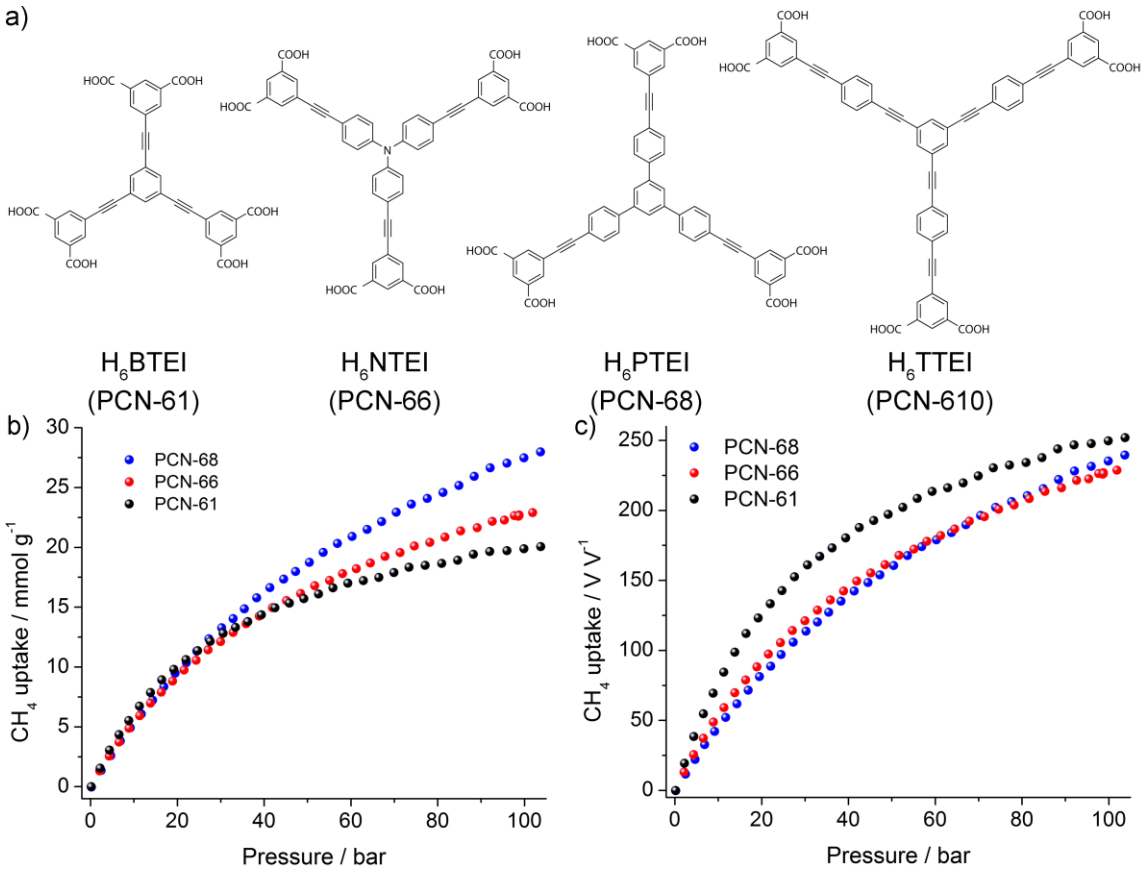

Figure 79. a) The linker precursors of PCN-6X series; b) gravimetric and c) volumetric capacities of CH_4 adsorption in the PCN-6X series at 298K.

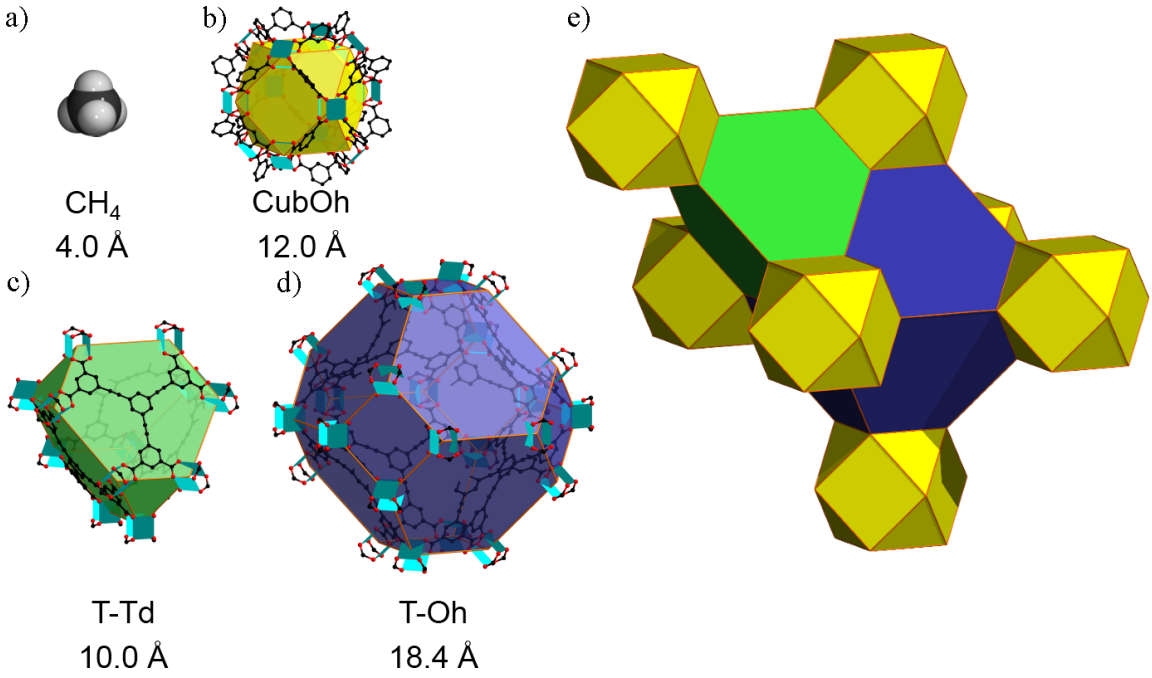

Figure 80. a) Methane molecule; the polyhedra and their pore sizes of PCN-61, including b) cuboctahedron, c) truncated tetrahedron, and d) truncated octahedron; e) the packing of the polyhedra in PCN-61.

5.2 Experimental Section

General information. Commercially available reagents were used as received without further purification. Nuclear magnetic resonance (NMR) data were collected on a Mercury 300 MHz spectrometer. Low pressure gas adsorption-desorption isotherms were measured using a Micromeritics ASAP2020 system with ultra high purity (UHP) gases.

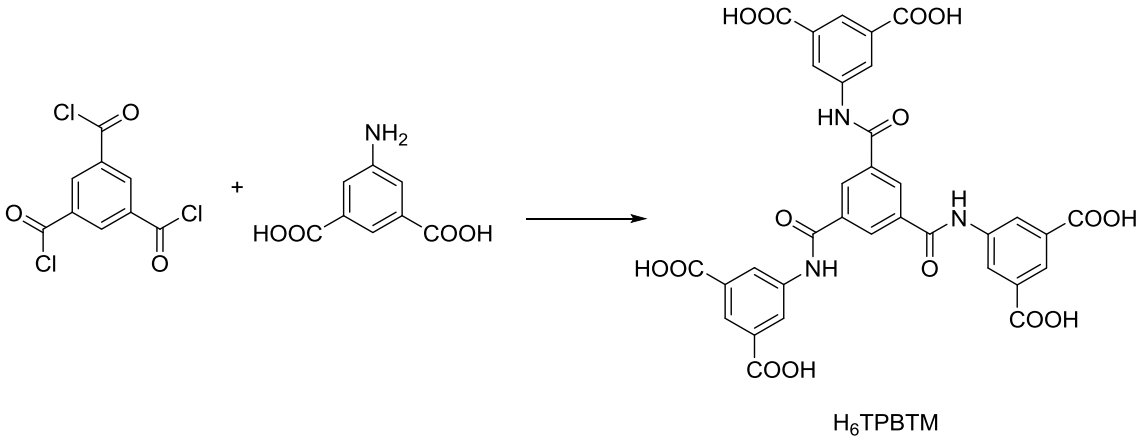

Figure 81. Schematic representation of synthetic route for H_6TPBTM.

Synthesis of 5,5',5''-((benzene-1,3,5-tricarbonyl)tris(azanediyl))triisophthalic acid (H_6TPBTM). 1,3,5-Benzenetricarbonyltrichloride (1.593 g, 6.0 mmol, FW: 265.48) was dissolved in anhydrous acetonitrile (60 mL) and added dropwise to a solution of 5-aminoisophthalic acid (3.81 g, 21 mmol, FW: 181.15) in acetonitrile (60 mL). Then 100 mL anhydrous tetrahydrofuran (THF) was added to the reaction mixture. The resulting mixture was refluxed for 24 h under nitrogen. When the reaction mixture was hot, the precipitated white solid was isolated by filtration and then washed with dry THF,

acetonitrile, water, and then methanol to obtain 5,5',5''-(benzenetricarbonyltris(azanediyl))triisophthalic acid (3.75 g, 89% yield, FW:699.53) after overnight drying under vacuum (< 0.1 mmHg). ^{1}H NMR (300 MHz, $CDCl_3$): δ 8.26 (s, 3H), 8.73 (s, 6H), 8.84 (s, 3H), 10.95 (s, 3H), 13.32 (s, 6H).

Synthesis of PCN-62.

$Cu(NO_3)_2 \cdot 6H_2O$ (30 mg) and H_6TPBTM (15 mg) were dissolved in 2 mL of *N*,*N*-dimthylformamide (DMF) in a 4 mL Pyrex vial, to which 0.2 mL of HNO_3 were added. The mixture was heated in an 85 ºC oven for 12 hours to yield 15 mg of blue crystals.

High-pressure adsorption measurements on PCN-62. A fully computer-controlled Sieverts apparatus, which has been reported,[204] was used to measure N_2 and CH_4 uptake.

5.3 Results and Discussion

Like other MOFs of the PCN-6X series, PCN-62, having **rht** topology, can be described as the packing of three types of polyhedra: cuboctahedra (cubOh), truncated tetrahedra (T-Td), and truncated octahedra (T-Oh) (Figure 82a). A sphere is displayed in the center of the pores to show the sizes of the pores (Figure 82b) and the results have been listed in Table 8 for comparison. As the linker becomes larger, the resulting MOF also has a larger unit cell length. The sizes of T-Tds and T-Ohs which are constructed from the linkers increase with the linkers getting larger. However, all cubOhs have the same size, since they are all constructed from isophthalate moieties and dicopper paddlewheels.

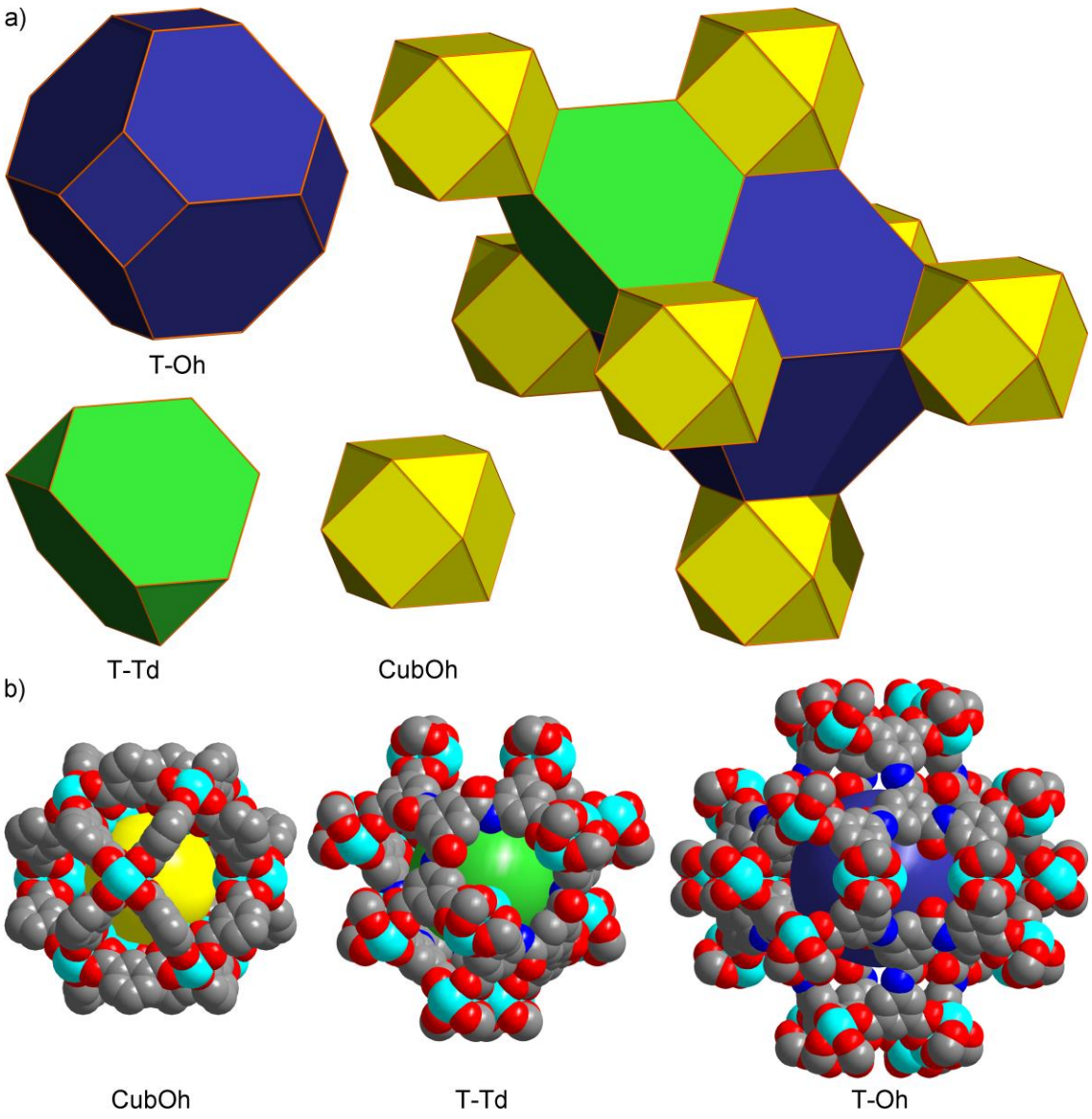

Figure 82. a) The three types of polyhedra in PCN-62 and their packing mode; b) the space-filling models of the polyhedra. The yellow, green, and indigo spheres represent the pores inside the polyhedra. Color scheme: C, grey; Cu, turquoise; O, red.

Table 8. Comparison of PCN-61, PCN-62 and PCN-66.

Material	Unit Cell Length (Å)	L Theoretical / Crystal Size (Å)[a]	CubOh Size (Å) [b]	T-Td Size (Å)	T-Oh Size (Å)
PCN-61	42.796	6.886 / 6.800	12.0	11.8	18.8
PCN-62	42.153	6.610 / 6.492	12.0	10.0	18.4
Difference	0.643	0.276 / 0.308	0	1.8	0.4

[a] The linker size is defined as the distance between the center of the linker and the center of a terminal benzene ring in the crystal structures.

[b] The size of the polyhedra is shown by a dummy sphere inside the pores that is big enough to contact the van der Waals surface of the framework. The diameter of the dummy sphere is the pore size.

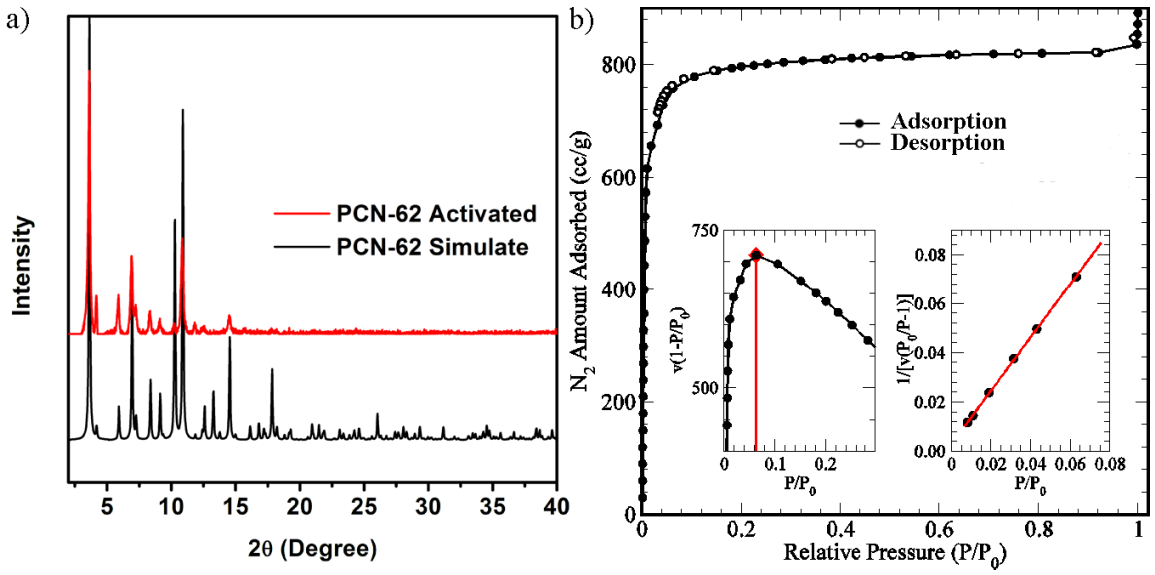

Figure 83. a) PXRD patters of PCN-62; b) N_2 adsorption isotherms under 77K and 1atm, the insets show the point range used for BET surface area calculations.

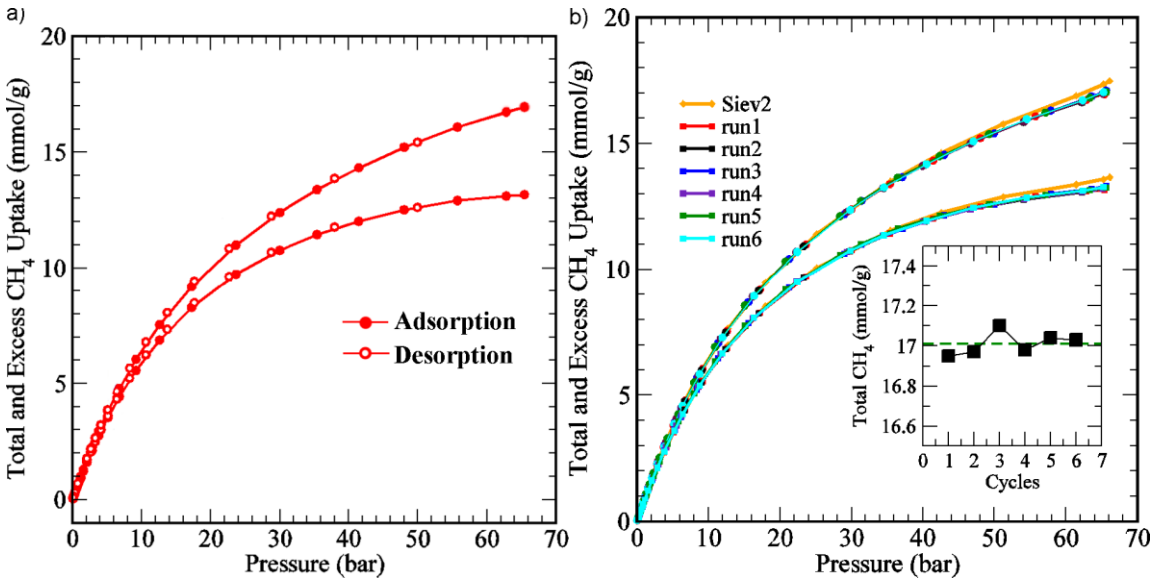

Figure 84. a) CH_4 sorption isotherms under 300 K was measured with the upper line presents the total uptake and the lower one presents the excess uptake. b) CH_4 sorption isotherms measured cycles, the inset shows the variation of the uptake with cycle 1~6 run on a Sievert 1 instrument. Siev2 is measurement on a Sievert 2 instrument.

The gas sorption measurements were performed at the Center for Neutron Research, National Institute of Standards and Technology (NIST) using a computer-controlled Sievert apparatus. The phase purity of freshly prepared sample was examined by powder X-ray diffraction (PXRD) (Figure 83a). Then the sample underwent regular solvent exchange and vacuum-heat activation. Nitrogen sorption measurements under 77K and 1 bar were performed to evaluate the porosity of PCN-62. The BET surface area and total pore volume are 3,204 $m^2\ g^{-1}$ and 1.273 $cm^3\ g^{-1}$, respectively. The experimental total pore volume is close to the theoretical value of 1.19 $cm^3\ g^{-1}$ calculated with PLATONT, indicating the sample has been fully activated. After confirming the status of the samples, high pressure methane uptake measurements were performed (Figure 84). The volumetric uptake reached 243 v_{STP}/v at 65 bar, which is much higher than the 222 v_{STP}/v of PCN-61. The working capacity is defined as the uptake difference between 65 bar and 5 bar. Thus the gravimetric working capacity of PCN-62 is 13.26 mmol g^{-1}, which corresponds to 0.213 g/g. The volumetric working capacity is 189 v_{STP}/v, which is also higher than the 177 v_{STP}/v of PCN-61. Thus, PCN-62 performs volumetrically almost the same as HKUST-1, which holds the record of 190 v_{STP}/v, but better gravimetrically (HKUST-1: 0.154 g/g).

TPBTM is just smaller than BETI with radius 0.308 Å (in crystal structures), and the unit cell length of PCN-62 is shorter than PCN-61 by 0.643 Å. The sizes of the three types of polyhedra cages are even smaller. However, the methane uptake capacities showed an extraordinary difference. The volumetric working capacity of PCN-62 is also higher than the total uptake of PCN-61 under 65 bar. This implies that tailoring pore size

properly, rather than simply increasing it, can also boost gas adsorption capacity. It implies that tiny changes in pore size and perhaps shape can cause a dramatic effect in methane storage capacity. However, the amide group, which is a strong polar group, may also have effect on the adsorption performance even the polarizability of methane molecule is low compared with CO_2 and quadruple moment of CH_4 is zero.

5.4 Conclusions

In summary, by applying a pore size tailoring strategy, a previously reported MOF, PCN-62 (Cu-TPBTM), has been synthesized and evaluated for methane storage capacity and working capacity. Its methane volumetric capacity increased over PCN-61. Also, its volumetric working capacity (189 v_{STP}/v) is nearly the same as HKUST-1 while the gravimetric working capacity (0.213 g/g) is higher than HKUST-1. In addition, the H_6TPBTM is easy to synthesize with low cost, which is beneficial to industrial application. The excellent adsorption performance of PCN-62 is likely based on the tiny difference in the elaborately tailored pore size. Considering the recently reported performance of HKUST-1, it can be concluded that in searching for the best materials for methane storage, it may worth to scan known materials as well as carefully tuning the structure of the outstanding ones.

6. SUMMARY

In this dissertation, three design strategies and one synthetic strategy have been proposed and demonstrated for synthesizing novel metal-organic frameworks targeting various applications.

In pursuing MOFs with large BET surface areas for hydrogen storage, large linkers have proved useful. Linker-extension by a hard-soft selective coordination strategy has been proposed and demonstrated. Taking MOF-14 as a prototype MOF constructed from BTB linkers, a porous MOF, PCN-91, was obtained with this design strategy. Three di-anions of 4-(3,5-dimethyl-1H-pyrazol-4-yl)-benzoic acid (H_2dmpba) coordinate to three Cu(I) ions, forming an extended trigonal planar metalo-linker, which is similar to but larger than BTB. The metalo-linker links three di-copper paddlewheel units giving rise to a Pt_3O_4 net, which is the same as MOF-14. The double interpenetrated framework is flexible, with the axial length able to change reversibly under varied temperatures. This phenomenon is attributed to the sliding of the two set frameworks.

A framework-templating strategy has been proposed to obtain MOF crystals which are very difficult to get in one-step solvothermal reactions. A microporous metal-organic framework, PCN-922 [Cu_4(ETTB)], constructed with an extended octatopic organic linker and a Cu_2 paddlewheel structural motif, has been synthesized by using a Zn_2 paddlewheel-based MOF as a template to prearrange the linkers for the Cu_2-based

MOF target. Compared to the labile Zn MOF template, which could not survive the activation process, Cu MOF PCN-922 shows permanent porosity and very high gas adsorption capacities.

We proposed and demonstrated that rigidifying the structure of fluorescent linkers by fixing them in metal-organic frameworks (MOFs) to control their conformation effectively tunes the fluorescence energy and enhances the quantum yield. A new tetraphenylethylene-based zirconium MOF exhibits a deep-blue fluorescent emission at 470 nm with 91 % quantum yield, representing ca. 3600 cm^{-1} blue shift and doubled radiative decay efficiency vs. the linker precursors. An anomalous increase in the fluorescence lifetime and relative intensity takes place upon heating the solid MOF from cryogenic to ambient temperatures. The origin of these unusual fluorescent properties is attributed to twisted linker conformation as well as inter- and intra-molecular interaction limitations resulting from linker rigidification.

Increasing linker size to obtain MOFs with larger pores and surface areas has proved an effective way to boost gravimetric gas uptake capacity under high pressure. However, the reverse idea of tailoring the linker size to obtain smaller pores for reducing dead space has been proposed and demonstrated in order to improve MOF methane volumetric uptake capacities. PCN-62, which has been reported as Cu-TPBTM, has smaller linkers and pores than PCN-61, showing 243 v_{STP}/v methane volumetric uptake under 65 bar and 189 v_{STP}/v working capacity from 65 to 5 bar.

REFERENCES

(1) Cook, T. R.; Zheng, Y.-R.; Stang, P. J. *Chem. Rev.* **2013,** *113*, 734.

(2) Gardner, G. B.; Venkataraman, D.; Moore, J. S.; Lee, S. *Nature* **1995,** *374*, 792.

(3) Yaghi, O. M.; Li, G.; Li, H. *Nature* **1995,** *378*, 703.

(4) Kondo, M.; Yoshitomi, T.; Matsuzaka, H.; Kitagawa, S.; Seki, K. *Angew. Chem. Int. Ed.* **1997,** *36*, 1725.

(5) Li, H.; Eddaoudi, M.; O'Keeffe, M.; Yaghi, O. M. *Nature* **1999,** *402*, 276.

(6) Férey, G.; Mellot-Draznieks, C.; Serre, C.; Millange, F. *Acc. Chem. Res.* **2005,** *38*, 217.

(7) Ferey, G.; Serre, C. *Chem. Soc. Rev.* **2009,** *38*, 1380.

(8) Horike, S.; Shimomura, S.; Kitagawa, S. *Nat. Chem.* **2009,** *1*, 695.

(9) Long, J. R.; Yaghi, O. M. *Chem. Soc. Rev.* **2009,** *38*, 1213.

(10) Yaghi, O. M.; O'Keeffe, M.; Ockwig, N. W.; Chae, H. K.; Eddaoudi, M.; Kim, J. *Nature* **2003,** *423*, 705.

(11) Chui, S. S.-Y.; Lo, S. M.-F.; Charmant, J. P. H.; Orpen, A. G.; Williams, I. D. *Science* **1999,** *283*, 1148.

(12) Furukawa, H.; Cordova, K. E.; O'Keeffe, M.; Yaghi, O. M. *Science* **2013,** *341*, 974.

(13) Zhou, H.-C.; Long, J. R.; Yaghi, O. M. *Chem. Rev.* **2012,** *112*, 673.

(14) Li, J.-R.; Sculley, J.; Zhou, H.-C. *Chem. Rev.* **2012,** *112*, 869.

(15) Foo, K. Y.; Hameed, B. H. *Adv. Colloid Interfac* **2011,** *162*, 22.

(16) Cui, Y.; Yue, Y.; Qian, G.; Chen, B. *Chem. Rev.* **2012,** *112*, 1126.

(17) Kurmoo, M. *Chem. Soc. Rev.* **2009,** *38*, 1353.

(18) Zhang, W.; Xiong, R.-G. *Chem. Rev.* **2012,** *112*, 1163.

(19) Suh, M. P.; Park, H. J.; Prasad, T. K.; Lim, D.-W. *Chem. Rev.* **2012,** *112*, 782.

(20) Makal, T. A.; Li, J.-R.; Lu, W.; Zhou, H.-C. *Chem. Soc. Rev.* **2012,** *41*, 7761.

(21) Getman, R. B.; Bae, Y.-S.; Wilmer, C. E.; Snurr, R. Q. *Chem. Rev.* **2012,** *112*, 703.

(22) Sumida, K.; Rogow, D. L.; Mason, J. A.; McDonald, T. M.; Bloch, E. D.; Herm, Z. R.; Bae, T.-H.; Long, J. R. *Chem. Rev.* **2012,** *112*, 724.

(23) Corma, A.; García, H.; Llabrés i Xamena, F. X. *Chem. Rev.* **2010,** *110*, 4606.

(24) Yoon, M.; Srirambalaji, R.; Kim, K. *Chem. Rev.* **2012,** *112*, 1196.

(25) Kreno, L. E.; Leong, K.; Farha, O. K.; Allendorf, M.; Van Duyne, R. P.; Hupp, J. T. *Chem. Rev.* **2012,** *112*, 1105.

(26) Horcajada, P.; Gref, R.; Baati, T.; Allan, P. K.; Maurin, G.; Couvreur, P.; Férey, G.; Morris, R. E.; Serre, C. *Chem. Rev.* **2012,** *112*, 1232.

(27) Yoon, M.; Suh, K.; Natarajan, S.; Kim, K. *Angew. Chem. Int. Ed.* **2013,** *52*, 2688.

(28) Della Rocca, J.; Liu, D.; Lin, W. *Acc. Chem. Res.* **2011,** *44*, 957.

(29) Wang, C.; Zhang, T.; Lin, W. *Chem. Rev.* **2012,** *112*, 1084.

(30) Kitagawa, S.; Kitaura, R.; Noro, S.-i. *Angew. Chem. Int. Ed.* **2004,** *43*, 2334.

(31) Tranchemontagne, D. J.; Mendoza-Cortes, J. L.; O'Keeffe, M.; Yaghi, O. M. *Chem. Soc. Rev.* **2009,** *38*, 1257.

(32) Eddaoudi, M.; Moler, D. B.; Li, H.; Chen, B.; Reineke, T. M.; O'Keeffe, M.; Yaghi, O. M. *Acc. Chem. Res.* **2001,** *34*, 319.

(33) Liu, T.-F.; Lü, J.; Guo, Z.; Proserpio, D. M.; Cao, R. *Cryst. Growth Des.* **2010,** *10*, 1489.

(34) Britt, D.; Tranchemontagne, D.; Yaghi, O. M. *Proc. Natl. Acad. Sci. U. S. A.* **2008,** *105*, 11623.

(35) Cavka, J. H.; Jakobsen, S.; Olsbye, U.; Guillou, N.; Lamberti, C.; Bordiga, S.; Lillerud, K. P. *J. Am. Chem. Soc.* **2008,** *130*, 13850.

(36) Feng, D.; Jiang, H.-L.; Chen, Y.-P.; Gu, Z.-Y.; Wei, Z.; Zhou, H.-C. *Inorg. Chem.* **2013,** *52*, 12661.

(37) Guillerm, V.; Ragon, F.; Dan-Hardi, M.; Devic, T.; Vishnuvarthan, M.; Campo, B.; Vimont, A.; Clet, G.; Yang, Q.; Maurin, G.; Férey, G.; Vittadini, A.; Gross, S.; Serre, C. *Angew. Chem. Int. Ed.* **2012,** *51*, 9267.

(38) Morris, W.; Volosskiy, B.; Demir, S.; Gándara, F.; McGrier, P. L.; Furukawa, H.; Cascio, D.; Stoddart, J. F.; Yaghi, O. M. *Inorg. Chem.* **2012,** *51*, 6443.

(39) Feng, D.; Gu, Z.-Y.; Li, J.-R.; Jiang, H.-L.; Wei, Z.; Zhou, H.-C. *Angew. Chem. Int. Ed.* **2012,** *51*, 10307.

(40) Jiang, H.-L.; Feng, D.; Wang, K.; Gu, Z.-Y.; Wei, Z.; Chen, Y.-P.; Zhou, H.-C. *J. Am. Chem. Soc.* **2013,** *135*, 13934.

(41) Feng, D.; Chung, W.-C.; Wei, Z.; Gu, Z.-Y.; Jiang, H.-L.; Darensbourg, D. J.; Zhou, H.-C. *J. Am. Chem. Soc.* **2013,** *135*, 17105.

(42) Brozek, C. K.; Dinca, M. *Chem. Sci.* **2012,** *3*, 2110.

(43) Yu, J.; Cui, Y.; Wu, C.; Yang, Y.; Wang, Z.; O'Keeffe, M.; Chen, B.; Qian, G. *Angew. Chem. Int. Ed.* **2012,** *51*, 10542.

(44) Wei, Z.; Lu, W.; Jiang, H.-L.; Zhou, H.-C. *Inorg. Chem.* **2013,** *52*, 1164.

(45) Férey, G.; Mellot-Draznieks, C.; Serre, C.; Millange, F.; Dutour, J.; Surblé, S.; Margiolaki, I. *Science* **2005,** *309*, 2040.

(46) Ma, S.; Yuan, D.; Chang, J.-S.; Zhou, H.-C. *Inorg. Chem.* **2009,** *48*, 5398.

(47) Dincă, M.; Han, W. S.; Liu, Y.; Dailly, A.; Brown, C. M.; Long, J. R. *Angew. Chem. Int. Ed.* **2007,** *46*, 1419.

(48) Serre, C.; Millange, F.; Thouvenot, C.; Noguès, M.; Marsolier, G.; Louër, D.; Férey, G. *J. Am. Chem. Soc.* **2002,** *124*, 13519.

(49) Liu, Y.; Wang, Q.; Chen, L.; Zhao, H.; Zhao, J. *Synthetic. Met.* **2012,** *162*, 1648.

(50) Deng, H.; Grunder, S.; Cordova, K. E.; Valente, C.; Furukawa, H.; Hmadeh, M.; Gándara, F.; Whalley, A. C.; Liu, Z.; Asahina, S.; Kazumori, H.; O'Keeffe, M.; Terasaki, O.; Stoddart, J. F.; Yaghi, O. M. *Science* **2012,** *336*, 1018.

(51) Wang, X.-S.; Ma, S.; Forster, P. M.; Yuan, D.; Eckert, J.; López, J. J.; Murphy, B. J.; Parise, J. B.; Zhou, H.-C. *Angew. Chem. Int. Ed.* **2008,** *47*, 7263.

(52) Ma, S.; Eckert, J.; Forster, P. M.; Yoon, J. W.; Hwang, Y. K.; Chang, J.-S.; Collier, C. D.; Parise, J. B.; Zhou, H.-C. *J. Am. Chem. Soc.* **2008,** *130*, 15896.

(53) Yuan, D.; Zhao, D.; Sun, D.; Zhou, H.-C. *Angew. Chem. Int. Ed.* **2010,** *49*, 5357.

(54) Zhuang, W.; Yuan, D.; Liu, D.; Zhong, C.; Li, J.-R.; Zhou, H.-C. *Chem. Mater.* **2011,** *24*, 18.

(55) Collins, C. S.; Sun, D.; Liu, W.; Zuo, J.-L.; Zhou, H.-C. *J. Mol. Struct.* **2008,** *890*, 163.

(56) Zhao, D.; Timmons, D. J.; Yuan, D.; Zhou, H.-C. *Acc. Chem. Res.* **2011,** *44*, 123.

(57) Wong-Foy, A. G.; Lebel, O.; Matzger, A. J. *J. Am. Chem. Soc.* **2007,** *129*, 15740.

(58) Schnobrich, J. K.; Lebel, O.; Cychosz, K. A.; Dailly, A.; Wong-Foy, A. G.; Matzger, A. J. *J. Am. Chem. Soc.* **2010,** *132*, 13941.

(59) Tan, C.; Yang, S.; Champness, N. R.; Lin, X.; Blake, A. J.; Lewis, W.; Schroder, M. *Chem. Commun.* **2011,** *47*, 4487.

(60) Gagnon, K. J.; Perry, H. P.; Clearfield, A. *Chem. Rev.* **2012,** *112*, 1034.

(61) Shimizu, G. K. H.; Vaidhyanathan, R.; Taylor, J. M. *Chem. Soc. Rev.* **2009,** *38*, 1430.

(62) Zhang, J.-P.; Zhang, Y.-B.; Lin, J.-B.; Chen, X.-M. *Chem. Rev.* **2012,** *112*, 1001.

(63) Phan, A.; Doonan, C. J.; Uribe-Romo, F. J.; Knobler, C. B.; O'Keeffe, M.; Yaghi, O. M. *Acc. Chem. Res.* **2010,** *43*, 58.

(64) Nouar, F.; Eubank, J. F.; Bousquet, T.; Wojtas, L.; Zaworotko, M. J.; Eddaoudi, M. *J. Am. Chem. Soc.* **2008,** *130*, 1833.

(65) Zhao, D.; Yuan, D.; Yakovenko, A.; Zhou, H.-C. *Chem. Commun.* **2010,** *46*, 4196.

(66) O'Keeffe, M.; Yaghi, O. M. *Chem. Rev.* **2012,** *112*, 675.

(67) Eddaoudi, M.; Kim, J.; Rosi, N.; Vodak, D.; Wachter, J.; O'Keeffe, M.; Yaghi, O. M. *Science* **2002,** *295*, 469.

(68) Cohen, S. M. *Chem. Rev.* **2012,** *112*, 970.

(69) Jiang, H.-L.; Feng, D.; Liu, T.-F.; Li, J.-R.; Zhou, H.-C. *J. Am. Chem. Soc.* **2012,** *134*, 14690.

(70) McDonald, T. M.; D'Alessandro, D. M.; Krishna, R.; Long, J. R. *Chem. Sci.* **2011,** *2*, 2022.

(71) Kim, M.; Cahill, J. F.; Fei, H.; Prather, K. A.; Cohen, S. M. *J. Am. Chem. Soc.* **2012,** *134*, 18082.

(72) Kaye, S. S.; Dailly, A.; Yaghi, O. M.; Long, J. R. *J. Am. Chem. Soc.* **2007,** *129*, 14176.

(73) Makal, T. A.; Yakovenko, A. A.; Zhou, H.-C. *J. Phys. Chem. Lett.* **2011,** *2*, 1682.

(74) Jiang, H.-L.; Tatsu, Y.; Lu, Z.-H.; Xu, Q. *J. Am. Chem. Soc.* **2010,** *132*, 5586.

(75) Furukawa, H.; Ko, N.; Go, Y. B.; Aratani, N.; Choi, S. B.; Choi, E.; Yazaydin, A. Ö.; Snurr, R. Q.; O'Keeffe, M.; Kim, J.; Yaghi, O. M. *Science* **2010,** *329*, 424.

(76) Park, J.; Wang, Z. U.; Sun, L.-B.; Chen, Y.-P.; Zhou, H.-C. *J. Am. Chem. Soc.* **2012,** *134*, 20110.

(77) Bae, Y.-S.; Mulfort, K. L.; Frost, H.; Ryan, P.; Punnathanam, S.; Broadbelt, L. J.; Hupp, J. T.; Snurr, R. Q. *Langmuir* **2008,** *24*, 8592.

(78) Stock, N.; Biswas, S. *Chem. Rev.* **2012,** *112*, 933.

(79) Mueller, U.; Schubert, M.; Teich, F.; Puetter, H.; Schierle-Arndt, K.; Pastre, J. *J. Mater. Chem.* **2006,** *16*, 626.

(80) Kim, J.; Yang, S.-T.; Choi, S. B.; Sim, J.; Kim, J.; Ahn, W.-S. *J. Mater. Chem.* **2011,** *21*, 3070.

(81) Yuan, W.; Friščić, T.; Apperley, D.; James, S. L. *Angew. Chem. Int. Ed.* **2010,** *49*, 3916.

(82) Ahnfeldt, T.; Moellmer, J.; Guillerm, V.; Staudt, R.; Serre, C.; Stock, N. *Chem. Eur. J.* **2011,** *17*, 6462.

(83) Schlesinger, M.; Schulze, S.; Hietschold, M.; Mehring, M. *Microporous Mesoporous Mater.* **2010,** *132*, 121.

(84) Surble, S.; Millange, F.; Serre, C.; Ferey, G.; Walton, R. I. *Chem. Commun.* **2006**, 1518.

(85) Brunauer, S.; Emmett, P. H.; Teller, E. *J. Am. Chem. Soc.* **1938,** *60*, 309.

(86) Park, J.; Yuan, D.; Pham, K. T.; Li, J.-R.; Yakovenko, A.; Zhou, H.-C. *J. Am. Chem. Soc.* **2011,** *134*, 99.

(87) Wriedt, M.; Sculley, J. P.; Yakovenko, A. A.; Ma, Y.; Halder, G. J.; Balbuena, P. B.; Zhou, H.-C. *Angew. Chem. Int. Ed.* **2012,** *51*, 9804.

(88) Dincă, M.; Dailly, A.; Liu, Y.; Brown, C. M.; Neumann, D. A.; Long, J. R. *J. Am. Chem. Soc.* **2006,** *128*, 16876.

(89) Wu, H.; Simmons, J. M.; Liu, Y.; Brown, C. M.; Wang, X.-S.; Ma, S.; Peterson, V. K.; Southon, P. D.; Kepert, C. J.; Zhou, H.-C.; Yildirim, T.; Zhou, W. *Chem. Eur. J.* **2010,** *16*, 5205.

(90) Wu, H.; Zhou, W.; Yildirim, T. *J. Am. Chem. Soc.* **2009,** *131*, 4995.

(91) Valenzano, L.; Civalleri, B.; Chavan, S.; Palomino, G. T.; Areán, C. O.; Bordiga, S. *J. Phys. Chem. C* **2010,** *114*, 11185.

(92) Siberio-Pérez, D. Y.; Wong-Foy, A. G.; Yaghi, O. M.; Matzger, A. J. *Chem. Mater.* **2007,** *19*, 3681.

(93) Wilmer, C. E.; Leaf, M.; Lee, C. Y.; Farha, O. K.; Hauser, B. G.; Hupp, J. T.; Snurr, R. Q. *Nat. Chem.* **2012,** *4*, 83.

(94) Rowsell, J. L. C.; Yaghi, O. M. *J. Am. Chem. Soc.* **2006,** *128*, 1304.

(95) Nelson, A. P.; Farha, O. K.; Mulfort, K. L.; Hupp, J. T. *J. Am. Chem. Soc.* **2009,** *131*, 458.

(96) Ma, L.; Jin, A.; Xie, Z.; Lin, W. *Angew. Chem. Int. Ed.* **2009,** *48*, 9905.

(97) Zhao, D.; Yuan, D.; Zhou, H.-C. *Energy Environ. Sci.* **2008,** *1*, 222.

(98) Bastos-Neto, M.; Patzschke, C.; Lange, M.; Mollmer, J.; Moeller, A.; Fichtner, S.; Schrage, C.; Lassig, D.; Lincke, J.; Krautscheid, H.; Staudt, R.; Glaser, R. *Energy Environ. Sci.* **2012,** *5*, 8294.

(99) Farha, O. K.; Eryazici, I.; Jeong, N. C.; Hauser, B. G.; Wilmer, C. E.; Sarjeant, A. A.; Snurr, R. Q.; Nguyen, S. T.; Yazaydın, A. Ö.; Hupp, J. T. *J. Am. Chem. Soc.* **2012,** *134*, 15016.

(100) Farha, O. K.; Özgür Yazaydın, A.; Eryazici, I.; Malliakas, C. D.; Hauser, B. G.; Kanatzidis, M. G.; Nguyen, S. T.; Snurr, R. Q.; Hupp, J. T. *Nat. Chem.* **2010,** *2*, 944.

(101) Yang, S. H.; Lin, X.; Blake, A. J.; Walker, G. S.; Hubberstey, P.; Champness, N. R.; Schroder, M. *Nature Chemistry* **2009,** *1*, 487.

(102) Mulfort, K. L.; Farha, O. K.; Stern, C. L.; Sarjeant, A. A.; Hupp, J. T. *J. Am. Chem. Soc.* **2009,** *131*, 3866.

(103) Li, Y.; Yang, R. T. *J. Am. Chem. Soc.* **2006,** *128*, 726.

(104) Hübner, O.; Glöss, A.; Fichtner, M.; Klopper, W. *J. Phys. Chem. A* **2004,** *108*, 3019.

(105) Ma, S.; Sun, D.; Simmons, J. M.; Collier, C. D.; Yuan, D.; Zhou, H.-C. *J. Am. Chem. Soc.* **2008,** *130*, 1012.

(106) Lu, W.; Sculley, J. P.; Yuan, D.; Krishna, R.; Wei, Z.; Zhou, H.-C. *Angew. Chem. Int. Ed.* **2012,** *51*, 7480.

(107) Nugent, P.; Belmabkhout, Y.; Burd, S. D.; Cairns, A. J.; Luebke, R.; Forrest, K.; Pham, T.; Ma, S.; Space, B.; Wojtas, L.; Eddaoudi, M.; Zaworotko, M. J. *Nature* **2013,** *495*, 80.

(108) Millward, A. R.; Yaghi, O. M. *J. Am. Chem. Soc.* **2005,** *127*, 17998.

(109) Banerjee, R.; Furukawa, H.; Britt, D.; Knobler, C.; O'Keeffe, M.; Yaghi, O. M. *J. Am. Chem. Soc.* **2009,** *131*, 3875.

(110) Yang, Q. Y.; Wiersum, A. D.; Llewellyn, P. L.; Guillerm, V.; Serred, C.; Maurin, G. *Chem. Commun.* **2011,** *47*, 9603.

(111) Li, J.-R.; Yu, J.; Lu, W.; Sun, L.-B.; Sculley, J.; Balbuena, P. B.; Zhou, H.-C. *Nat. Commun.* **2013,** *4*, 1538.

(112) Caskey, S. R.; Wong-Foy, A. G.; Matzger, A. J. *J. Am. Chem. Soc.* **2008,** *130*, 10870.

(113) Horcajada, P.; Chalati, T.; Serre, C.; Gillet, B.; Sebrie, C.; Baati, T.; Eubank, J. F.; Heurtaux, D.; Clayette, P.; Kreuz, C.; Chang, J.-S.; Hwang, Y. K.; Marsaud, V.; Bories, P.-N.; Cynober, L.; Gil, S.; Ferey, G.; Couvreur, P.; Gref, R. *Nat. Mater.* **2010,** *9*, 172.

(114) Kuppler, R. J.; Timmons, D. J.; Fang, Q.-R.; Li, J.-R.; Makal, T. A.; Young, M. D.; Yuan, D.; Zhao, D.; Zhuang, W.; Zhou, H.-C. *Coord. Chem. Rev.* **2009,** *253*, 3042.

(115) Fateeva, A.; Chater, P. A.; Ireland, C. P.; Tahir, A. A.; Khimyak, Y. Z.; Wiper, P. V.; Darwent, J. R.; Rosseinsky, M. J. *Angew. Chem. Int. Ed.* **2012,** *51*, 7440.

(116) Ma, S.; Zhou, H.-C. *Chem. Commun.* **2010,** *46*, 44.

(117) Seo, J. S.; Whang, D.; Lee, H.; Jun, S. I.; Oh, J.; Jeon, Y. J.; Kim, K. *Nature* **2000,** *404*, 982.

(118) Farrusseng, D.; Aguado, S.; Pinel, C. *Angew. Chem. Int. Ed.* **2009,** *48*, 7502.

(119) Ma, L.; Abney, C.; Lin, W. *Chem. Soc. Rev.* **2009,** *38*, 1248.

(120) Corma, A.; García, H.; Llabrés i Xamena, F. X. *Chem. Rev.* **2010,** *110*, 4606.

(121) Jiang, H.-L.; Xu, Q. *Chem. Commun.* **2011,** *47*, 3351.

(122) Chen, B.; Xiang, S.; Qian, G. *Acc. Chem. Res.* **2010,** *43*, 1115.

(123) Takashima, Y.; Martínez, V. M.; Furukawa, S.; Kondo, M.; Shimomura, S.; Uehara, H.; Nakahama, M.; Sugimoto, K.; Kitagawa, S. *Nat. Commun.* **2011,** *2*, 168.

(124) An, J.; Geib, S. J.; Rosi, N. L. *J. Am. Chem. Soc.* **2009,** *131*, 8376.

(125) Zhao, D.; Yuan, D.; Sun, D.; Zhou, H.-C. *J. Am. Chem. Soc.* **2009,** *131*, 9186.

(126) Stork, J. R.; Thoi, V. S.; Cohen, S. M. *Inorg. Chem.* **2007,** *46*, 11213.

(127) Halper, S. R.; Do, L.; Stork, J. R.; Cohen, S. M. *J. Am. Chem. Soc.* **2006,** *128*, 15255.

(128) Scott, T. A.; Abbaoui, B.; Zhou, H.-C. *Inorg. Chem.* **2004,** *43*, 2459.

(129) He, J.; Yin, Y. G.; Wu, T.; Li, D.; Huang, X. C. *Chem. Commun.* **2006,** 10.1039/b601009a, 2845.

(130) Zhang, J. P.; Kitagawa, S. *J. Am. Chem. Soc.* **2008,** *130*, 907.

(131) Zhang, J. X.; He, J.; Yin, Y. G.; Hu, M. H.; Li, D.; Huang, X. C. *Inorg. Chem.* **2008,** *47*, 3471.

(132) Lo, S. M. F.; Chui, S. S. Y.; Shek, L. Y.; Lin, Z. Y.; Zhang, X. X.; Wen, G. H.; Williams, I. D. *J. Am. Chem. Soc.* **2000,** *122*, 6293.

(133) Hammond, G. S.; Nonhebel, D. C.; Wu, C.-H. S. *Inorg. Chem.* **1963,** *2*, 73.

(134) Broxton, T. J.; Bunnett, J. F.; Paik, C. H. *The Journal of Organic Chemistry* **1977,** *42*, 643.

(135) Citterio, A.; Ferrario, F. *J. Chem. Res-s.* **1983**, 308.

(136) Lorris, M. E.; Abramovitch, R. A.; Marquet, J.; Moreno-Mañas, M. *Tetrahedron* **1992,** *48*, 6909.

(137) Spek, A. *J. Appl. Crystallogr.* **2003,** *36*, 7.

(138) Wagner, C. D.; Riggs, W. M.; Davis, L. E.; Moulder, J. F., *Handbook of X-ray Photoelectron Spectroscopy*. Muilenberg, GE: Perkin-Elmer Cor., Physical Electronics Division, Eden Prairle, MN, 1979.

(139) Chen, B.; Eddaoudi, M.; Hyde, S. T.; O'Keeffe, M.; Yaghi, O. M. *Science* **2001,** *291*, 1021.

(140) Sun, D.; Ke, Y.; Mattox, T. M.; Parkin, S.; Zhou, H.-C. *Inorg. Chem.* **2006,** *45*, 7566.

(141) Sun, D. F.; Ma, S. Q.; Ke, Y. X.; Collins, D. J.; Zhou, H. C. *J. Am. Chem. Soc.* **2006,** *128*, 3896.

(142) Dias, H. V. R.; Diyabalanage, H. V. K.; Eldabaja, M. G.; Elbjeirami, O.; Rawashdeh-Omary, M. A.; Omary, M. A. *J. Am. Chem. Soc.* **2005,** *127*, 7489.

(143) He, J.; Yin, Y.-G.; Wu, T.; Li, D.; Huang, X.-C. *Chem. Commun.* **2006**, 2845.

(144) Zhang, J.-P.; Kitagawa, S. *J. Am. Chem. Soc.* **2008,** *130*, 907.

(145) Gao, G.-F.; Li, M.; Zhan, S.-Z.; Lv, Z.; Chen, G.-h.; Li, D. *Chem. Eur. J.* **2011,** *17*, 4113.

(146) Ramsahye, N. A.; Trung, T. K.; Bourrelly, S.; Yang, Q. Y.; Devic, T.; Maurin, G.; Horcajada, P.; Llewellyn, P. L.; Yot, P.; Serre, C.; Filinchuk, Y.; Fajula, F.; Ferey, G.; Trens, P. *J. Phys. Chem. C* **2011,** *115*, 18683.

(147) Lu, W.; Yuan, D.; Makal, T. A.; Li, J.-R.; Zhou, H.-C. *Angew. Chem. Int. Ed.* **2012,** *51*, 1580.

(148) Blatov, V. A. *IUCr CompComm Newsletter* **2006,** *7*, 4.

(149) Cychosz, K. A.; Matzger, A. J. *Langmuir* **2010,** *26*, 17198.

(150) Collins, D. J.; Zhou, H.-C. *J. Mater. Chem.* **2007,** *17*, 3154.

(151) Dincă, M.; Long, J. R. *Angew. Chem. Int. Ed.* **2008,** *47*, 6766.

(152) Rowsell, J. L. C.; Yaghi, O. M. *Angew. Chem. Int. Ed.* **2005,** *44*, 4670.

(153) Vitillo, J. G.; Regli, L.; Chavan, S.; Ricchiardi, G.; Spoto, G.; Dietzel, P. D. C.; Bordiga, S.; Zecchina, A. *J. Am. Chem. Soc.* **2008,** *130*, 8386.

(154) Gedrich, K.; Senkovska, I.; Klein, N.; Stoeck, U.; Henschel, A.; Lohe, M. R.; Baburin, I. A.; Mueller, U.; Kaskel, S. *Angew. Chem. Int. Ed.* **2010,** *49*, 8489.

(155) Haque, E.; Jeong, J. H.; Jhung, S. H. *CrystEngComm* **2010,** *12*, 2749.

(156) Miessler, G. L. T., Donald A., *Inorganic Chemistry*. Pearson Educaiion, Inc.: Upper Saddle River, 2004.

(157) Feldblyum, J. I.; Liu, M.; Gidley, D. W.; Matzger, A. J. *J. Am. Chem. Soc.* **2011,** *133*, 18257.

(158) Dincă, M.; Long, J. R. *J. Am. Chem. Soc.* **2007,** *129*, 11172.

(159) Mi, L.; Hou, H.; Song, Z.; Han, H.; Xu, H.; Fan, Y.; Ng, S.-W. *Cryst. Growth Des.* **2007,** *7*, 2553.

(160) Mi, L.; Hou, H.; Song, Z.; Han, H.; Fan, Y. *Chem. Eur. J.* **2008,** *14*, 1814.

(161) Das, S.; Kim, H.; Kim, K. *J. Am. Chem. Soc.* **2009,** *131*, 3814.

(162) Tian, J.; Saraf, L. V.; Schwenzer, B.; Taylor, S. M.; Brechin, E. K.; Liu, J.; Dalgarno, S. J.; Thallapally, P. K. *J. Am. Chem. Soc.* **2012,** *134*, 9581.

(163) Yao, Q.; Sun, J.; Li, K.; Su, J.; Peskov, M. V.; Zou, X. *Dalton Trans.* **2012,** *41*, 3953.

(164) Wang, X.; Li, P.-Z.; Liu, L.; Zhang, Q.; Borah, P.; Wong, J. D.; Chan, X. X.; Rakesh, G.; Li, Y.; Zhao, Y. *Chem. Commun.* **2012,** *48*, 10286.

(165) Li, J.-R.; Zhou, H.-C. *Nat. Chem.* **2010,** *2*, 893.

(166) Vyas, V. S.; Banerjee, M.; Rathore, R. *Tetrahedron Lett.* **2009,** *50*, 6159.

(167) Natera, J.; Otero, L.; Sereno, L.; Fungo, F.; Wang, N.-S.; Tsai, Y.-M.; Hwu, T.-Y.; Wong, K.-T. *Macromolecules* **2007,** *40*, 4456.

(168) Sheldrick, G. *Acta Crystallogr. A* **2008,** *64*, 112.

(169) Langmuir, I. *J. Am. Chem. Soc.* **1916,** *38*, 2221.

(170) Yang, J. S.; Swager, T. M. *J. Am. Chem. Soc.* **1998,** *120*, 11864.

(171) Moerner, W. E.; Orrit, M. *Science* **1999,** *283*, 1670.

(172) Gunnlaugsson, T.; Glynn, M.; Tocci, G. M.; Kruger, P. E.; Pfeffer, F. M. *Coord. Chem. Rev.* **2006,** *250*, 3094.

(173) Baldo, M. A.; O'Brien, D. F.; You, Y.; Shoustikov, A.; Sibley, S.; Thompson, M. E.; Forrest, S. R. *Nature* **1998,** *395*, 151.

(174) D'Andrade, B. W.; Forrest, S. R. *Adv. Mater.* **2004,** *16*, 1585.

(175) Wu, H.; Gong, Q.; Olson, D. H.; Li, J. *Chem. Rev.* **2012,** *112*, 836.

(176) Allendorf, M. D.; Bauer, C. A.; Bhakta, R. K.; Houk, R. J. T. *Chem. Soc. Rev.* **2009,** *38*, 1330.

(177) Bétard, A. l.; Fischer, R. A. *Chem. Rev.* **2011,** *112*, 1055.

(178) Gu, Z.-Y.; Yang, C.-X.; Chang, N.; Yan, X.-P. *Acc. Chem. Res.* **2012,** *45*, 734.

(179) Zou, J.-P.; Peng, Q.; Wen, Z.; Zeng, G.-S.; Xing, Q.-J.; Guo, G.-C. *Cryst. Growth Des.* **2010,** *10*, 2613.

(180) Feng, R.; Jiang, F.-L.; Chen, L.; Yan, C.-F.; Wu, M.-Y.; Hong, M.-C. *Chem. Commun.* **2009,** *0*, 5296.

(181) Liu, Y.; Pan, M.; Yang, Q.-Y.; Fu, L.; Li, K.; Wei, S.-C.; Su, C.-Y. *Chem. Mater.* **2012,** *24*, 1954.

(182) Ablet, A.; Li, S.-M.; Cao, W.; Zheng, X.-J.; Wong, W.-T.; Jin, L.-P. *Chemistry – An Asian Journal* **2013,** *8*, 95.

(183) White, K. A.; Chengelis, D. A.; Gogick, K. A.; Stehman, J.; Rosi, N. L.; Petoud, S. p. *J. Am. Chem. Soc.* **2009,** *131*, 18069.

(184) Lee, C. Y.; Farha, O. K.; Hong, B. J.; Sarjeant, A. A.; Nguyen, S. T.; Hupp, J. T. *J. Am. Chem. Soc.* **2011,** *133*, 15858.

(185) Son, H.-J.; Jin, S.; Patwardhan, S.; Wezenberg, S. J.; Jeong, N. C.; So, M.; Wilmer, C. E.; Sarjeant, A. A.; Schatz, G. C.; Snurr, R. Q.; Farha, O. K.; Wiederrecht, G. P.; Hupp, J. T. *J. Am. Chem. Soc.* **2012,** *135*, 862.

(186) Liu, T.-F.; Zhang, W.; Sun, W.-H.; Cao, R. *Inorg. Chem.* **2011,** *50*, 5242.

(187) Vyas, V. S.; Rathore, R. *Chem. Commun.* **2010,** *46*, 1065.

(188) Shustova, N. B.; McCarthy, B. D.; Dincă, M. *J. Am. Chem. Soc.* **2011,** *133*, 20126.

(189) Shustova, N. B.; Cozzolino, A. F.; Reineke, S.; Baldo, M.; Dincă, M. *J. Am. Chem. Soc.* **2013,** *135*, 13326.

(190) Shustova, N. B.; Ong, T.-C.; Cozzolino, A. F.; Michaelis, V. K.; Griffin, R. G.; Dincă, M. *J. Am. Chem. Soc.* **2012,** *134*, 15061.

(191) Shustova, N. B.; Cozzolino, A. F.; Dincă, M. *J. Am. Chem. Soc.* **2012,** *134*, 19596.

(192) Zhang, W.; Huang, H.; Liu, D.; Yang, Q.; Xiao, Y.; Ma, Q.; Zhong, C. *Microporous Mesoporous Mater.* **2013,** *171*, 118.

(193) Kandiah, M.; Nilsen, M. H.; Usseglio, S.; Jakobsen, S.; Olsbye, U.; Tilset, M.; Larabi, C.; Quadrelli, E. A.; Bonino, F.; Lillerud, K. P. *Chem. Mater.* **2010,** *22*, 6632.

(194) Schaate, A.; Roy, P.; Preuße, T.; Lohmeier, S. J.; Godt, A.; Behrens, P. *Chem. Eur. J.* **2011,** *17*, 9320.

(195) Vermoortele, F.; Ameloot, R.; Vimont, A.; Serre, C.; De Vos, D. *Chem. Commun.* **2011,** *47*, 1521.

(196) Kim, M.; Cahill, J. F.; Su, Y. X.; Prather, K. A.; Cohen, S. M. *Chem. Sci.* **2012,** *3*, 126.

(197) Accelrys, *Materials Studio Release Motes, Release 5.5.1*. Accelrys Software, Inc. : San Diego, 2010.

(198) Walton, K. S.; Snurr, R. Q. *J. Am. Chem. Soc.* **2007,** *129*, 8552.

(199) Melhuish, W. H. *The Journal of Physical Chemistry* **1961,** *65*, 229.

(200) Lacowicz, J. R., *Principles of Fluorescence Spectroscopy*. 2nd ed.; Kluwer Academic/Plenum: New York, 1999.

(201) Xia, G.; Sun, Q.; Cao, X.; Wang, J.; Yu, Y.; Wang, L. *Energy*， http://dx.doi.org/10.1016/j.energy.2013.12.029.

(202) Mortazavi, A.; Alabdulkarem, A.; Hwang, Y.; Radermacher, R. *Appl. Energ.* **2014,** *117*, 76.

(203) Pham, T.; Forrest, K. A.; Nugent, P.; Belmabkhout, Y.; Luebke, R.; Eddaoudi, M.; Zaworotko, M. J.; Space, B. *J. Phys. Chem. C* **2013,** *117*, 9340.

(204) Zhou, W.; Wu, H.; Hartman, M. R.; Yildirim, T. *J. Phys. Chem. C* **2007,** *111*, 16131.